DESIGN OF AN AXIAL-FLUX GENERATOR FOR A SMALL-SCALE WIND ELECTROLYSIS PLANT

By:

John Gitonga Wanjiku

A Thesis Submitted to the Department of Electrical Engineering, University of Cape Town, in complete fulfilment of the requirements for the degree of Master of Science in Electrical Engineering

November, 2010

DECLARATION

This is to certify that the work is entirely my own and not of any other person, unless explicitly acknowledged (including citation of published and unpublished sources). The work has not been previously submitted in any form to the University of Cape Town or any other institution for assessment for any other purpose.

Signature……

J.G. Wanjiku
17th November, 2010

DEDICATION

To my late mum Wanjiku, my constant source of love, hope and encouragement!

ACKNOWLEDGEMENT

The process of writing this thesis has been a wonderful and challenging experience in my academic life. Completion of this study would have not been possible if support and encouragement from different people were not availed to me. Above all, I wish to thank the Almighty God for granting me good health and energy to complete this work.

I am grateful to my family; my niece Wanjiku and my brother Wambugu for all their prayers and emotional support. I would also like to sincerely thank my uncle, Mr. H. N. Nderitu for his support, selflessness and inspiration in my whole life. My cousin Dr. I. Njeri deserves special mention for introducing me to Dr. A.B. Sebitosi who introduced me to the AMES group, UCT. I deeply appreciate his assistance and support.

My sincere appreciation goes to my supervisor Dr. M.A. Khan and my co-supervisor Dr. P.S. Barendse for their assistance and guidance throughout the process of this project. I would also like to thank Mr. C. Wozniack and Mr. P. Titus for their assistance in the laboratory. I cannot forget Mr. Blumeris and his colleagues at Beatech Pty Ltd (SA) for their help in the fabrication of the mechanical machine parts. I also thank Mr. Teixeira for his assistance and patience during the prototyping and testing phase of the machine. I am also grateful to Dr. Ø. Ulleberg and Dr. S. Pasupathi of HySA Sytems, University of Western Cape for sharing their invaluable knowledge in hydrogen related technology. I would also like to recognize the assistance of Mr. Jagau and Mr. Liu in analysing cogging torque.

I am also indebted to Marlene and Nicole of the Department of Electrical, UCT and Carmelita of the Student Wellness Centre, UCT for their assistance during this period. I cannot forget Mrs. Khan and Mr. Ohene Anyang for finding time in their busy schedule to read my work.

I am grateful to my friends Ashwill, Barbz, Ernest, Hartmut, Anneke, Mashele, Lucas, Mumbi and the AMES family. You made my stay in South Africa a truly memorable part of my life.

Finally, am grateful to my friends: Wambugu, Nyambura, Maina, Muhia, Mwenda, Shake, Olang', WaMbio, Jane, Gitonga, Njeri, Gachahi, Karanja, Mwangi, Gathogo, Muchai and Karimi for their emotional and/or financial support.

I also thank the AMES group and the University of Cape Town for funding my studies.

ABSTRACT

The main objective of this study is the selection and design of a wind generator to meet electrolyser requirements. These are the hydrogen production rate, the power requirements and the operating temperature. This requires the analysis of the load, sizing and characterizing of an electrolyser and finally, the design of a wind generator that meets electrolyser requirements. A hybrid system that combines the use of hydrogen as an efficient form of energy storage, and the growing renewable energy (RE) industry is discussed in detail. The sizing of the electrolyser requires the comparison of different electrolyser-load topologies. The loads that are analysed are thermal (lighting and cooking) and electrical. Biogas technology is used in the analysis of thermal loads. After rating the electrolyser, a topology is selected that is applicable to both urban and rural setting. The electrolyser is then characterized by determining the number of cells, the hydrogen production rate, the stack power requirements and the optimum operating temperature range.

The electrolyser power requirements are then used to size the generator. The adopted topology is a twin-rotor-inner-stator axial-flux generator due to its higher power density in comparison to a radial-flux machine. In addition, it allows the use of a parallel-teeth stator which solves the problem of fabricating steel-cored stators in axial-flux machines. Finite element analysis (FEA) is used to compare the performance of this topology with the conventional trapezoidal-teeth topology. Cogging torque analysis on this type of stator structure is also conducted. The effects of different cogging torque minimization techniques, which are considered to be practical to implement with this type of stator are also analysed. These methods include: 3optimisation the pole-arc, teeth-notching and skewing of rotor poles. A pole-arc ratio of 0.72 had the least peak cogging torque of 1.8% of the rated torque. Teeth-notching easily reduced cogging torque for all the pole-arcs with a maximum peak of 2.6% of the rated torque. This was for the topology with a pole-arc ratio of 0.80 whose peak cogging torque is 19.3% of the rated torque. Notching can be easily implemented in this type of stator structure. The topology with a pole-arc ratio of 0.72 and the ones with notched-teeth had the least ripple torque for unity power factor operation.

It was found that the hydrogen production rate and operating temperature of the electrolyser are dependent on current while the efficiency of the electrolyser is inversely proportional to the stack voltage. The parallel-teeth axial flux generator not only met performance requirements, but it also reduced cogging torque inherently. The parallel case had a peak cogging torque of 0.54Nm while the trapezoidal case had 0.71Nm obtained using 3D-FEA. A 2D-FEA methodology for simulating an Axial-Flux machine as an equivalent Radial-Flux machine was also verified. It presented minor

differences which are attributed to the slightly higher flux-density associated with the Axial-Flux machine topology.

A method for holding the teeth in a parallel-teeth stator is also practically implemented. Three PM rotors are tested with this type of stator. These include: a machine with a pole-arc ratio of 0.80, one with alternating pole-arcs of 0.61 and 0.80 and finally one with skewed poles. The effect of pole-shape and area is evident on the results. The experimental RMS values for the no-load voltages for each rotor type are 17.9V, 16.7V and 17V respectively. Their efficiencies are 80%, 78% and 79% respectively. The measured results are comparable to the analytical and/or FEA values. The analytical and/or FEA no-load RMS voltages are 18.1V, 15.7V and 16.8V, while their efficiencies are 83%, 82% and 83% respectively. All the machines met the RMS phase load voltage of 14V at an RMS phase load current of 10A. The alternating pole-arcs topology effectively reduced the cogging torque of the 0.80 pole-arc by 67% while the skewed poles reduce it by 37%. The peak cogging torque for the 0.80 rotor was 8.2% of the rated toque of 6.3Nm.

A method for estimating core-losses and stray load losses is also presented. It is important to point out that steel-cored machine topologies are better placed for small machines where copper losses are more dominant. They have high airgap flux-density which effectively reduces the number of turns. This reduces copper losses which are approximately 50% of the total losses. However, their set-back is the introduction of cogging torque and core losses. Fortunately, this parallel-teeth stator topology reduces cogging torque inherently and core-losses are relatively low for low speed machines. This was proved by the fact that core losses were unaffected by load. Another important aspect is that the analytical and/or FEA and experimental losses were comparable; except for the friction & windage losses whose experimental values were higher. This was due to the strong axial force which is negated in the analytical and/or FEA analysis. This may have contributed to the lower efficiencies in the measured values.

It will be shown that the machine performance would have an effect on the electrolyser. The hydrogen production rate is reduced by 6% for a machine with alternating pole-arcs and in skewed, by 3%. Fortunately, the electrolyser would operate at a reasonable efficiency and temperature for all the machine topologies. It will also be shown that the generator current, with a fairly constant phase voltage, determines the electrolyser current which, in turn, affects the hydrogen production and electrolyser temperature. Lastly the various limitations encountered in this research will be identified and discussed in more details.

Table of Contents

DECLARATION ..... **ii**

ACKNOWLEDGEMENT ..... **iv**

ABSTRACT ..... **v**

Table of Contents ..... **vii**

List of Tables ..... *xi*

List of Figures ..... *xii*

List of Abbreviations ..... *xiv*

List of Symbols ..... *xv*

1 Introduction **1**

1.1 Background *1*

1.2 Literature Review *2*

1.2.1 Hydrogen Production Using Renewable Energy 2

1.2.2 Energy Storage 3

1.2.3 Electrolyser 6

1.2.4 Wind Energy Conversion Systems (WECS) 8

1.2.5 Permanent Magnet Synchronous Generators (PMSG) 9

1.2.6 Cogging Torque 10

1.3 Research Questions *11*

1.4 Objectives *12*

1.5 Scope and Limitations *12*

1.6 Research Significance *13*

1.7 Thesis Organization *13*

2 Overview of Hydrogen Technology **14**

2.1 Fuel Cells (FCs) *14*

2.1.1 Operation of a Fuel Cell 15

2.1.2 Fuel Cell Models 17

2.2 Hydrogen Storage *19*

2.2.1 Compressed Hydrogen 19

2.2.2 Liquid Hydrogen (LH_2) 19

2.2.3 Metal Hydride ... 20
2.3 Electrolysis of Water ... *21*
2.3.1 Operation of an Electrolyser ... 21
2.4 Types of Electrolysers ... *24*
2.4.1 Alkaline Electrolysers ... 25
2.4.2 PEM/SPE Electrolysers ... 26
2.4.3 Solid Oxide Electrolysers or Steam Electrolysers ... 27
2.5 Electrolyser modelling equations ... *27*
2.5.1 Empirical Models ... 27
2.5.2 Analytical Models ... 28
2.6 Conclusions ... *33*
3 Small-Scale Use of Hydrogen and Electrolyser Sizing & Characterization ... 35
3.1 Load Characterization ... *35*
3.1.1 Thermal Loads ... 35
3.1.2 Electrical Loads ... 38
3.2 Electrolyser System Configurations ... *39*
3.2.1 ELY-Biogas Combination ... 39
3.2.2 ELY-FC Combination ... 40
3.2.3 ELY-FC/H_2 Storage Combination ... 41
3.3 Electrolyser Characterization ... *43*
3.4 Generator - Electrolyser Interface ... *46*
3.5 Conclusions ... *51*
4 Axial-Flux Topologies and Analytical Modelling ... 52
4.1 AFPM Topologies ... *52*
4.1.1 Single-sided AFPM Machines ... 52
4.1.2 Double-sided AFPM Machines ... 53
4.1.3 Multi-disc AFPM Machines ... 54
4.2 Magnetic Circuits ... *55*
4.2.1 Demagnetization Characteristic of a PM Material ... 56
4.2.2 Approximate Calculation of Flux ... 57
4.2.3 Nonlinear Calculation of a Magnetic Circuit ... 59
4.3 Torque Production ... *60*
4.3.1 Magnetic Flux ... 60
4.3.2 Electromagnetic Torque and EMF ... 61

4.3.3 Pulsating Torque 62

4.4 PM Machine Windings *63*

4.4.1 Three-Phase Winding Distribution in Slots 64

4.4.2 Winding Factor and EMF Harmonics 65

4.4.3 Pole-Slot Combinations for Concentrated PM Windings 67

4.4.4 Synchronous Reactance 67

4.5 Losses and Efficiency *69*

4.5.1 Stator Winding Losses 69

4.5.2 Stator Core Losses 70

4.5.3 Rotational Losses 70

4.5.4 Efficiency 71

4.6 Sizing Equations for Diameters, Current Loading, Magnet Depth, Rotor Back Iron Thickness and Power Density *72*

4.7 Conclusions *74*

5 Design and Analysis of an Axial-Flux Generator 75

5.1 Machine Design *75*

5.1.1 Number of Poles and Slots 75

5.1.2 Phase Voltage and Phase Current 77

5.1.3 Magnet Grade 77

5.1.4 Tooth and slot width 78

5.2 Machine FEA Analysis *80*

5.2.1 Modelling of an AFPM Machine as an Equivalent RFPM Machine 83

5.2.2 Flux Density Distribution 85

5.2.3 Back-EMF 86

5.2.4 Quasi-3D Analysis of Cogging Torque 88

5.2.5 Cogging Torque Minimization Techniques 90

5.2.6 Developed Torque 93

5.2.7 Analytical and FEA Estimation of Machine Performance parameters 94

5.3 Conclusions *97*

6 Prototyping and Testing 99

6.1 Prototyping *99*

6.1.1 PM Rotor Discs 100

6.1.2 Stator Structure 100

6.2 Experimental Results *104*

6.2.1 Back-EMF 104

6.2.2 No-load Losses 106

6.2.3 Core Losses 107
6.2.4 Stray Load Losses 108
6.2.5 Terminal voltage 109
6.2.6 Efficiency 110
6.2.7 Cogging torque 110
6.2.8 Temperature response of the Machine 113
6.3 Comparison of Results 115
6.4 Electrolyser Requirements and Machine Performance 117
6.5 Conclusions 119
7 Conclusions and Recommendations 120
7.1 Conclusions 120
7.2 Recommendations 122
References 124
Appendices 129
Appendix A: Conversion Parameters and Safety Statistics for Hydrogen and other Fuels 129
Appendix B: WECS, WECS-ELY Interface and ELY Simulink® Model 130
Appendix C: Winding Layouts and Factors for different Pole-Slot Combinations 131
Appendix D: Comparison of Some Silicon Steels 132

List of Tables

Table 1.1 Comparison of small-scale energy storage methods 4
Table 2.1 Thermodynamic quantities for H_2, O_2 and H_2O 16
Table 2.2 A summary of some common fuel cells and their applications [2] 17
Table 2.3 Hydrogen storage methods [36] 20
Table 2.4 PEM/SPE electrolyser parameters [40] 32
Table 2.5 Thickness of Nafion® membranes [45] 32
Table 3.1 Heating values for various fuels and their replacement [46] 35
Table 3.2 Quantity of biogas required for specific applications [46] 36
Table 3.3 Electrolyser ratings for ELY-H_2 storage set-up 42
Table 3.4 A comparative summary of electrolyser ratings for different load scenarios 44
Table 5.1 Comparison of various pole-slot configurations 76
Table 5.2 Analytical machine parameters 80
Table 5.3 Effect of cogging torque minimization on machine performance for all trapezoidal case 95
Table 5.4 Performance of machines with parallel-teeth 96
Table 6.1 Core losses in some machine steels 100
Table 6.2 Cogging torque experimental values 112
Table 6.3 Comparison of analytical, FEA and experimental results 115
Table 6.4 PEM electrolyser performance parameters under rated machine parameters 117
Table A.1Conversions parameters 129
Table C.2 Winding factor for different number of poles, p and slots Q_s combinations [31] 131
Table C.3 Winding layouts [31] 132

List of Figures

Fig 1.1 H_2-SAPS concept 3
Fig 1.2 Comparison of energy and power densities for different energy storage methods [6] 4
Fig 2.1 Fuel cell concept 15
Fig 2.2 PEMFC stack (16 cells, 500W, 50A, and around 11V) [35] 16
Fig 2.3 Operation of different types of FCs [36] 17
Fig 2.4 FC characteristic; $V_{cell} = U_{FC}$; $E_o = U_{OCV}$; $J = i$ [37] 18
Fig 2.5 An alkaline electrolyser cell 22
Fig 2.6 Alkaline electrolyser designs [1] 25
Fig 2.7 A PEM electrolyser [41] 26
Fig 2.8 Typical voltage-current curves for an electrolyser cell at high and low temperatures [17] 28
Fig 2.9 Experimental (□) and exponential equation (-): $I = 0.00009 \exp(0.29285E)$ [42] 28
Fig 2.10 Equivalent circuit of an electrolyser cell 29
Fig 2.11 Experimental data at 80°C (1:U_{OCV}, 2:U_{ohm}, 3: U_c, 4: U_a on Pt-IrO2, 5: U_a on Pt) [40] 30
Fig 3.1 Flame heights as a function of thermal power [53] 37
Fig 3.2 Energy requirements for H_2/Biogas blending ratios by volume and by energy 38
Fig 3.3 A 24-hour rural village load profile [54] 38
Fig 3.4 Electrolyser parameters vs. cell voltage for $\eta_c = 11$ cells at $I_{ely} = 52$A at a H_2 production 46
Fig 3.5 Response of the Simulink® model to a ramp wind-speed input 49
Fig 3.6 Response of the Simulink® model to a varying wind-speed input 50
Fig 4.1 Single-sided AFPM structure [22] 52
Fig 4.2 Flux path in an AFIR machine [22] 53
Fig 4.3 Flux paths in a TORUS machine [22] 54
Fig 4.4 A slotless multi-disc machine for $n = 3$ [22] 54
Fig 4.5 Magnetic equivalent circuits 55
Fig 4.6 B-H characteristic of a permanent magnetic material [61] 56
Fig 4.7 Effects of temperature on the demagnetization characteristic [61] 57
Fig 4.8 Magnetic circuit of a twin rotor- internal stator AFPM 58
Fig 4.9 Winding layouts for a 4-pole RFPM 64
Fig 4.10 k_{p1} and k_{w1} vs. q for $Q_s = 12$ slots, $p = 5$ pole pairs and $m_1 = 3$ phase 66
Fig 4.11 Tooth and slot dimensions; slot-width, w_s; tooth-width, w_t; slot-pitch, τ_s 68
Fig 5.1The power flow diagram for a WECS-ELY system 75
Fig 5.2 Interaction of teeth and poles in an axial-flux machine 81
Fig 5.3 Flux density distribution in an AFPM machine 82
Fig 5.4 Flux density distribution in an RFPM machine 82
Fig 5.5 Models in Flux environment; Isolines show the flux density in the 2D model 83
Fig 5.6 Pole slices 84
Fig 5.7 Normal and tangential flux-density components 86
Fig 5.8 Back-EMF results at D_g and for $N = 3$ slices for an AFPM machine and its equivalent RFPM machine 87

Fig 5.9 Back-EMF results at D_{g1}, D_{g2} and D_{g3} for the equivalent RFPM machine 87
Fig 5.10 Comparison of load voltage and cogging torque in 2D and 3D-FEA 88
Fig 5.11 Quasi-3D cogging torque analysis for three slices 89
Fig 5.12 Application of quasi 3D-FEA to 3, 6 and 10 planes 90
Fig 5.13 Methods of minimizing cogging torque using the equivalent RFPM methodology 91
Fig 5.14 2D-FEA cogging torque results 92
Fig 5.15 3D-FEA cogging torque results 93
Fig 5.16 Torque developed 94
Fig 5.17 Power flow diagram in a PMSG 94
Fig 5.18 Performance comparison of the equivalent RFPM machine with the AFPM machine 96
Fig 6.1 PM rotor discs 100
Fig 6.2 Holding of the teeth 101
Fig 6.3 The actual fabricated teeth holding structure 101
Fig 6.4 Assembly of parallel-teeth stator and dummy stator 102
Fig 6.5 Assembly and disassembly rig 103
Fig 6.6 AFPM generator mounted on the test rig 103
Fig 6.7 Induced no-load voltages of a machine with a pole-arc ratio of 0.80 104
Fig 6.8 No-load voltage harmonics at 50Hz 105
Fig 6.9 Experimental phase back-EMF 106
Fig 6.10 No-load losses 106
Fig 6.11 Core losses at no-load 108
Fig 6.12 Core loss constant as a function of shaft speed 108
Fig 6.13 Stray load losses at 600rpm and 50Hz 109
Fig 6.14 Terminal voltage at a rated speed of 600rpm and 50Hz 109
Fig 6.15 Efficiency at a rated speed of 600rpm and 50Hz 110
Fig 6.16 Oscilloscope cogging torque results 111
Fig 6.17 Scale balance method 111
Fig 6.18 The FFT method 112
Fig 6.19 Experimental cogging torque waveforms 113
Fig 6.20 Temperature response of the machine 114
Fig 6.21 Comparison of experimental and 3D-FEA cogging torque values 116
Fig 6.22 Comparison of 2D-FEA and experimental load performance for a pole-arc ratio of 0.80 117
Fig 6.23 Electrolyser performance parameters as a function of voltage regulation 118
Fig 6.24 Electrolyser parameters for H_2(g/hr) = 6.4g/hr with a generator phase current of 10A and a phase voltage of 15.2V 118
Fig B.1 Simulink® model 130
Fig D.2 DC magnetization curve for M310-50A 132
Fig D.3 DC magnetization curve for M350-50A 133
Fig D.4 DC magnetization curve for 50H270 133

List of Abbreviations

AFPM	Axial-Flux Permanent Magnet machine
atms	A unit for pressure, atmospheres
Btu	British thermal unit
Cal	A unit for energy, Calories
CHP	Combined Heat and Power generation
CNG	Compressed Natural Gas
D	Duty ratio
EES	Electrical Energy Storage
ELY	Electrolyser
EMF or E_f	Electro Motive Force or the no-load voltage
F	Faraday's constant (= 96,485 C/mol or As/mol)
FC	Fuel Cell
FCV	Fuel Cell Vehicles
FEA	Finite Element Analysis
FFT	Fast Fourier Transform
gcd	Greatest Common Divisor
GHG	Green House Gases
H_2	Hydrogen
HAWT	Horizontal Axis Wind Turbine
HHV	High Heat Value
ICE	Internal Combustion Engine
KOH	Potassium Hydroxide
kW	kilo Watt
kWh	kilo Watt hour
LCM	Least Common Multiple
LH_2	Liquid Hydrogen
LHV	Low Heat Value
MEA	Membrane Electrode Assembly
MMF	Magneto Motive Force
MPPT	Maximum Power Point Tracking
NdFeB	Neodymium-Iron-Boron magnets
Nm^3	Normal metres cubic
NO_x	Nitrogen Oxides
OCV	Open Circuit Voltage
PC	Permeance coefficient
PEM	Polymer Electrolyte Membrane or Proton Exchange Membrane
PMSG	Permanent Magnet Synchronous Generator
R	Universal gas constant (= 8.3144J/mol)

R&D	Research and Development
RE	Renewable Energy
RFPM	Radial Flux Permanent Magnet machine
RMS	Root Mean Square
SAPS	Stand Alone Power Systems
SMC	Soft Magnetic Composites
SmCo	Samarium Cobalt magnets
SPE	Solid Polymer Electrolysers
TSR or λ	Tip Speed Ratio
TWh	Terra Watt hour
WECS	Wind Energy Conversion Systems

List of Symbols

Symbol	Unit	Definition
$\varepsilon = E_f / V_{an}$		Voltage regulation
ϕ_g	Wb	Airgap flux
ϕ_p	Wb	Flux per pole
ϕ_l	Wb	Leakage flux
ϕ_M	Wb	Magnet flux
ϕ_r	Wb	Remanent flux
$A_{elc}/A/A_c/A\text{-}MEA/A_{MEA}$	cm^2	Active area of the electrolyser or fuel cell
A_g	m^2	Airagap area
a_{H2O}		Water activity (=1 for liquid water)
$A_{M/pm}$	m^2	Pole area
A_p	m^2	Pole-pitch area
A_s	A/m	Current loading
A_{slot}	m^2	Slot area
$B_{1\max}$	T	Specific magnetic loading
B_{cr}	T	Maximum rotor core flux-density
B_{cs}	T	Maximum stator core flux-density
$B_{g/ave}$	T	Airgap flux-density
B_k	T	Knee flux-density
B_{mg}	T	Plateau value of the magnetic flux density
B_r	T	Remanent flux-density

C_p		Power coefficient
C_Φ		Flux focusing or concentrating factor ($=A_M/A_g$)
D_{cond}	m	Conductor diameter
d_e	m	Distance between electrodes
D_x	m	Diameter; $x = i, g, o$
F		Periodicity of the basic winding element
f	Hz	frequency
F_c	A-turns	Coercive MMF
f_{LKG}		Flux leakage coefficient
G	J	Gibbs free energy
g	mm	Airgap
H	J	Enthalpy
H_c	Wb/m^2	Magnetic field intensity
i or j	A/cm^2	Current density
I_a	A	Armature current
i_d	A	d-axis current
I_{ely}	A	Electrolyser stack current
i_q	A	q-axis current
$I_{s(rms)}$	A	The RMS Stator current
k_C		Carter's coefficient
$K_c(f)$	$W/(Wb\text{-}turns)^2$	Core loss constant
k_d		Ratio of inner diameter to outer diameter
k_{dn}		Distribution factor
k_{pn}		Pitch factor
K_s		Stacking factor
k_{sf}		Slot fill factor
k_{skew}		Skew factor
k_{W1}		The fundamental winding factor
L_e	m	Effective length
l_m	m	Magnet depth
L_r	m	Axial depth of the whole rotor
L_{rc}	m	Axial depth of the rotor iron
L_s	H	Synchronous inductance
L_{stk}	m	Machine stack length
m_1		Number of phases
n or n_{rpm}	revs/min	Shaft speed
n_c		Coils per phase
N_c		Conductors per coil
N_L		LCM(Qs,2p)
N_{ph}	turns	Number of turns in series per phase

n_s	revs/sec	Shaft speed
N_{sl}		Conductors per slot
p		number of pole pairs
P	atms	Pressure
P_{ag}	W	Airgap power
P_{Cu}	W	Copper losses
P_{Fe}	W	Core losses
P_{gen}	W	Generator power
P_{in}	W	Input power
P_{out}	W	Output power
$P_{PM\text{-}rotor}$	W	PM rotor core losses
$P_{rot/F\&W}$	W	Rotational or friction & windage losses
P_{stray}	W	Stray load losses
P_{WT}	W	Wind turbine power
P_{x2}	atms	Partial pressure; $x = H$ or O
q		Slots/pole/phase
Q		Number of slots per pole
Q	J	Heat
Q_c		Number of coils
Q_s		Number of slots
R	A-turns/Wb	Reluctance
R	m	Turbine radius
R_{core}	A-turns/Wb	Rotor iron core reluctance
$R_{dc/ph/ac}$	Ω	Phase resistance
R_{ely}	Ω	Liquid electrolyte resistance
R_g	A-turns/Wb	Airgap reluctance
R_L	A-turns/Wb	Leakage reluctance
R_p	A-turns/Wb	Internal reluctance
R_{stator}	A-turns/Wb	Stator reluctance
S	J	Entropy
T	°C	Temperature
T_{cog}	Nm	Coggign torque
T_d	Nm	Torque developed
t_m	cm	Membrane thickness
U	J	Internal energy
U_{ely}	V	Electrolyser stack voltage
U_{FC}	V	Fuel cell stack voltage
U_x	V	Overvoltage; $x = a, c, ohm, OCV, rev, tn$
V	m^3	Volume
V_{an}	V	phase voltage

V_d	V	Input voltage of the buck-boost converter
v_m	m/s	Mean wind speed
V_o	V	Output voltage of the buck-boost converter
W_{airgap}	J	Energy within the airgap
w_o	m	Slot opening
w_s	m	Slot-width
w_t	m	Tooth-width
w_{tip}	m	Tooth-tip width
X_s	H	Synchronous reactance
y	m	Coil-pitch
z		Number of electrons transferred per mole
α		Transfer coefficient
α_i		Pole-arc ratio
η	%	Efficiency
η_c		number of electrolyser cells
η_{convr}	%	Buck-boost converter efficiency
η_F	%	Faraday efficiency
η_{gen}	%	Generator efficiency
η_{rect}	%	Rectifier efficiency
$\eta_{sys\text{-}eff}$	%	Overall system efficiency
θ	degrees or rads	Rotor angle
λ_m		Water content
$\lambda_{s/PM}$	Wb-turns	Flux-linkage
μ_o	H/m	Permeability of free space
μ_{rec}		Relative recoil permeability
ρ	kg/m3	Density of air
$\sigma_{k/m}$	S/cm	Electrical conductivity of the electrolyte
τ_p	m	Pole-pitch
τ_s	m	Slot-pitch
ω_m	rads/sec	Mechanical angular speed

1 Introduction

1.1 *Background*

The global consumption of fossil fuels is increasing at an alarming level. The energy crisis is compounded by diminishing resources, global warming effects, increased population and industrialisation of rapidly developing countries. These effects can be mitigated by harnessing energy from renewable sources which have negligible environmental effects like wind, solar, tidal wave, hydro etc. Conservation of energy is particularly encouraged when it is obtained from intermittent renewable sources. Most of the rural areas in Africa are yet to be connected to the grid despite the existence of rural electrification programs and the situation is expected to worsen as the demand for electricity grows. The provision of electricity by means of stand-alone systems will therefore be one of the viable options for improving livelihoods in rural Africa.

This study considers a wind-electrolysis plant where wind energy is stored in form of hydrogen. The main advantages of hydrogen are its flexibility in end use and its ability to replace fossil fuels in internal combustion engines. Hydrogen can be converted into other forms of energy. It can be converted to electrical energy by means of fuel cells, thermal energy for space heating, enriching natural gas and also cooking and lighting by blending it with biogas fuel. Hydrogen is economically derived from methane. This implies that the benefits of using hydrogen are lost if fossil fuel sources are used without carbon capture, which further increases the cost of producing hydrogen. Renewable sources are well suited for generating hydrogen due to their abundance availability in most regions. This could result in lower dependence on fossil fuels and the improvement of the social well being of communities by diverting funds meant for oil imports into social development projects. The renewable energy sector would be stimulated further economically and technologically by the adoption of green or clean energy solutions.

This study will therefore focus on the small-scale use of hydrogen in a rural context where hydrogen can supply thermal (lighting and cooking) or electrical loads. The sizing of a small wind electrolysis plant is assessed in the context of a typical rural application. A PMSG is then developed for direct coupling to a small wind turbine. An axial-flux PMSG with a stator core is selected due to its higher power density in comparison to a radial-flux machine, and other advantages. The drawback of this topology is associated with the manufacture of the stator cores, without shorting-circuiting the

laminations. This can be overcome by using pre-formed soft magnetic composite (SMC) teeth or a yoke-less parallel-teeth stator.

In SMC core, the teeth are formed from a composite material with 3D-electromagnetic properties. They are then fitted onto a laminated yoke. This type of core has assembly and electromagnetic problems. The electromagnetic problems are easily solved by the parallel-teeth topology which uses a twin rotor-inner stator topology. This topology eliminates the need for a stator yoke but presents a challenge of holding the teeth. This thesis addresses the challenge of designing and prototyping an axial–flux generator with parallel-teeth that meets requirements of a small wind-electrolysis plant for rural application.

1.2 *Literature Review*

In this section, the sub-systems of a wind-electrolysis plant are discussed in details. These include: the production of hydrogen using renewable energy, comparison of different types of small-scale energy storage, electrolyser operating modes and wind energy conversion systems (WECS). Different methods of minimizing cogging torque in axial-flux machines are also compared.

1.2.1 Hydrogen Production Using Renewable Energy

The global energy needs are increasing with diminishing availability of traditional non-renewable sources. Most of this energy is from fossil fuels. For instance, in the United States, 17.3×10^{15} Btu of gasoline and 12.9×10^{15} Btu (3,717 TWh) of electricity were consumed in 2004 [1]. This trend is similar in many countries. The situation is exacerbated if rapidly developing countries like China, India, Brazil, among others are considered. Fossil fuels also contribute to global warming and adverse economic and political policies. An urgent need therefore exists to reduce dependence on fossil fuels and provide alternative sources of energy in addition to energy security for sustained development. This is reiterated by the United Nations Intergovernmental Panel on climate Change (IPCC) [2].

Renewable energy is considered to be a viable alternative source of energy. It is environmental friendly and abundant in most locations. Over 70% of oil deposits are in OPEC countries, while developing countries are rich in RE [2]. Developing countries can realize growth by channelling finances meant to meet their fossil fuel needs to social development projects. It is important to note that about 90% of Africa's population is off-grid with South Africa accounting for 17% [3]. In addition to rural electrification programs, Stand Alone Power Systems (SAPS) offer a good solution

to rural power needs which are far from the grid. They can power small (10-100W), medium (0.1-10kW) and large (10-100kW) loads [3]. The effectiveness of SAPS can be realized when energy saving and efficiency and adoption of emerging technologies like white LEDS for lighting are incorporated. This will effectively reduce the overall load of the system.

The H_2-SAPS concept is shown in Fig 1.1. From the figure, renewable sources can be integrated into a hybrid system to reduce their inherent intermittency. This can be achieved by combining two or more sources (e.g. solar and wind) and incorporating both short term storage (e.g. a battery bank) and long term storage facilities (e.g. hydrogen storage). The energy from the RE source can power electrical loads directly, with the excess diverted to the electrolyser. Alternatively, it can be a dedicated system where all the energy is supplied to the electrolyser. Hydrogen from the electrolyser can then be fed directly to the fuel cells or it can be stored for peak shaving or for back-up when energy from the RE source(s) diminishes. Hydrogen can also be combusted for thermal energy. Long-term hydrogen storage components (bounded by the dashed rectangle in Fig 1.1) include: the electrolyser, hydrogen storage and fuel cells. To improve the efficiency of the system, combined heat and power (CHP) generation or cogeneration can be used to generate electricity to meet electrical loads, whilst the waste heat can be used for space heating.

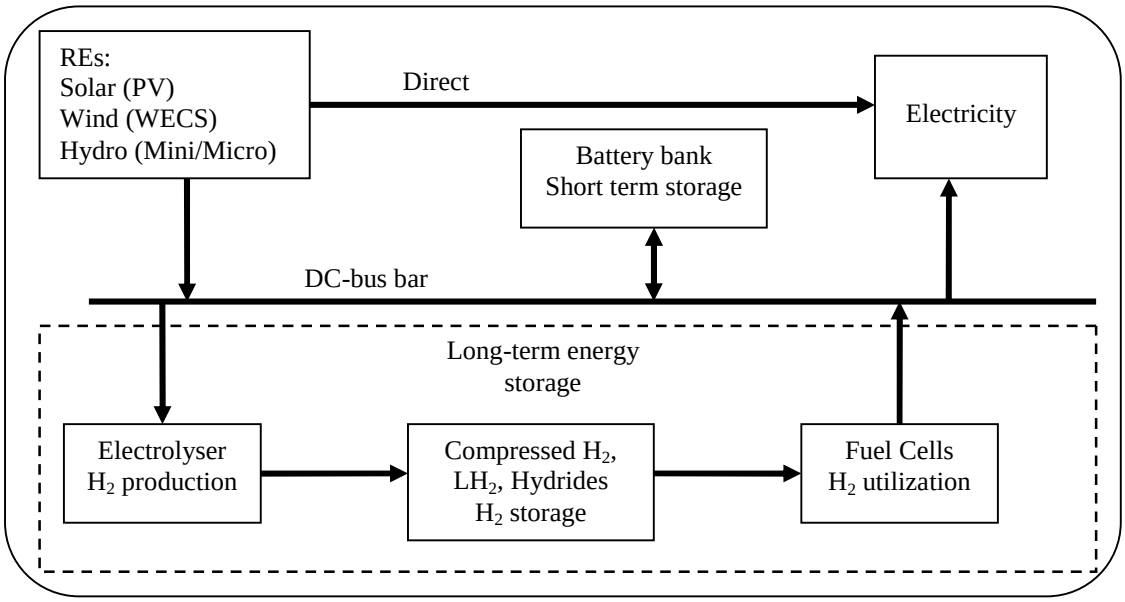

Fig 1.1 H_2-SAPS concept

1.2.2 Energy Storage

Energy can be stored in pumped hydro facilities, flywheels, electrochemical batteries, super capacitors/ultra capacitors and as H_2, among other methods. H_2 is the most flexible, environmentally

friendly, and the most cost effective method for power applications over 5kW and long term storage [4], [5]. Energy storage associated with RE sources should have a high cycle life – charging and discharging cycles, high capacity at low rate of discharge, good reliability under transient conditions, high power efficiencies at different states of charge (SOC), long life and low maintenance requirements and a wide temperature operating range [3]. A comparison of energy and power densities for different energy storage methods is shown in Fig 1.2. A further comparison of small-scale energy storage options is presented in Table 1.1. It can be seen that there is no particular storage method can meet all the requirements for a RE storage system. It is therefore common to have a hybrid system.

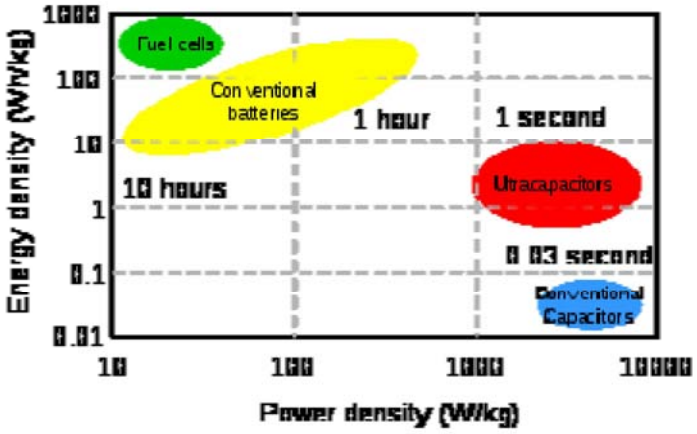

Fig 1.2 Comparison of energy and power densities for different energy storage methods [6]

Table 1.1 Comparison of small-scale energy storage methods

Storage	Mode of operation	Advantages	Disadvantages
Rechargeable batteries or accumulators Refs [7], [8], [9]	Convert stored chemical energy to electrical energy. The process is reversible	High efficiencies (91-95%) for short-storage periods Convenient for charging and recharging cycles Inexpensive and simple to manufacture Mature and well proven technology Well suited for buffering transients - smoothing the bus voltage	Low energy density in comparison to H_2 storage Decomposition of water into H_2 and O_2 requires regular topping with distilled water and electrolyte to maintain electrolyte concentration Corrosion, depletion of the active material and growth of the positive electrode especially in sealed lead acid batteries Batteries are also self discharging (1-5% of their stored energy per hour) Formation of insoluble compounds due to intermittent and/or low charging (opportunity charging)
	These limitations reduce their service life making them to be inefficient for medium and larger power applications.		

Flywheels	A mechanical battery that stores kinetic energy. The flywheel is 'charged' by rotating it using an electric motor and this energy is extracted by the same motor which now serves as a generator.	High turn-around efficiency High specific power than batteries Long life High output power They are relatively unaffected by ambient temperature.	The need to operate in an evacuated environment and safety containment raises capital costs. Evacuation introduces thermal problems in the design of the electrical machine. It is a less mature technology compared to electrochemical batteries for SAPS applications The current flywheels have low specific energy and they are expensive compared to batteries.
	Flywheels are one of the promising ways of replacing lead acid batteries. They will find applications in automobiles and in SAPS systems. Recent advances in composite materials have renewed the interest in flywheels.		
Super/ultra/ electric double layer capacitors Ref [6]	They are similar to common capacitors but they have higher capacitance. They use special electrodes and electrolytes hence they are a hybrid between capacitors and electrochemical cells.	They have an unlimited cycle life High efficiency Compact design Rapid charging due to their low impedance.	Low energy density which is much less than that of electrochemical batteries Low voltage per cell which requires series connection to realize higher voltages. Voltage balancing is necessary if more than three capacitors are connected in series They have high self-discharge than that of electrochemical batteries
	Applications - meeting transient demands, smoothing and filtering pulsed load currents, used in memory back-ups and power back-up systems. *Their high cycle life makes them to be fit for meeting transient demands hence they are used together with other storage means like batteries. This reduces the cycle times of the batteries significantly, enhancing their service life.*		
Hydrogen	Water is split into hydrogen and oxygen in an electrolyser. Hydrogen which is an energy carrier is stored and converted to either thermal energy by burning or electrical energy in a fuel cell.	Allows transportation of large amounts of energy at much higher densities Can replace fossil fuels - finds application in most areas where fossil fuels are used It is efficiently converted to other useful forms of energy than fossil fuels Clean if obtained from RE sources	Less mature technology than battery technology for SAPS systems Has low energy density by volume High capital cost High cycle time affects the service life of electrolysers
	H_2 will be part of the energy carriers in future and as such there is need to lower its capital cost and continued R&D especially in the field of H_2 storage		

Power conditioning circuits are used to interface elements in a SAPS system. Solar and wind systems may employ maximum power point tracking (MPPT) algorithms to ensure maximum power is

captured from the highly varying RE source. An electrolyser was directly coupled to photo-voltaic (PV) panels in [10]. The results compare well with that of an electronic MPPT for a PV-H_2 system. The advantage of direct coupling is higher efficiency, but with more transients due to the intermittency of the source. These transients are due to instantaneous loads, spikes, electrolyser transients and energy peaks.

1.2.3 Electrolyser

When adopting electrolysers for RE applications, they are required to be highly robust. It is important to point out that most electrolysers are designed for constant mode operation which does not account for variable mode operation. Reference [11] presents an analysis for a PEM electrolyser designed for RE applications. In this case, the feed water was not heated and it was shown that it is possible to attain the operating temperature range of 80-100°C by regulating the current density.

An electrolyser can be operated in either constant/fixed power mode or non-constant/variable power mode. Constant power operation leads to high efficiencies due to operation at a high capacity factor according to [12], [13]. Variability of the electrolyser power reduces its service life by increasing internal wear, impurities and energy losses [7]. Constant power input can be achieved by use of a battery which absorbs transients maintaining the DC bus bar voltage at a predetermined value. DC/DC converters meet the voltage ratings of the electrolyser and fuel cells. An inverter is provided at the output to feed AC loads.

The effect of variable power mode on electrolyser degradation is a matter requiring in-depth studies. Electrolyser degradation may be due to poor stack assembly, delamination or debonding at membrane-electrode interfaces, contamination and dehydration of the membrane for PEM electrolysers. It can also be due to an increase in contact resistance between electrodes and interconnecting plates due to surface oxidation and the mode of power operation which affects the operating temperature of the electrolyser [10], [13]. It is important to maintain the operating temperature within the operating range of the electrolyser. This ensures efficient operation and also prolongs the life of an electrolyser by reducing the corrosion of the membranes and electrodes [14].

An alkaline electrolyser (26kW; 7 bars) was run under a fixed and variable mode operation [13]. There was a reduced number of start and stop cycles in the variable mode. This was projected to increase the life of the electrolyser. In fixed mode, below a certain set operating point, the electrolyser was switched off, whereas for the variable mode as long as the source was able to supply the idling current, the electrolyser remained operational. In this set-up, the variable mode gave the best

performance. Most alkaline electrolysers are designed to operate at least at 20% of their rated power [13], ensuring variable power mode operation.

Another test on an alkaline electrolyser (220kW; 30 bars; 70 cells) was done in [15], however the findings were contrary to [13]. The variable power mode was less efficient than the constant power mode except for increased constant load demands (17-20%). The amount of wind energy converted to hydrogen was 23% for the non-constant mode while in the constant mode it was greater than 28%. This can be attributed to the operation of the electrolyser in the high capacity region by ensuring constant operating conditions as noted earlier. The non-constant mode of operation can be used to analyze the performance and behaviour of an electrolyser [15].

In summary, the operating characteristic of a given electrolyser cannot be generalized to other electrolysers. The operation performance is dependent on electrolyser type, temperature, electrodes' constituents, type of membrane, the electrolyte employed etc. The above discrepancy ([13] and [15]) shows a lack of technical data and operational experience in this field and more needs to be done to understand parameters governing the service life of electrolysers.

Examples of stand-alone power system projects are: the PHOEBUS project in Jülich, Germany, which demonstrated for ten years a PV-H_2 for a library [16] [17], HYSOLAR project which is a test and research facility in Stuttgart, Germany in partnership with Saudi Arabia [17]. A hybrid system (wind and PV) at El-Hammam site, Egypt demonstrated the use of Fuzzy Logic Control (FLC) for energy flow and management. Hydrogen was used as a back up when the wind and PV power were low [18]. A SAPS for a low energy dwelling was demonstrated at Trondheim, Norway which showed that the size of the solar-hydrogen infrastructure is dependent on solar insolation. The study also recommends the reduction of both thermal and electrical loads and the use of cogeneration (CHP) to improve on efficiency and a reduction in components' sizes [8]. A hybrid (wind and solar) SAPS for a remote communication station is described in [9], where H_2 is produced from an excess of the renewable energy. This is the case for most projects, except in cases where H_2 is the desired end product like fuel for hydrogen vehicles.

Demonstration projects have proved the feasibility of hydrogen technology from a technological point of view and a lot of R&D is being conducted. For instance, the Norwegian government has spent € 1.7 million on the Utsira project which serves to evaluate the production of hydrogen using wind power. The Greek Center for Renewable Energy Sources (CRES) is focusing on the use of RE for producing hydrogen, while in Australia, R&D is underway on the use of solar electrolysis for both the public and private sector. Research is also being done in Turkey on the use of Boron as a hydrogen carrying media in fuel cells. R&D is also being done in Europe, US, Japan among other countries [7].

In 2008, South Africa established a Hydrogen Centre of Competence to focus on hydrogen production, storage, delivery and distribution in the North-West University (NWU) [19]. It has also established a centre that focuses on fuel cells - Hydrogen South Africa (HySA Systems) which is based at the University of Western Cape (UWC). This demonstrates a worldwide commitment to utilise hydrogen as one of the future energy carriers.

1.2.4 Wind Energy Conversion Systems (WECS)

Wind power was one of the main sources of energy in the first half of the 20th century. It was used for sailing, grinding and pumping water. This changed in the 1960s with the use of cheaper fossil fuels which made wind power technology expensive. It saw a comeback in the 1970s due to rising fuel prices [20] and recently due to the adverse environmental effects of fossil fuels. This has led to development of wind turbines in the megawatt range. These include the American MOD-2; 2.5MW, the Swedish-American WTS-4; 4MW, the German GROWIAN; 3MW among others [20]. The first mass production of wind power plants was started by a German constructor, Allgaier in the early 1950s to supply off-grid homes and some of these plants are still operational even after more than 50 years of service [20].

The advent of power electronics is contributing to a shift from fixed-speed systems to variable-speed systems. This reduces the loading on drive trains; reducing their sizes significantly and operation at various wind speeds leads to capturing of more energy. It also allows the control of power. The trend now is to shift towards gearless systems by adopting direct-drive permanent magnet synchronous generators (PMSG). According to [21] the gear box is the most complex component of the system. Eliminating it improves on reliability by reducing complexity which lowers maintenance and service costs.

PMSG are relatively compact and light weight which allows for conventional transportation and installation with high power density. In addition they are cost effective by having a reduced number of parts, lower maintenance and service costs [20], [21]. For instance, Siemens recently launched a gearless SWT-3.0-101 direct drive wind turbine with a rated power of 3MW. It offers 25% more power than the 2.3MW with half the parts of a conventional wind turbine and much less than half the number of moving parts. It has reduced complexity thereby improving reliability and profitability [21]. Other examples are the Enercon E 40 in the 500kW class and Harakosan Z72 which has a 2MW nominal output [20]. PMSG can also be adapted for higher MW range in slow-running turbines. This can be achieved by combining the high torque generators with a single-stage gear box making it possible for units in the 5MW range [20]. The penetration of PMSG into the market is due to

favourable prices of high quality hard magnetic materials, the versatility of designing a high number of poles around the rotor or stator and high efficiencies at partial load range [20]. Its reduced complexity, improved reliability, reduced number of parts and lower maintenance costs, makes PMSGs a profitable venture and therefore the number of installed units is expected to grow. The PMSG also negates the need for start up or excitation unlike other machines such as the doubly-fed asynchronous machine and a wound field synchronous generator.

1.2.5 Permanent Magnet Synchronous Generators (PMSG)

PMSG direct driven machines are more reliable and efficient due to the elimination of the gear box, excitation systems, reduced rotor losses (they do not have rotor windings) and they are considered to be more compact. They include the Radial Flux PM Machines (RFPM), the Axial Flux PM Machines (AFPM) and the Transverse Axial Flux PM (TAFPM) machines. RFPMs have higher power density and higher torque per ampere ratio than asynchronous machines and the transfer of heat from the stator frame is better allowing relatively high machine electrical loading [22]. The disadvantages of PMSGs include cogging torque inherent in slotted PM machines and the need to hold the magnets so that the rotor does not fly apart. Transverse machines have high torque ripple, their structure is complex with three dimensional magnetic fields which makes fabrication difficult and expensive. They also have a low power factor [23].

AFPM machines have more advantages than the rest of the machines. These includes: high torque/power density, less ripple and cogging torque, easily adjustable airgaps, less noise and vibrations and a wide variety of topologies by varying the direction of the main airgap flux [22], [24], [25]. A dual-rotor RFPM machine was reported by [26] to have a higher torque density than an equivalent induction motor and AFPM. AFPM motors are well suited for electrical vehicles (EVs), fans, pumps, control of valves, centrifuges, machine tools, robots among other applications. A typical significant relevance is in low speed applications such as hoists, traction drives and wind generators. This is because their large diameters can accommodate a large number of poles. The large diameter can also be used as a flywheel which can also help minimizing ripple torque.

The increase in power density in RFPM machines is limited by magnetic saturation of the rotor teeth, under utilisation of the rotor core around the shaft/rotor yoke and poor heat evacuation from the rotor to the ambient. AFPM machines have several advantages over RFPM such as: higher power density, a wide range of topologies, larger diameter to length ratio, they have an adjustable airgap which makes them to be relatively easier to construct, they are suitable for high frequency or low speed applications due to their large diameter and their topology is ideal for modular design where modules (stages) can

be adjusted to meet torque or power requirements. In conclusion, AFPM machines have a smaller volume and less active material mass for a given power rating than RFPM machines [24].

The power limitation of an AFPM machine is influenced by its diameter. As the diameter increases the contact surface between the rotor and the shaft becomes smaller, which makes it difficult to design a sound mechanical joint for high power outputs. One way to circumvent this is to adopt multi-stage/multidisc topologies. The advantages of axial flux topology may be lost as the ratio of the length to diameter or as the power increases. The limiting factor in a single-stage machine is that the radius should be less than twice the length of the machine [24].

1.2.6 Cogging Torque

Cogging torque exists in PM machines with an iron-cored-slotted stator. It makes the rotor to 'stick' when it is rotated relative to the stator. This is mainly due to the change in reluctance as a result of slotting. It is independent of current excitation and proportional to the square of the flux-density. Ripple torque is mainly due to EMF and current harmonics and is usually higher than cogging torque [27]. The sum of the ripple and cogging torque gives the pulsating torque component which is superimposed on the developed torque of the machine. Ripple torque is usually filtered out by the system inertia at high speeds but may become significant at low speeds. This is not tolerable for low noise and smooth torque applications [25], [28]. Although ripple torque might be higher than cogging torque, it is important to reduce the latter since it affects the self starting ability of a motor or a generator; particularly at light loads and low wind speeds. For a generator, it implies that the amount of energy captured is reduced for a given installed capacity. Pulsating torque also produces noise and mechanical vibrations which accelerates the wear of the machine.

In [29], cogging torque is mitigated by alternating the pole-arc. This is achieved by designing the consequent magnets in each rotor with two different magnet pole-arc ratios. This is repeated in the second rotor but in the reverse direction. This method is simple and cost effective with minimal effects on the machine performance. This is due to the simplistic design of the pole-shape in comparison to the skewed or circular magnets hence relatively easier to manufacture and often costs less. The method only needs two sets of magnets with different pole angles and the effect on the airgap flux density is relatively small. According to [28] and [29], the peak cogging torque was 51% of the rated torque for a pole-arc ratio of 0.778 and 19% for 0.667. By employing the alternating pole-arc method, it was reduced to 8.7% [29]. In [30], cogging torque is reduced by 99.2% by employing teeth pairing and optimizing the pole-arc ratio. Teeth pairing alone reduces it by about 67%. To use

this method, the tooth-tips must be sufficiently long, thus it is applied to machines with a low slot number and wide tooth-tips.

It is important to point out that minimizing cogging torque does not necessarily minimize torque ripple [27], [31]. It is therefore important to consider methods of minimizing torque ripple. Reference [25] considers ripple torque minimization by optimizing the pole-arc ratio and skewing of the rotor poles. Three PM machine topologies were considered with slotted (S) and non-slotted (NS) stators giving a total of six machines. The topologies are a Radial Surface Mounted PM Motor (RFSM), an Axial-Flux External/Twin/Double/Dual Rotor Internal stator PM motor (TORUS) and the Axial-Flux Internal Rotor External double stator PM motor (KAMAN/AFIR). It was concluded that non-slotted topologies have negligible cogging torque and it was highest in RFSM-S. TORUS-NS machines have the lowest ripple torque at a pole-arc ratio of 0.81 at a skew angle of 32.4°. Ripple torque is also less in AFPM than in cylindrical machines [25]. Ripple torque can also be minimized by designing the windings to have a more sinusoidal MMF. The MMF harmonics can be further reduced by properly wrapping the airgap windings for the non-slotted topologies. In [32], a coreless twin rotor internal stator AFPM was analysed and a pole-arc ratio of 0.8 was seen to have the least ripple torque. It was also noted that ripple torque cannot be minimised by circumferentially changing the relative position of the two rotors or changing the axial length of the airgap or changing the radial thickness of the magnet. In [27] the effect of slot-openings on ripple torque was investigated. Although open slots have more harmonics, they have a relatively less ripple torque than semi-closed slots. A pole angle of 120 electrical degrees eliminates the third harmonic in the air gap flux density. This further minimises ripple torque for a machine with q = 0.5 and semi-closed slots. For minimum torque ripple q should be approximately a third, i.e. q = slots/pole/phase ≈ 1/3 [27].

1.3 *Research Questions*

In the process of determining how electrolyser requirements affect the generator design, the following questions were formulated:

1. Which type of electrolyser is suitable for SAPS applications?
2. What are the possible applications for small-scale hydrogen utilization in rural areas?
3. How do the electrolyser requirements affect the ratings of a wind generator?
4. How does the performance of a parallel-teeth stator topology compare with the conventional trapezoidal-teeth topology?

5. Which are the most effective techniques of minimizing cogging torque in an axial-flux machine with parallel-teeth stator structure, and how is the performance of the machine affected?
6. How does the performance of the generator affect the electrolyser performance?

1.4 *Objectives*

The main objectives of this research are to find out how electrolyser requirements affect the design of the generator, and how the parallel-teeth stator topology affects the machine performance in comparison with the trapezoidal-teeth topology. The specific objectives of this study include:

1. To use the intermittency of a renewable source to determine a suitable electrolyser for a rural application.
2. To size and characterize an electrolyser for small-scale applications and link its performance requirements with the generator design process.
3. To compare the effect of a parallel-teeth stator topology on machine performance to a machine with trapezoidal slots.
4. To analyse the effect of cogging torque minimization techniques on the performance of the machine with parallel-teeth.
5. Relate the experimental machine performance to electrolyser performance parameters.

1.5 *Scope and Limitations*

Hydrogen technology can be regarded as an emerging technology, which is still at its introductory phase. For this reason, issues relating to cost of H_2 technology will not be considered. Furthermore, the exorbitant cost associated with a commercial electrolyser prevented the full implementation of the laboratory wind-electrolysis system. Therefore, most of the analysis done on the electrolyser section will be analytical. An interface is also assumed and will not be prototyped. Thermal analysis will not be considered. The main work will involve the design of the wind generator to meet the electrolyser requirements and analyze the effect of cogging torque on machine performance.

1.6 *Research Significance*

The significance of this research to PM machine design and RE systems includes:

1. An investigation into the possible small-scale use of hydrogen in rural areas by incorporating biogas technology with hydrogen technology.
2. Formulation of an analytical methodology for sizing and characterizing an electrolyser for RE applications.
3. Presentation of a methodology for simulating an AFPM machine as equivalent RFPM machine using open source 2D-FEA software.
4. Development of a twin-rotor-inner-stator generator which eliminates some problems associated with manufacturing of slotted steel stators. The experimental performance is comparable to the analytical and/FEA results. In addition this topology meets machine requirements and inherently reduces cogging torque.
5. Analyses of practical cogging torque minimization techniques for this type of stator are presented and their effect on machine performance is considered. Alternating pole-arcs and skewed poles PM rotor poles were fabricated. They were effective in reducing cogging torque with minimal reduction in machine performance.

1.7 *Thesis Organization*

An overview of hydrogen related technologies such as fuel cells, electrolysers and hydrogen storage is presented in Chapter 2. This leads to the selection of a PEM electrolyser for stand-alone applications. In Chapter 3, the possible small-scale use of hydrogen in rural Africa is discussed. This is done using both thermal and electrical rural loads which results in the sizing and characterization of an electrolyser. Analytical modelling and sizing equations for an axial-flux PMSG are presented in Chapter 4. In Chapter 5, machine design and analysis is discussed. In addition, different methods of minimizing cogging torque and their effect on machine performance are reviewed. This chapter also presents a way of simulating an AFPM machine as an equivalent RFPM machine. The performance of a machine with parallel-teeth topology is also compared to one with trapezoidal-teeth. In Chapter 6, the experimental performance of machines with alternating pole-arcs and skewed poles is compared with one with a pole-arc ratio of 0.80. The experimental results are also compared with analytical and/or FEA results. The effect of these machines on electrolyser performance is also discussed. Finally, in Chapter 7, conclusions and recommendations are presented.

2 Overview of Hydrogen Technology

In this chapter hydrogen technology which includes fuel cells, electrolysers, hydrogen storage and hydrogen infrastructure, is discussed. The working principle and modelling of fuel cells and electrolysers are reviewed. Some of the hydrogen storage methods are also reviewed. The electrolyser performance parameters such as the hydrogen production rate and efficiency are shown to be dependent on current and stack voltage respectively. An analytical PEM electrolyser model which will be used in Chapter Three for electrolyser characterization is derived. The advantages of a PEM electrolyser for stand-alone applications over alkaline electrolysers are also noted. This leads to its selection for this type of application.

2.1 *Fuel Cells (FCs)*

A fuel cell (FC) is a device that converts chemical energy to electrical energy with the release of water and heat as by-products (see eqn (2.1)). The inputs are hydrogen or hydrogen rich fuel and oxygen in presence of a catalyst. William Robert Grove invented the first FC in 1839. He used sulphuric acid as an electrolyte and porous platinum as electrodes. Since then, further research in this field has enabled the use of FCs in space programs since 1960s (Apollo and Space Shuttles) [2]. In recent years, their use in power generation has also been demonstrated. For instance, a 220kW solid oxide fuel cell (SOFC)-micro turbine hybrid system was initiated at the University of California, Irvine. This system has an efficiency of 52-53% [2]. In addition, automotive companies such as Daimler-Chrysler, Ford, General Motors, Toyota, Honda, and Nissan among other companies are funding fuel cell vehicle (FCV) programs. Some of these companies have even produced prototype vehicles [2], [33]. An example is the Clean Urban Transport for Europe (CUTE) program. This program is continuously designing, analyzing, testing, optimizing and developing FCs, hydrogen internal combustion engines (ICEs) and hydrogen refueling infrastructure [34]. Fuel cells are becoming popular due to the following reasons:

1. They are reliable and quiet in operation due to the absence of moving parts
2. Fuel cells generate less noise allowing in-house installation
3. The waste heat can be used for heating, increasing the efficiency of the plant
4. Their application in stand-alone power generation near load points, reduces transmission and distribution costs

5. Hydrogen, which is used as a fuel, is safe since it burns with low radiation heat and escapes rapidly due to its low density which causes it to spread easily; compared to fuels like gasoline and diesel
6. Fuel cells are also lighter, last longer and can be easily refuelled
7. Another important aspect is that they are efficient even at low loads, which is promising for power generation.

2.1.1 Operation of a Fuel Cell

The cell has two electrodes, i.e. the positively charged electrode (anode) and the negatively charged electrode (cathode) in the presence of an electrolyte. Hydrogen ionizes into H^+ ions (protons) and electrons by the aid of a catalyst. Electrons flow through the outer circuit setting up a current, while protons migrate to the cathode via the electrolyte. At the cathode, the protons recombine with electrons and react with oxygen to produce water and heat as shown in Fig 2.1.

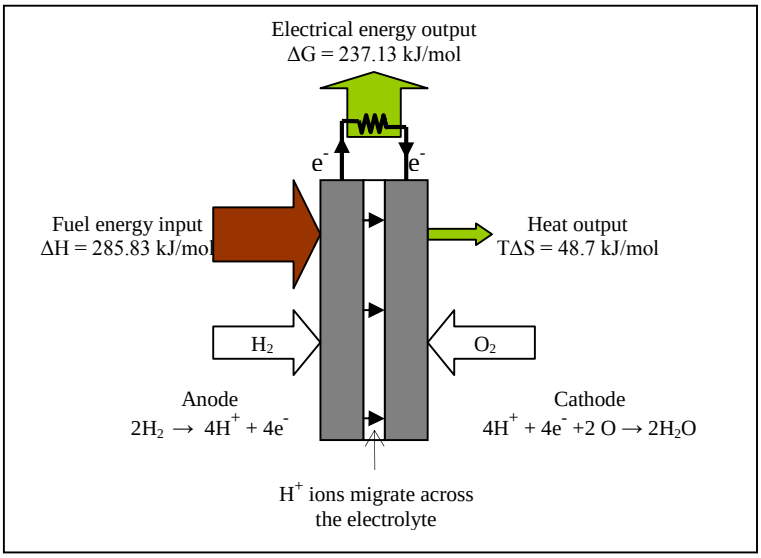

Fig 2.1 Fuel cell concept

In polymers and acidic electrolytes, protons move to the cathode via the electrolyte. However in alkaline and basic electrolytes, negative ions migrate to the anode through the electrolyte. The fuel cell reaction is governed by eqn (2.1).

$$2H_{2(g)} + O_{2(g)} \rightarrow 2H_2O_{(l)} + 4e^- + heat \qquad (2.1)$$

The efficiency of a FC depends on thermodynamics, electrode kinetics, mass transfer of reactants, materials and components constituting a fuel cell. The operating voltage of a basic FC is about 0.6-

0.7V at the rated current. This range is less than the theoretical value of a single cell, which is 1.229V. To meet load requirements, single cells are assembled into a stack as shown in Fig 2.2.

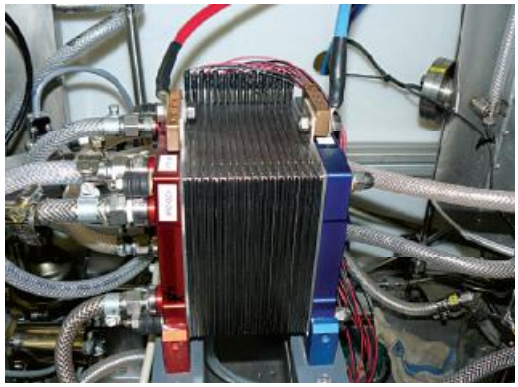

Fig 2.2 PEMFC stack (16 cells, 500W, 50A, and around 11V) [35]

At 25°C (298K) and 1 atms, energy is generated by combining a mole of hydrogen and half a mole of oxygen. This reaction is spontaneous, unlike in electrolysis where energy is required for the reaction.

The reaction can be described thermodynamically by considering enthalpy, entropy and Gibbs free energy equation. Enthalpy, H is the summation of internal energy, U and $P\Delta V$ which is the product of pressure P and change in volume ΔV, i.e. $H = U + P\Delta V$. U is the energy released by the production of water, while $P\Delta V$ is the energy due to a decrease in the volume of the gases. This is because the water molecules formed are less than the total sum of hydrogen and oxygen molecules. In other words, two molecules of water are formed when two molecules of hydrogen react with an oxygen molecule. The excess energy $T\Delta S$ is dissipated to the environment as heat (where $\Delta S = Q/T$ is entropy and Q is the heat dissipated to the ambient at a temperature T). The theoretical energy converted to electrical energy is given by the Gibbs free energy equation in eqn (2.2) and as shown in Fig 2.1. By harnessing $T\Delta S$, the overall efficiency of the FC can be improved by combining heat and power generation (CHP).

$$\Delta G = \Delta H - T\Delta S = -285.83kJ + 48.7kJ = -237.1kJ \qquad (2.2)$$

where ΔG and ΔH are changes in Gibbs free energy and enthalpy respectively. Thermodynamic values are as given in Table 2.1.

Table 2.1 Thermodynamic quantities for H_2, O_2 and H_2O

Quantity	**H_2**	**$0.5O_2$**	**H_2O**	**Change**
Enthalpy (H)	0	0	-285.83 kJ	ΔH = -285.83 kJ
Entropy (ΔS)	130.68 J/K	0.5×(205.14) J/K	69.91 J/K	TΔS = -48.7 kJ

Table 2.2 and Fig 2.3 summarises the characteristics of different types of FCs, i.e. the type of electrolyte, operating temperature range and possible application. References [2], [33], [36] can be reviewed for more information on FCs.

Table 2.2 A summary of some common fuel cells and their applications [2]

Fuel Cell Type	Electrolyte	Temperature °C	Application
Alkaline (AFC)	Alkaline	50-200	Space travel, transportation
Direct Methanol (DMFC)	Polymer	80-200	Transport, mobile equipment
Proton-exchange-membrane (PEM)	Polymer	50-80	Space travel, transportation, small CHP, mobile equipment
Phosphoric acid (PAFC)	Phosphoric acid	190-210	CHP, power plants
Molten Carbonate (MCFC)	Molten carbonate	600-650	CHP, power plants
Solid Oxide (SOFC)	Solid oxide	600-1000	CHP, power plants

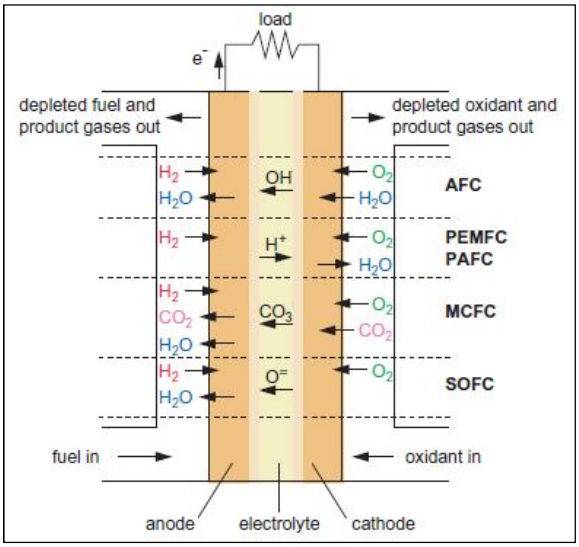

Fig 2.3 Operation of different types of FCs [36]

2.1.2 Fuel Cell Models

There are two kinds of FC models, i.e. theoretical or mechanistic models and empirical and/or semi-empirical models [37], [38]. In the mechanistic model, the cell voltage, U_{FC} is given as [38]

$$U_{FC} = U_{OCV} - U_a - U_c - U_{ohm} \tag{2.3}$$

where U_{OCV} is the open circuit voltage, U_a and U_c are the activation and concentration voltage drops and U_{ohm} is resistive losses. Diffusion voltage when operating at higher current densities should also be considered. These overvoltages are dependent on temperature and on the hydrogen and oxygen

partial pressures. According to [37], this model requires prior knowledge of nine parameters, which are difficult to evaluate. It can be improved by using empirical and semi-empirical methods to evaluate some parameters, such as the ohmic voltage and the equilibrium water content of the membrane as done in [38].

The second method uses experimental data which is curve-fitted to an empirical equation to model a FC. The terms of this equation comes from the Nernst, Tafel and Ohm laws. This type of model is not universal but simpler than the theoretical one. This is evident by comparing the analytical and semi-empirical equations presented in [38] and the empirical equations in [37]. An empirical model that can predict the current-voltage relationship for a typical PEMFC can be given as [37], [38].

$$U_{FC}(i) = U_{OCV} - b\ln(i) - Ri - m\exp(ni) - b\ln\left(\frac{P}{p_{O2}}\right) \tag{2.4}$$

where i is the current density (A/cm^2), b is a Tafel parameter for oxygen reduction (V), R is resistance (Ωcm^2) , P/p_{O2} is the pressure ratio, m and n are diffusion parameters (V and A^{-1} respectively). Each term is dominant in a given region of the voltage-current density relationship shown in Fig 2.4. The second term influences region 1 where the voltage decreases sharply due to oxygen electrochemical activation reactions. Resistive losses (the third term) are dominant in region 2 while in region 3, diffusion losses expressed by the fourth and fifth terms dominate [37], [38].

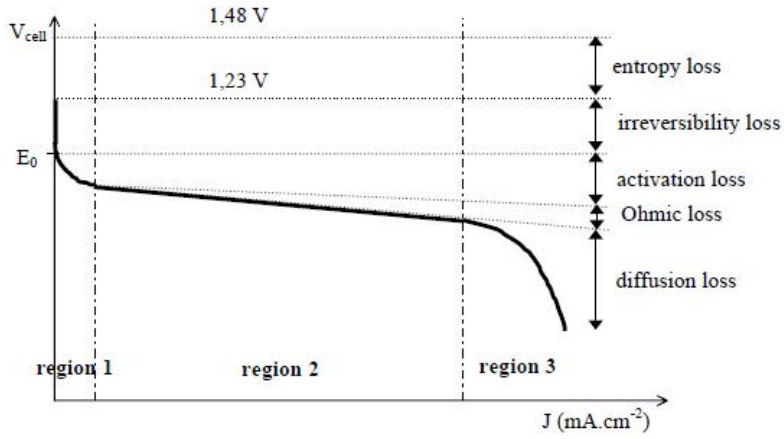

Fig 2.4 FC characteristic; $V_{cell} = U_{FC}$; $E_o = U_{OCV}$; $J = i$ [37]

In [37], the number of unknowns is reduced to four and the developed model can predict the cell voltage at any current density. It is given as

$$U_{FC}(i) = U_{OCV} + \frac{b}{\ln(i/i_d) - 2} + \left(\frac{b}{4i_d} - \Delta\right) \times i \qquad (2.5)$$

where i_d is the current density when $\frac{d^2 U_{FC}}{di^2}(i_d) = 0$ and Δ is obtained from $\frac{dU_{FC}}{di}(i_d) = -\Delta$ at the point of inflexion (i_d, $U_{FC}(i_d)$).

2.2 *Hydrogen Storage*

Hydrogen has a high energy density by weight. For this reason, it is widely used in space travel and well suited for aeronautical applications. However, its energy density by volume is rather low, posing a greater challenge than gasoline with respect to storage. According to [8], the main challenges in hydrogen storage are its low density and boiling point even at high pressure. These challenges have to be surmounted for commercialization of fuel cell vehicles (FCVs). According to US DoE, FCV storage must meet an energy density of 6.5 %wt H_2 and 62 kg H_2/m^3 for a driving distance of 560km [2]. Hydrogen can be stored in compressed form, as a liquid or in metal hydrides, among other methods.

2.2.1 Compressed Hydrogen

Hydrogen is compressed and stored in tanks or cylinders made of steel or aluminium encased with fibre glass or plastic encased with fibre glass. This type of storage is applicable for stationary systems where space is available. To improve on efficiency, pressurized electrolysers are used which reduce or completely eliminate the need for compression.

2.2.2 Liquid Hydrogen (LH_2)

Hydrogen is stored as a liquid at -253°C (20K) in highly insulated tanks. This is well suited for long distance transportation and aerospace applications. Compression energy required is about 30-40% of the fuel energy. This increases inefficiency and it is one of the challenges in FCV storage. Linde, a German company has developed a tank for LH_2 which uses the low temperature of LH_2 to cool the insulator [2].

2.2.3 Metal Hydride

A hydride is a compound consisting of hydrogen and other elements. Some metals and metallic alloys have the ability to absorb hydrogen at moderate pressures and temperatures. A metal hydride assembly comprises of a heat system and a granular matrix which holds the hydrogen. The heat system cools the hydride storage during 'charging' and raises its temperature during 'discharge'. Excess heat from the FC or ICE can be used in the discharge cycle. This storage method is considered to be safe. In the event of an accident, the system will cool down, stopping the flow of hydrogen due to the loss of pressure.

Other methods of storage include: storing hydrogen in carbon nano tubes, in combined form (fossil fuels) especially methanol, in large underground hydrogen storages and also in pipelines by regulating the pressure in the pipes during peak times. Table 2.3 gives the various ways of storing hydrogen with their corresponding densities. The densities relate to the mass of stored hydrogen to that of the storage or holding material [36].

Table 2.3 Hydrogen storage methods [36]

Type	**kgH_2/kg**	**kgH_2/m^3**
Large volume storage (10^2-$10^4 m^3$)		
Underground	-	5-10
Pressurized gas storage (above ground)	0.01-0.014	2-16
Metal hydride	0.013-0.015	50-55
Liquid hydrogen	~1	65-69
Stationary small storage (<100m^3)		
Pressurized gas cylinder	0.012	~15
Metal hydride	0.012-0.014	50-53
Liquid hydrogen tank	0.15-0.50	~ 65
Vehicle tanks (0.1-0.5m^3)		
Pressurized gas cylinder	0.05	15
Metal hydride	0.02	55
Liquid hydrogen tank	0.09-0.13	50-60

Hydrogen transportation and distribution may benefit from utilizing existing natural gas infrastructure and technology. This would require some modifications on the pipelines and pumps due to its lightness which would present sealing problems. The pipes would have to be larger and more energy is needed to compress it. Fortunately, due to lower pressure loss, the recompression stations would be spaced twice apart. Studies have shown that the cost of massive transmission of hydrogen is around 1.5-1.8 times that of natural gas. In addition, it is more economical to pump hydrogen over greater distances (over 1000km) compared to transmission of electricity [36].

2.3 *Electrolysis of Water*

Electrolysis was the chief method of producing hydrogen in the 1920s and 1930s. As the demand for hydrogen grew, steam reforming of fossil fuels (especially methane) gradually took over because it was economical [1]. Today, the stakes against fossil fuels are high - diminishing fuel stocks, fluctuating fuel prices, high demand for fossil fuels and adverse environmental effects. This is ushering a new era of using electrolysis as a viable 'clean' option for hydrogen production. An electrolyser provides the necessary conditions and surfaces for the electrolytic process.

2.3.1 Operation of an Electrolyser

Electrolysis is the process of splitting water molecules into hydrogen and oxygen molecules. This requires energy which is usually thermal or electrical or a combination of the two. The electrolyser holds the electrolyte in the presence of electrodes. The process generates 2 moles of hydrogen at the cathode and 1 mole of oxygen at the anode. According to [4], electrolysis is the only practical way of producing clean and sustainable hydrogen due to the abundance of water supply.

For acidic electrolytes, the half reactions at the cathode and anode are

$$\text{Cathode (reduction): } 2H^{+}_{(aq)} + 2e^{-} \rightarrow H_{2(g)} \tag{2.6}$$

$$\text{Anode (oxidation): } 2H_2O_{(l)} \rightarrow O_{2(g)} + 4H^{+}_{(aq)} + 4e^{-} \tag{2.7}$$

The half reactions for basic or alkaline electrolytes are

$$\text{Cathode (reduction): } 2H_2O_{(l)} + 2e^{-} \rightarrow H_{2(g)} + 2OH^{-}_{(aq)} \tag{2.8}$$

$$\text{Anode (oxidation): } 4OH^{-}_{(aq)} \rightarrow O_{2(g)} + 2H_2O_{(l)} + 4e^{-} \tag{2.9}$$

Combining the half reactions for either acidic or basic electrolytes yields

$$2H_2O_{(l)} + energy \rightarrow 2H_{2(g)} + O_{2(g)} \tag{2.10}$$

The choice of an electrolyte depends on the electrode potential. This is the potential difference between individual potentials of the two electrodes with respect to the electrolyte. Positive ions

(cations) should have a lower potential than hydrogen ions (H^+) while negative ions (anions) should have a higher potential than hydroxide ions (OH^-). Sodium (Na^+) and potassium (K^+) are often used as cations. If an acid is used as an electrolyte, the commonly used anions are sulphate (SO_4^{2-}) and carbonate (CO_3^{2-}). Examples of electrolytes are sulphuric acid (H_2SO_4), potassium hydroxide (KOH) and sodium hydroxide (NaOH). The selection of electrodes on the basis of electrode potential prevents the corrosion of electrodes by ionization. Nafion® is a solid polymer electrolyte which effectively splits water molecules in the presence of a catalyst. Brine ($NaCl_{(aq)}$) is rarely used as an electrolyte due to the liberation of chlorine gas (Cl_2). It also produces less hydrogen compared to electrolysis. This is evidenced by comparing eqns (2.10) and (2.11).

$$2NaCl_{(aq)} + 2H_2O_{(l)} + energy \rightarrow Cl_{2(g)} + H_{2(g)} + 2NaOH_{(aq)} \qquad (2.11)$$

In alkaline electrolysers (KOH type), the anode can be nickel (Ni), cobalt (Co) and iron (Fe) based while the cathode can be nickel-based with a platinum-activated catalyst (Ni, C-Pt) with nickel oxide (NiO) diaphragms [17].

The electrolytic process provides the necessary energy needed to dissociate water and expand the freed gases as seen in Fig 2.5. An energy input requires the thermodynamic quantities given in Table 2.1 to be positive. In this case, internal energy, U dissociates water molecules, $P\Delta V$ expand the gases and $\Delta S = Q/T$ is derived from the environment to aid in the electrolysis process. The theoretical energy needed for the process is given by the Gibbs free energy expression as

$$\Delta G = \Delta H - T\Delta S = 285.83kJ - 48.7kJ = 237.1kJ \qquad (2.12)$$

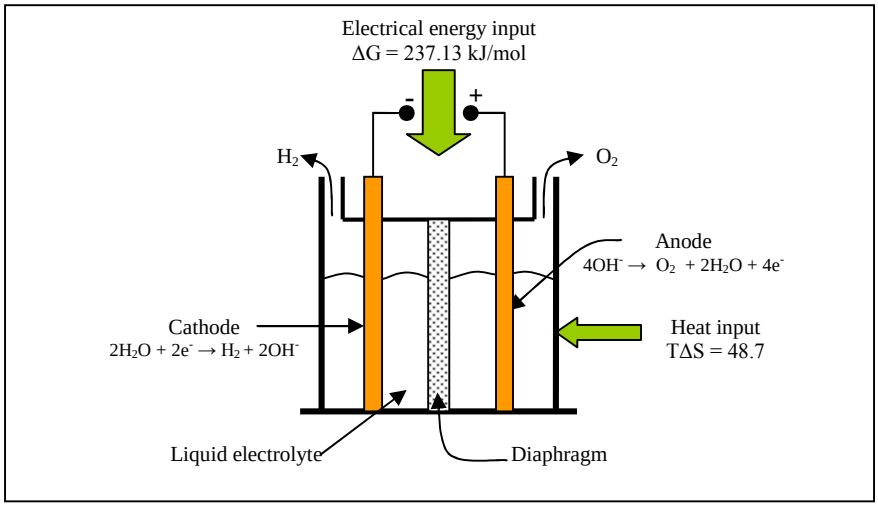

Fig 2.5 An alkaline electrolyser cell

Operating the electrolyser at high temperature reduces the electrical energy demand. By comparing eqns (2.2) and (2.12), it can be inferred that electrolysis is the reverse process of a fuel cell.

Ideally, 39kWh (HHV) of electricity and 8.9 litres of water are required to produce 1kg of hydrogen at 25°C and 1 atms. Practically this value is higher in the range of 53.4 - 70.1kWh/kg at an efficiency of 56-73% [1]. [4] reports that a litre of water produces 1.24Nm^3 H_2 theoretically, but the actual water demand is 25% higher. The author also gives a range of 4.5-6.0kWh/Nm^3 at an efficiency of 65-80% for commercial electrolysers. [33] gives a consumption of 40-45kWh/kg at an efficiency of 70-75%. The acronyms HHV and LHV refer to the higher heating value and lower heating value of a fuel. Efficiencies reported by different authors fall in the range of 40-88% [1], [4], [14], [33]. The main goal is to achieve over 85% efficiency for commercial electrolysers [33].

Change in Gibbs free energy is related to the reversible voltage, U_{rev} by

$$U_{rev} = \frac{\Delta G}{zF} = \frac{237.1 \times 1000J}{2e^- \times 96{,}485C/mol} = 1.229V \tag{2.13}$$

while change in enthalpy is related to the thermoneutral voltage, U_{tn} by the expression

$$U_{tn} = \frac{\Delta H}{zF} = \frac{285.83 \times 1000J}{2e^- \times 96{,}485C/mol} = 1.481V \tag{2.14}$$

where:

z = number of electrons transferred per mole of H_2O ($z = 2e^-$)

U = voltage difference across the electrodes of a single cell in volts, V

F = Faraday's constant, F = 96,485 C/mol or As/mol

In other words, U_{rev} and U_{tn} are the electrical notations for ΔG and ΔH energies. At standard conditions U_{rev} = 1.229V and U_{tn} = 1.482V, which agrees with the values obtained in eqns (2.13) and (2.14).

The rate of producing hydrogen in kg/h is expressed as [14]

$$\mathrm{H_2\ production\,(kg/h)} = \frac{2.106g/mol\ \text{of}\ \mathrm{H_2} \times 3600s}{1000} \times \frac{\eta_c I_{ely}}{zF} = 7.5816\frac{\eta_c I_{ely}}{zF} \tag{2.15}$$

where I_{ely} is the stack current in Amperes (1A is 1 Coulomb/sec) and η_c is the number of cells in series. By manipulating eqn (2.15) the rate in m^3/sec is $1.30\times10^{-7} I_{ely}$ (m^3/sec) for η_c = 1 at 20°C (293K) and 1 atms where the density is 0.08376kg/m^3. Therefore, the rate of producing hydrogen is proportional to the input current. For 1A, the amount of hydrogen liberated is $1.30\times10^{-7}\,\mathrm{m}^3 = 1.09\times10^{-8}\,\mathrm{kg}$/sec.

The efficiency of hydrogen production is commonly referenced to the LHV of hydrogen as [14]

$$efficiency = \frac{LHV\ of\ H_2 (33.3 kWh/kgH_2)}{specific\ energy\ use\ (kWh/kgH_2)} \tag{2.16}$$

Specific energy use is the ratio of the input power to the electrolyser over the actual amount of hydrogen generated. It is given as

$$specific\ \ energy\ use (kWh/kgH_2) = \frac{U_{ely} I_{ely} (kW)}{H_2\ \ production (kg/h)} \tag{2.17}$$

Combining eqns (2.15), (2.16) and (2.17) gives efficiency as

$$efficiency = 7.5816 \times \frac{1000}{zFU_{ely}} \eta_c \times LHV\ of\ H_2 (33.3 kWh/kgH_2) \tag{2.18}$$

The efficiency is therefore inversely proportional to the electrolyser stack voltage, U_{ely}. To operate at higher efficiencies, the cell voltage is usually held close to the thermal neutral voltage, U_{tn} = 1.48V. Practically the actual operating voltage is in the range of 1.48-2V due to overpotentials. Higher voltages lead to dissipation of heat (this can be applied to self-starting/self-heating electrolysers), while lower voltages result in permeation and impurity of the gases. Impurity is due to low production rates of gases and increases at low voltages [14].

2.4 *Types of Electrolysers*

Electrolysers can be classified according to the type of electrolyte they use. The common ones are the alkaline electrolysers, polymer electrolyte membrane or proton exchange membrane (PEM)

electrolysers or solid polymer electrolysers (SPE) and solid oxide electrolysers or steam electrolysers [1], [2], [17], [39].

2.4.1 Alkaline Electrolysers

Majority of the alkaline electrolysers use a liquid electrolyte, for instance, KOH at 20-40% concentration. These electrolysers operate at relatively low current densities of less than 0.4 A/cm^2. Gas purities are typically 99.8% and 99.2% for H_2 and O_2 respectively. Their operating temperature and pressure are within 70-100°C and 1-30 bars respectively. They have been used by Norsk Hydro Electrolysers (NHE), Norway since 1928. Some of the NHE's electrolysers have an efficiency of over 80% [17], [39].

Alkaline electrolysers are less expensive than PEM electrolysers due to their reduced catalytic loading. Corrosion of electrodes is a challenge in this type of electrolysers. It can be alleviated by having an idling current, draining the electrolyte though the start-up time will be long or operating at low power levels of 10-40% when the electrolyser is not in use [5], [17], [39].

There are two types of designs that have been widely used in alkaline electrolysers. These are: the unipolar or monopolar (tank) design and the bipolar or filter-press design [1], [17]. Fig 2.6(a) depicts a unipolar design where electrodes are alternately suspended in a tank. The cells are connected in parallel at a potential of 1.9-2.5 V. They are simple to manufacture and repair, however they operate at lower current densities and temperatures.

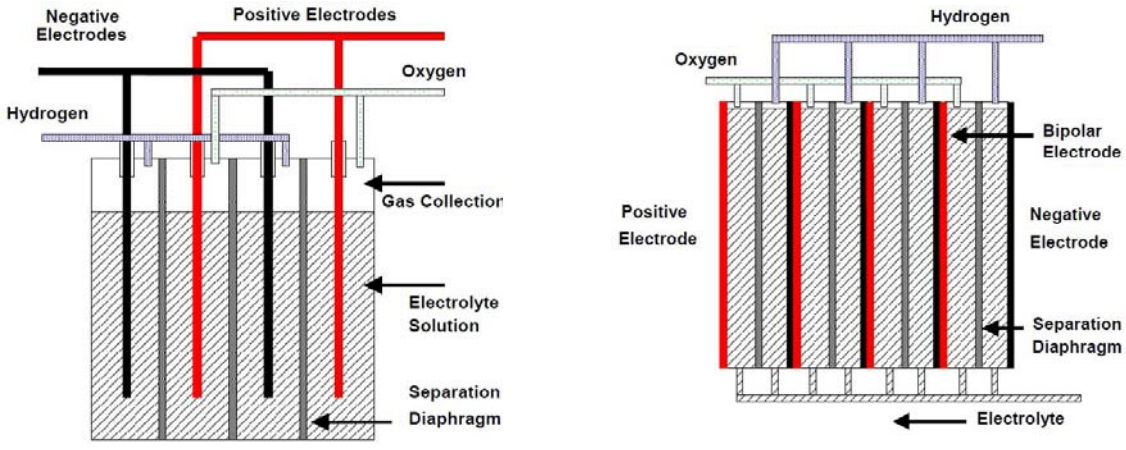

(a) Unipolar design **(b) bipolar design**

Fig 2.6 Alkaline electrolyser designs [1]

The bipolar design has negative and positive electrodes bound together as shown in Fig 2.6(b). The cells are connected in series resulting in higher stack voltages. Bipolar cells have a reduced stack size due to their relatively thin cells and they operate at higher current densities. In addition, they can produce pressurized gas. The limitation of this design is that it cannot be repaired without servicing the entire stack. Bipolar cells are also predisposed to parasitic currents that cause corrosion problems. They are also expensive [1], [17]. Asbestos has been widely used as a diaphragm material. New materials such as Ryton® a polymer, composites such as polysulfones and oxide-ceramics among others are replacing it [14].

New improvements on the design of alkaline electrolysers have led to advanced alkaline electrolysers. They have zero-gap cells, low resistance diaphragms, higher process temperatures (up to 160°C) and new catalysts which reduce anodic and cathodic overpotentials. This design has been adopted by many manufacturers [17].

2.4.2 PEM/SPE Electrolysers

An SPE or PEM electrolyser consists of a polymer electrolyte sandwiched between porous electrodes. The polymer allows the flow of protons and inhibits the flow of electrons as shown in Fig 2.7. The membrane should be hydrated at all times. The membrane separates the anode and the cathode as well as oxygen and hydrogen gases. PEM electrolysers have higher current densities than alkaline electrolysers (1-2A/cm^2) with an efficiency range of 50-90%, and they employ bipolar design. Their response time is short, therefore they can respond to transients. This makes them well suited for intermittent RE applications. They can also operate at higher pressures reducing the need for auxiliary compression. They are also well suited for small plants [2], [3]. A typical PEM electrolyser is made of a polymer such as Nafion®, while platinum is commonly used for the cathode. Pt-IrO_2 alloy catalyst is preferred for the anode [40].

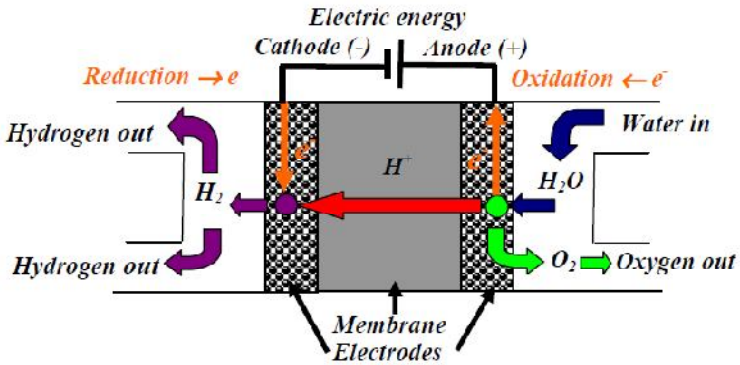

Fig 2.7 A PEM electrolyser [41]

2.4.3 Solid Oxide Electrolysers or Steam Electrolysers

The solid oxide electrolysers employ a ceramic ion (O^{2-}) conducting electrolyte (zirconia/ceria) at 800-1000°C. They have a high efficiency factor, i.e. they use less electricity by deriving energy from the heat source. Their main disadvantage is thermal and sealing related problems at elevated temperatures making the production of prototypes difficult [39].

The performance of electrolysers is influenced by factors such as operating voltage, temperature and pressure. An increase in temperature reduces the electrical energy needed for the process. Waste heat from the FC or ICE can be used to raise the temperature of the feed water increasing the overall system efficiency. Operating at high pressure reduces the need for an auxiliary compressor improving efficiency and reducing cost.

2.5 *Electrolyser modelling equations*

Similar to FC modelling, empirical and analytical current-voltage relationships are used to model an electrolyser cell. All these models try to express the electrolyser voltage as a function of overvoltages.

2.5.1 Empirical Models

An empirical model that considers electrode kinetics at a given operating temperature was proposed by [8]. The input parameters to the model are: the electrode area, the reversible voltage, the stack current, the resistance of the electrolyte and the coefficients of the overvoltages. This model was improved by [17], by taking into account the dependency of overvoltage coefficients on temperature. The operating voltage was then be obtained by linear interpolation between the two curves at different temperatures as shown in Fig 2.8.

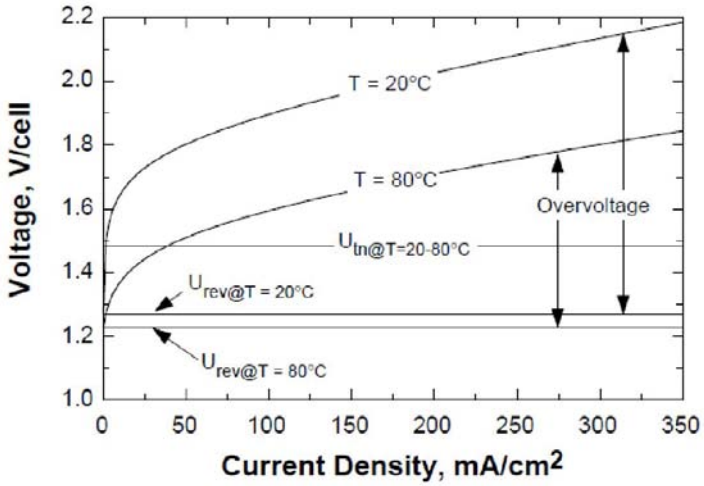

Fig 2.8 Typical voltage-current curves for an electrolyser cell at high and low temperatures [17]

A PEM electrolyser experimental curve was fitted to an exponential current-voltage equation as shown in Fig 2.9. By switching the current and voltage axes, the curve resembles those shown in Fig 2.8. Therefore alkaline electrolyser modelling equations can be used to analyze PEM electrolysers.

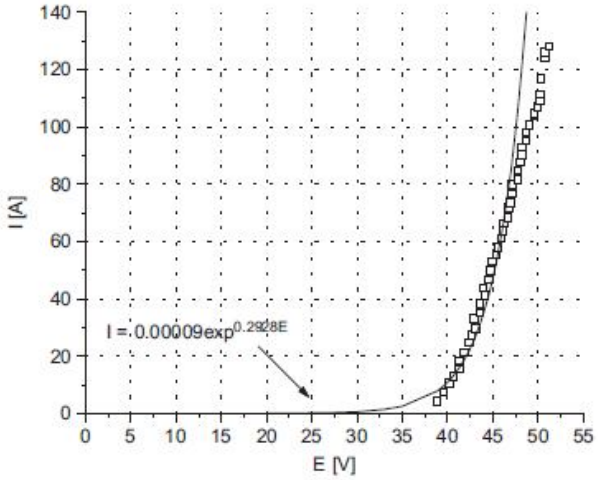

Fig 2.9 Experimental (□) and exponential equation (-): I = 0.00009 exp (0.29285E) [42]

2.5.2 Analytical Models

An analytical model for an alkaline electrolyser is given by [12]. The overvoltages are added to the open circuit voltage, i.e. $U_{ely} = U_{OCV} + U_a + U_c + U_{ohm}$. These overvoltages are similar to those of a PEM electrolyser which will be analysed later. A minor difference is in the ohmic drop of the liquid electrolyte whose resistance is given as $R_{ely} = \frac{d_e}{\sigma_k \times A_c}$. d_e is the distance between the electrodes, A_c

is the cross-sectional area of the electrolyte and σ_k is the electrical conductivity of the electrolyte. For KOH, it is given as

$$\sigma_k = 2.62 \times C_{KOH} + 0.067 C_{KOH}\left(T_{ely} - 273.15\right) - 4.8 \times C^2{}_{KOH} - 0.088 \times C^2{}_{KOH}\left(T_{ely} - 273.15\right) \quad (2.19)$$

where C_{KOH} is the mass concentration of KOH. Fig 2.10 shows an equivalent electrical circuit for an electrolyser cell. The electrochemical potential U_{ely} of the cell can be derived by combining overpotentials from references [40], [41], [43], [44] as,

$$U_{ely} = U_{OCV} + U_a - U_c + U_{diff} + U_{ohm} + U_{int} \quad (2.20)$$

These voltage drops are expressed analytically in the succeeding subsections (i) to (iv).

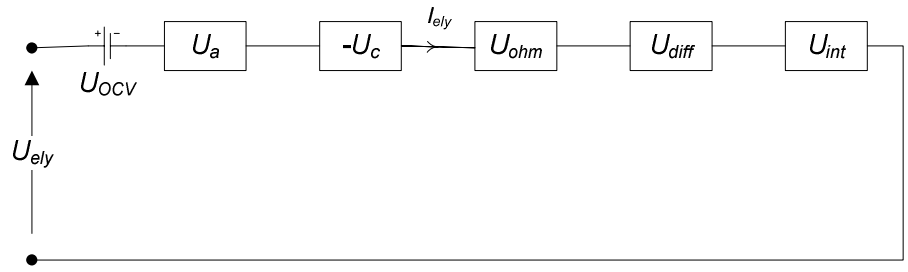

Fig 2.10 Equivalent circuit of an electrolyser cell

i) Open circuit voltage or the reversible voltage, U_{OCV}

The open circuit voltage is as a result of the chemical Redox reaction. It represents the cell potential when the current is nil. It is given by the Nernst equation as

$$U_{OCV} = U_{rev} + \frac{RT}{zF} ln\left(\frac{P_{H2} P_{O2}{}^{1/2}}{a_{H2O}}\right) \quad (2.21)$$

where:

T = electrolyser temperature

R = 8.3144 J/mol K is the universal gas constant

P_{H2} and P_{O2} are partial pressures for H_2 and O_2 respectively

a_{H2O} = 1 for liquid water is the water activity

ii) Anode, U_a and cathode, U_c activation potentials

The activation voltage drops represent the transfer of reactants through the electrodes. For the anode and cathode, they can be expressed as

$$\left.\begin{aligned} U_a &= \frac{RT}{\alpha_A zF} ln\left(\frac{i}{i_{AO}}\right) \\ U_c &= -\frac{RT}{\alpha_C zF} ln\left(\frac{i}{i_{CO}}\right) \end{aligned}\right\} \qquad (2.22)$$

Where i_{AO} and i_{CO} are the anode and cathode exchange current densities in A/cm^2, α_A and α_C are the transfer coefficients for the anode and cathode electrode ($\alpha = \alpha_A = \alpha_C = 0.5$ according to [40] while [41] gives $\alpha = 0.452$). $i = I/A$ is the current density with I being the electrolyser current and A being the membrane-electrode-assembly (MEA) active area. The anode overpotential is usually dominant compared to the cathode overpotential. This can be seen in Fig 2.11. The anode catalyst material also affects U_a. This can be seen by inspecting curves 4 and 5. For simplification purposes, the cathode overpotential can be neglected resulting to

$$U_a = U_{act} = \frac{RT}{\alpha zF} ln\left(\frac{i}{i_{AO}}\right) \qquad (2.23)$$

with U_{act} representing the activation potentials.

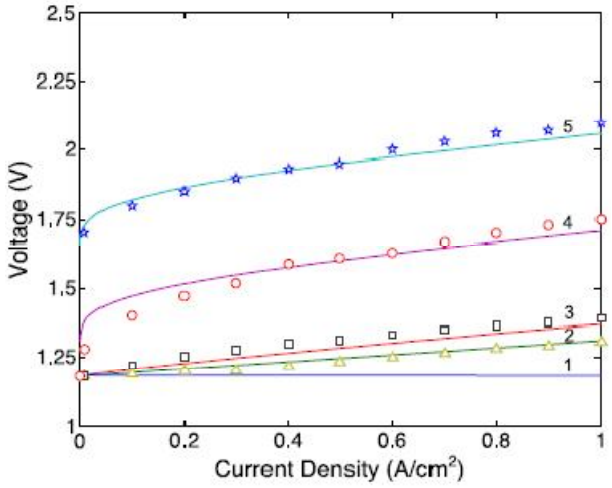

Fig 2.11 Experimental data at 80°C (1:U_{OCV}, 2:U_{ohm}, 3: U_c, 4: U_a on Pt-IrO2, 5: U_a on Pt) [40]

iii) Diffusion voltage drop, U_{diff}

Diffusion close to the electrodes results in variation of partial pressure and chemical reaction rate and is expressed as [41]

$$U_{diff} = \frac{RT}{\beta zF} ln\left(1 + \frac{i}{i_{lim}}\right) \tag{2.24}$$

Where β is a constant coefficient and i_{lim} is the diffusion limit current density. Authors [40] and [44] have negated U_{diff} in their models.

iv) Ohmic voltage drop, U_{ohm} and the interface voltage drop, U_{int}

Ohmic voltage drop is mainly due to the polymer membrane. The ohmic drop is given as

$$U_{ohm} = R_m \times i \tag{2.25}$$

The membrane resistance R_m (Ω) is calculated as $R_m = t_m / \sigma_m$ where t_m (cm) is the membrane thickness and σ_m (S/cm) is the conductivity of the membrane. The conductivity is dependent on temperature and water content, λ_m as given by [41], [43].

$$\sigma_m = (0.00514\lambda_m - 0.00326) exp\left(1268\left(\frac{1}{303} - \frac{1}{T}\right)\right) \tag{2.26}$$

The resistance of the membrane can also be expressed as a function of resistivity ρ_m (Ωcm), $R_m = \rho_m t_m$. Resistivity is given as

$$\rho_m = \frac{181.6\left[1 + 0.03(I/A) + 0.0062(T/303)^2 (I/A)^{2.5}\right]}{\left[\lambda_m - 0.634 - 3(I/A)\exp(4.18((T-303)/T))\right]} \tag{2.27}$$

The membrane water content, λ_m is expressed as

$$\lambda_m = \begin{cases} 0.043 + 17.81a - 39.85a^2 + 36a^3 & ; \text{ for } 0 < a \le 1 \\ 14 + 1.4(a-1) & ; \text{ for } 1 < a \le 3 \end{cases} \tag{2.28}$$

The value of λ_m indicates the relative humidity of the membrane. $\lambda_m = 7$ indicates a dry membrane and $\lambda_m = 14$ indicates good hydration (100%). When $a = 1$, $\lambda_m = 22$ for water immersed membrane [41], [44], [45]. $a = a_{H2O}$ is water activity. The interface overpotential, U_{int} is given by [40] as a product of the interface resistance, R_{int} and current density, i, that is, $U_{int} = R_{int} \times i$.

The electrochemical potential or electrolyser cell voltage can be simplified by negating U_{diff}, U_{int} and U_c, such that eqn (2.20) reduces to $U_{ely} = U_{OCV} + U_a + U_{ohm}$, that is,

$$U_{ely} = U_{rev} + \frac{RT}{zF} ln\left(\frac{P_{H2} P_{O2}^{1/2}}{a_{H2O}} \right) + \frac{RT}{\alpha zF} ln\left(\frac{i}{i_{AO}} \right) + R_m i \tag{2.29}$$

The rate of producing H_2 and O_2 in mol/s is expressed as

$$\left.\begin{aligned} H_2 = 2O_2 &= \frac{I}{2F}\eta_F \\ \eta_F &= \frac{i - i_{loss}}{i} \end{aligned}\right\} \tag{2.30}$$

where η_F is Faraday efficiency and $i_{loss} < 1\%$ i is the internal current and hydrogen loss which could result from permeation of gases [43]. Table 2.4 gives some parameters for a PEM electrolyser operating at 80°C while Table 2.5 gives the thickness of Nafion® membranes for different hydration levels. Using any of the above models the instantaneous current or voltage can be obtained for certain operating conditions.

Table 2.4 PEM/SPE electrolyser parameters [40]

Parameter	Value	Units	Comments
$i_{AO,Pt}$	10^{-12}	A/cm^2	Anode exchange current density for Pt
$i_{AO,Pt\text{-}Ir}$	10^{-7}	A/cm^2	Anode exchange current density for Pt-Ir
i_{CO}	1.0×10^{-3} 0.3×10^{-3} Ref [41]	A/cm^2	Cathode exchange current density for Pt
σ_m	0.14	(S/cm)	Conductivity of Nafion® 117 electrolyte

Table 2.5 Thickness of Nafion® membranes [45]

Membrane	Thickness (mm)			
	Nominal	Dry	Wet	MEA
Nafion 117	0.178	0.183 ± 0.003	0.208 ± 0.005	0.148 ± 0.002
Nafion 115	0.127	0.141 ± 0.003	0.161 ± 0.003	0.100 ± 0.002
Nafion 113	0.089	0.091 ± 0.002	0.111 ± 0.002	0.075 ± 0.003
Nafion 112	0.051	0.050 ± 0.002	0.058 ± 0.003	0.040 ± 0.002

2.6 *Conclusions*

Different types of fuel cells, electrolysers and some hydrogen storage modes were reviewed. It was shown that PEM electrolysers are well suited for small scale renewable systems which are inherently intermittent. This is due to their fast response to transients and fast start-up time. They can also operate at higher current densities making them to be compact and they have a solid electrolyte improving on safety by avoiding explosions. A solid electrolyte also allows compression. A pressurized electrolyser eliminates or minimizes the size of the compressor. This increases the system efficiency and lowers the capital cost of the plant. Improvement on alkaline electrolysers to zero-gap cells with a solid electrolyte will put them at an advantage over PEM electrolysers due to their reduced requirements on expensive catalysts.

An increase in electrolyser temperature improves on efficiency. The additional heat energy lowers the electrical energy requirement. This is only limited by the electrolyser materials. For PEM electrolysers, their maximum operating temperature is about 100°C. Self-starting or self-heating capability of a PEM electrolyser can be achieved by operating the electrolyser at a higher cell voltage. The electrolyser is heated to the operating temperature, whereby a controller can then be used to maintain the temperature in the operating regime.

The hydrogen production rate was shown to be dependent on current. This imposes a condition on the controller which has to hold the cell voltage at around 1.48-2V, as well as ensure the flow of maximum current. Under these conditions, the electrolyser will be operating at high efficiencies. An analytic PEM electrolyser model was also derived which will be used in subsequent work.

The major challenges facing the hydrogen economy are: lack of transport, storage and distribution infrastructure, high capital cost especially for small scale applications, technological challenges in storage, costly catalyst materials and electrodes, safe end-use of hydrogen and reliability of technologies for large scale implementation. Distributed hydrogen generation near load points will reduce transportation and distribution infrastructure while mass production will lower the production cost. Continued R&D in this field will lead to less expensive catalysts and electrodes with reduced catalytic loading and storage modes with high energy densities by volume. The hydrogen economy is favoured by the increasing demand and cost of fossil fuels with declining supply and the need for energy security. As the energy deficit increases, the hydrogen technology will become affordable with added benefits of being clean. Other fuels such as landfill gases, bio-fuels and bio-diesel will form part of the energy mix for the transport industry and distributed generation. The high cost of hydrogen

infrastructure limits hydrogen production to research and demonstration projects, remote area applications and for special applications like aerospace uses.

3 Small-Scale Use of Hydrogen and Electrolyser Sizing & Characterization

This chapter first reviews the possible small-scale end use of hydrogen. This will involve analyzing the load demand which leads to the computation of energy flow from liberation to use. Rural thermal and electrical loads are considered in the analysis. The systems which will be considered include: a biogas-electrolyser system and an electrolyser-FC system. The advantages, limitations and possible applications for these systems will be discussed. The result is a comparison of electrolyser (ELY) ratings for different loads and systems. A desired set-up is then selected from the ratings and its electrolyser characterized. Characterization will involve determining the number of electrolyser cells, the hydrogen production rate and optimum operating temperature. A Simulink® model is then used to analyse these parameters in response to a wind input. The parameters are shown to perform as expected.

3.1 *Load Characterization*

Hydrogen can drive both thermal and electrical loads. Thermal loads that will be considered are lighting and cooking. An electrical load profile is used to derive the base and peak power demands for a single household.

3.1.1 Thermal Loads

Hydrogen can be combusted to provide heat and light. This subsection draws its analysis from biogas technology. Table 3.1 compares the heating values of different fuels and their equivalent biogas replacement.

Table 3.1 Heating values for various fuels and their replacement [46]

Fuel	Heating value (kCal/m^3)	Replacement value
Biogas	4713 (20MJ/m^3 [47])	1.0 m^3
Electricity	860	4.698 kWh
Wood fuel	4700	3.414 kg
Coal	6930	1.458 kg
LPG	10882	0.433 kg
Dung cake	2092	12.296 kg
Kerosene	9122	0.620 litres

1 Cal = 4.184 J
CH_4: 32, 560 kJ/m^3 at 1 atms at 15˚ C [48]
H_2: 10, 050 kJ/m^3 at 1 atms at 15˚ C [48]
Density of H_2; 0.08376 kg/m^3 at 1 atms at 20˚ C [48]

The sizing of a biogas plant is dependent on consumption and the availability of biodegradable materials. Table 3.2 gives the consumption rate of biogas for different applications. Biogas burners are 55-60% efficient [46], [47]. They can be single or double burners. There is also a special type of burner called the *chapatti* burner [46]. Biogas lamps are similar to kerosene lamps. Their main advantage is negligible smoke, reducing respiratory and eye infections. Their illumination is equivalent to 100 candle power lamp (60W) [46]. Table 3.2 is used to compute the biogas demand per day.

Table 3.2 Quantity of biogas required for specific applications [46]

Use	Specific application	Quantity
Cooking	2" burner; 0.33m^3/hr 4" burner; 0.47m^3/hr 5" burner; 0.64m^3/hr 55-60% burner efficiency	0.3m^3 per day per person
Lighting	100 candle power lamp (60 W)	0.15 m^3/hr
Motive Power	75-80% replacement of diesel in dual fuel engine	0.50 m^3 per bhp hou

Considering a family of five as a representative of an average family in rural Africa [49]. If the family needs five hours of lighting (3½ hours in the evening and 1½ hours in the morning) for two lamps and accordingly for cooking, the total biogas demand is $3.0m^3 = \left(0.3m^3 \times 5persons\right) + \left(0.15m^3 \times 5hrs \times 2lamps\right)$ per day. The equivalent energy content is $60MJ \approx 14MCal \approx 4713kCal/m^3 \times 3m^3$ of biogas. If 60% efficiency is assumed for the burners and lamps [46], [47], then the gas demand per day is 5.0 m^3 with an approximate energy content of 24MCal = 100 MJ.

Biogas can be blended with hydrogen to improve combustion efficiency and reduce emissions. Studies have been done on hydrogen-methane or natural gas blending for vehicular applications. The conclusions from [50], [51] are synonymous. Fuel conversion efficiency is improved, there is a reduction of carbon based green house gas (GHG) emissions and improved combustion due to reduced levels of unburnt fuel. Unfortunately, the levels of nitrogen oxides (NOx) emissions increase. For every 10% increase in hydrogen content there is a corresponding 10% increase in NO_x emissions [50]. Catalytic burners which reduce the combustion temperature can be used to reduce NO_x

emissions [2]. In [52], a cost effective way of enriching[1] biogas is presented. CO_2 content in biogas is reduced from 100% to 4 % by employing water absorption of CO_2 and H_2S at high pressures. The methane content after scrubbing approached that of compressed natural gas (CNG) and it was used to fuel a CNG vehicle.

The results from [50] and [51] can be adopted although the experiments were done in controlled conditions. Values of 15-20% by volume are preferred according to [51], while [2] reports that 15% values can be adopted without changing the burners. Values above 30% have a reduced energy density coupled with potential pre-ignition of hydrogen [51]. Fig 3.1 shows the relative flame heights for different H_2/CH_4 concentrations and their thermal power. For cooking and lighting, hydrogen concentration in the range of 10-50% is acceptable due to the substantial length of the flame for lighting purposes and thermal power for cooking.

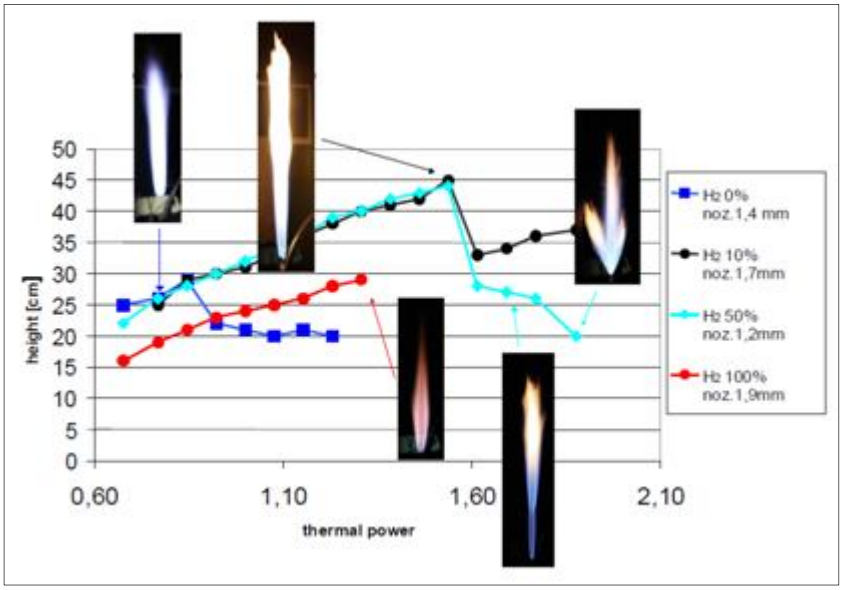

Fig 3.1 Flame heights as a function of thermal power [53]

Fig 3.2 compares two blending modes, i.e. by energy and by volume. The energy mode gives a wide range of blending ratios and meets the load requirements compared to the latter. For instance, consider a blending ratio of 1:1 for the volume mode. 50MJ is provided by the biogas while H_2 avails 25MJ.

[1] Enrichment in this context is the reduction of biogas impurities like CO_2, H_2S and water vapour in order to increase the CH_4 content to meet CNG standards. Blending is the mixing of H_2 and biogas in relative proportions with or without improving the quality of biogas.

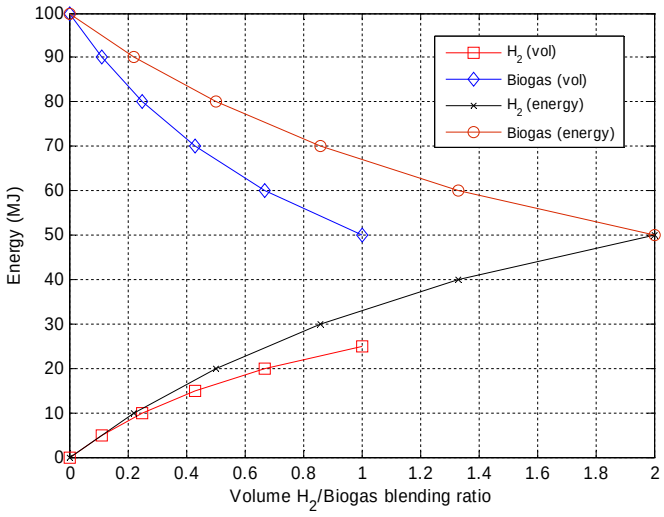

Fig 3.2 Energy requirements for H_2/Biogas blending ratios by volume and by energy

3.1.2 Electrical Loads

Fig 3.3 shows a typical 24-hour load profile for Garapola village in South Africa with 41 households. The daily total load demand is 160.8 kWh with an average of 6.7 kW and a peak power demand of 16.3 kW. Therefore for a single household, the peak power demand is 0.42 kW (17.115 kW/41) while the base demand is 0.17 kW (7.024 kW/41). This is after incorporating a 5% factor as done in [54].

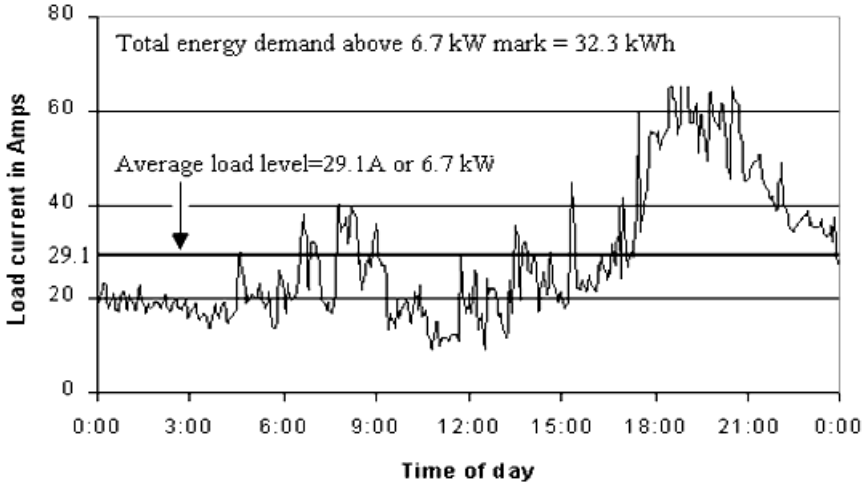

Fig 3.3 A 24-hour rural village load profile [54]

3.2 *Electrolyser System Configurations*

The scenarios to be analysed are: an *ELY-biogas blending system* which can be implemented in a rural set-up by utilising the existing biogas infrastructure, an *ELY-H_2 storage-FC combination* fit for residential applications both in rural and suburban areas and finally an *ELY-H_2 storage system* that is fit for utility companies specializing in hydrogen production and bottling. All the cases will involve small-scale hydrogen production and the advantages and limitations of each will be noted. The ELY-biogas system will be analysed using thermal loads while the ELY-H_2 storage/FC system will consider electric loads.

3.2.1 ELY-Biogas Combination

Biogas is a mixture of 50-60% methane, 30-40% carbon dioxide and traces of hydrogen sulphide, oxygen, hydrogen and water vapour among other elements. It is produced by methanogenic bacteria which act on biodegradable materials in anaerobic conditions (deficient of oxygen) [46], [47].

Biogas technology is considered to be a zero waste technology due to the utilization of both the gas as a fuel and the slurry as a form of organic fertiliser [47]. The main source of biodegradable matter is cattle dung, other animals' dung, night soils, agricultural and forest waste etc. Biodegradation of municipal waste also produces land fill gas which is rich in methane.

Assuming the biogas plant exists and was designed for $5m^3$ (100 MJ) capacity, the hydrogen generated from the wind can be used to prolong the usage of biogas and improve on its combustion. The electrolyser-simple H_2 storage system can be rated to produce a maximum volume of $5m^3$ ($= 0.42kg = 5m^3 \times 0.08376kg/m^3$) at atmospheric pressure. This corresponds to a H_2/Biogas blending ratio of 2:1, (see Fig 3.2) with an energy content of 50MJ. If the two systems were to be set-up together, the capacity of the biogas system would be reduced to 2.5 m^3 for the same ratio. The storage is simple in the sense that H_2 is not dried, cleaned or compressed. The storage holds the gas after production and the process only requires a regulation valve to control the blending ratio. The losses in this storage are deemed to be negligible.

The electrolyser rating, P_{ely} is computed from the high heat value (HHV = 49.25kWh/kgH_2). This is the case if electrical energy is assumed to be the sole source of energy and no heat is sourced from the ambient. It can be expressed as

$$P_{ely} = \frac{H_2\ demand\ in\ kg \times HHV\ of\ H_2 (49.25 kWh/kgH_2)}{24hrs \times \eta_{sys-eff}} \quad (3.1)$$

where $\eta_{sys\text{-}eff}$ is the overall system efficiency. Using an electrolyser efficiency of 56% [1], the rating for an ELY-Biogas set-up is obtained as 1.5kW. The biogas plant efficiency is neglected. If the electrolyser was to supply the total demand of 100 MJ, it would be twice the prior rating, i.e. 3kW.

The advantages of an ELY-biogas system include: reduced capital costs by the elimination of a fuel cell and its ancillaries, reduction of H_2 storage costs by using a simple storage strategy, improved combustion of biogas increasing efficiency and a reduction of carbon based GHG emissions and prolonged usage of biogas. Biogas advantages like negligible smoke which reduces respiratory and eye infections, improved sanitation, combustion of methane which is twenty times more potent than CO_2, use of slurry as a fertiliser and general improvement of livelihoods in rural areas are also realized [46].

The limitations include: it is not suited for urban or suburban areas where space is limited, shortage of raw materials for feeding the biogas system can be problematic, dependency of biogas production on pressure and temperature of the ambient can hinder reliability and it is labour intensive especially in the handling of the biogas feed and slurry. Biogas is also low in methane content which can be mitigated by blending with an increase in NO_x emissions. Shortage of water when preparing the biogas feed can be a problem considering that 1 kg of cow dung requires a litre of water [46].

3.2.2 ELY-FC Combination

The ELY-FC set-up consists of an electrolyser and a fuel cell without storage. It is assumed that hydrogen is used by the FC as it is produced. A buffer tank can be used to reduce intermittency and fuel starvation by allowing a continuous flow of hydrogen.

The ELY-FC set-up is rated using the peak power demand in order to meet transients. Incorporating other forms of electrical energy storage (EES) like batteries and super- capacitors would reduce the size of the electrolyser significantly. The peak power demand results in an overrating of the electrolyser, while the base load reduces its size by allowing the EES to meet transients. The electrolyser is rated at 1.7kW to meet peak power demand assuming efficiency values of 56% for the electrolyser, 50% [55] for the fuel cell and 90% [55] for the auxiliaries. Incorporating other forms of EES to meet transients, the rating is reduced to 0.67kW (~0.7kW) by using the base power demand.

The advantages of this set-up are reduced capital cost due to the absence of storage and its auxiliaries and improved efficiency since there are no storage losses. It also requires less space compared to H_2-biogas system and thus can be implemented in residential areas where space is limited.

Its disadvantages include: the system cannot respond to transients due to the lack of storage, there is fuel starvation in the FC due to lack of H_2 storage, it leads to overrating of the electrolyser by using the peak power demand, it is expensive than an ELY-biogas system and it requires gas drying, purification etc.

3.2.3 ELY-FC/H_2 Storage Combination

Two scenarios are considered; an ELY-H_2 storage-FC system and an ELY-H_2 storage system. Storage efficiencies are taken into account in the analysis. To compress a unit mass of hydrogen to 10-50 atms requires about 10-15MJ/kg (assume 12MJ/kg) and to liquefy hydrogen from 25˚C (298 K) to -253˚C (20 K) and maintain it at -253˚C (20 K) requires 50.4 MJ/kg [56]. Metal hydride storage requires a thermal system that removes heat during the absorption process and supplies heat during the desorption process. If waste heat from the FC or ICE is utilised, the total energy required is about 15 MJ/kg at 20 atms [56]. This is the lowest storage energy demand compared to compression and liquefaction of hydrogen.

The energy demand per day is $14.7MJ = 4.08kWh = (0.17kW \times 24hrs)$ and 36MJ = 10kWh corresponding to the base and peak energy demands respectively. This translates to $0.12kg = 4.08kWh/(33.3kWh/kgH_2)$ and 0.30kg respectively by using the low heat value (LHV = 33.3 kWh/kgH_2). It is assumed there is no water recovery in the FC.

The storage efficiency is computed from either the base load energy demand or the peak load energy demand. They give the same result. It can be expressed as

$$storage\,efficiency(\%) = \frac{stored\ energy - energy\ requirement\ \ for\ storage}{stored\ energy} \qquad (3.2)$$

For instance, to compress 0.12kg of H_2 to 10-50 atms gives a compression efficiency of

$$90\% \approx \frac{[14.7MJ - (0.12kg \times 12MJ/kg)]}{14.7MJ} \times 100\,.$$

Similarly to liquefy hydrogen to -253˚C (20 K), the liquefaction efficiency is 59% and by utilising waste heat in metal hydride storage at 20 atms, the efficiency is 88%. These efficiencies are comparable to those found in literature. According to [55], the efficiency of compression is 90% while that of liquefaction is about 65%. If electrical energy from the FC is used in metal hydrides, the efficiency is about 50% [57] and by utilising waste heat the efficiency approaches 90% [57].

1. ELY-H_2 Storage-FC Combination

This set-up incorporates the efficiencies of storage, electrolyser, FC and their ancillaries. Consider a case where hydrogen is compressed. The electrolyser rating is approximately 0.80kW, using eqn (3.1). Similarly, for liquefied hydrogen the rating is 1.1kW. If metal hydrides employ electrical energy from the FC or an independent thermal system or use waste heat from the FC or ICE, the corresponding electrolyser ratings are 1.4kW, 0.75kW(~0.8kW) and 0.77kW(~0.8kW) respectively. The above electrolyser ratings are obtained by considering the base load demand. Similarly for the peak power demand, the ratings are 1.9kW, 2.8kW, 3.3kW, 1.9kW and 1.9 kW respectively.

2. ELY- H_2 Storage Combination

In future, some of the utilities will provide bottled hydrogen for home based applications like cooking, space heating, filling of hydrogen vehicles, FCs among other applications. Hydrogen generated by the electrolyser is purified and dried to meet the expected standards. FC and its ancillaries are negated. The electrolyser ratings are as shown in Table 3.3 for different storage methods.

Table 3.3 Electrolyser ratings for ELY-H_2 storage set-up

Type of load	Compression storage (kW)	Liquefaction storage (kW)	Hydride storage (kW)		
			FC electrical power	Independent thermal system	Waste heat
Combustion	3.7	5.8	6.7	3.4	3.8
Base load	0.4	0.6	0.7	0.4	0.4
Peak load	~1.0	1.4	1.7	~1.0	~1.0

The advantages of the ELY-FC/ H_2 storage systems include: there is no fuel starvation in the FC, the system can respond to transients due to the availability of storage and they are practical, especially for residential applications. They are also versatile, for instance, ELY-H_2 storage-FC systems will not only meet electrical and thermal loads but also fuel hydrogen engines and vehicles. The ELY-H_2 storage system is vital in the refuelling of FCVs and other ICEs which are hydrogen based. Hydrogen storage also reduces space requirements significantly and it is adaptable to any locality unlike biogas systems that entirely depend on the availability of biodegradable materials and space. Their set-backs

include: they are the most expensive of all the systems and losses are also high due to more ancillaries.

Compression is preferred due to its simplicity but the need for leak and embrittlement free compressors makes it a costly option. LH_2 has high operating energy since the temperature should be kept constant at -253˚C (20 K) and the need to cool the storage container. Hydride storage has low operating energy and high volumetric energy density, moderate pressures and temperatures. The set back in hydrides is their weight which limits their use to stationary applications though they are fit for vehicular applications due to their fail safe design. The need for a thermal system to control the charging and discharging of hydride storage increases the cost of the plant [56]. Their main appeal in vehicular applications is safety. In case of an accident hydrogen cannot be released if the desorption heat is not availed. This can be compared to highly pressurised cylinders which can burst into high velocity projectiles dependent on the storage pressure and cylinder material. Table 3.4 gives a comparative summary of the electrolyser ratings for different load scenarios.

3.3 *Electrolyser Characterization*

This involves obtaining stack parameters such as the number of cells, current, voltage, operating temperature and the hydrogen production rate. The response of these parameters (except the number of cells) to a wind-speed input was modelled in Simulink®. The model consists of a wind energy conversion system, a DC/DC converter interface and a PEM electrolyser.

The ELY-H_2 storage-FC system represents the most practical and promising way of implementing the hydrogen economy. The electrolyser is rated from the base load and H_2 storage allows the system to meet transient demands. An alternative is to have a hybrid system where the FC supplies the base load while the EES and H_2 storage meet the transients. ELY-H_2 storage-FC set-ups with a 0.8kW rating are selected from Table 3.4. Their storage modes are compression and hydride storage (independent thermal system or waste heat). The set-up utilizing compression storage will be used as an example in determining the various parameters of an electrolyser.

A 0.8kW electrolyser would generate $0.5765 kgH_2 = (0.8kW \times 24hrs)/(33.3kWh/kgH_2)$ per day. The LHV value is once again used assuming there is no water recovery in the fuel cell, that is, combusting a unit mass of hydrogen in the FC gives 33.3 kWh in the form of electrical energy.

Table 3.4 A comparative summary of electrolyser ratings for different load scenarios

Scenario	Load	Ely. 56%	F.C. 50%	Aux. 90%	Storage					Ely. rating kW	Comment
					Comp. 90%	Liq. 59%	Hydride				
							50%*	90%+	88%×		
BiogasTh	4.17MJ									-	Biogas system only; 5 m^3 capacity
H_2-biogasTh	0.86kW	✓								1.5	5m^3H_2 at 1atm; 2.5m^{3}Biogas (50MJ)
H_2Th	1.72kW	✓								3.0	10m^3H_2 at 1atm
H_2-FC^{El}	0.17kW	✓	✓	✓						0.7	Immediate use of H_2 by FC
	0.42kW	✓	✓	✓						1.7	
H_2-Storage-FC^{El}	0.17kW	✓	✓	✓	✓					0.8	Compressed H_2
		✓	✓	✓		✓				1.1	Liquefied H_2
Note:		✓	✓	✓			✓			1.4	Electrical thermal system powered by FC
0.17kW-base load		✓	✓	✓				✓		0.8	Independent thermal system
0.42kW-peak load		✓	✓	✓					✓	0.8	Use of waste heat
Th Thermal load	0.42kW	✓	✓	✓	✓					1.9	Compressed H_2
^{El} Electrical load		✓	✓	✓		✓				2.8	Liquefied H_2
		✓	✓	✓			✓			3.3	Electrical thermal system powered by FC
		✓	✓	✓				✓		1.9	Independent thermal system
		✓	✓	✓					✓	1.9	Use of waste heat
H_2-StorageTh	1.72kW	✓		✓	✓					3.7	Compressed H_2
		✓		✓		✓				5.8	Liquefied H_2
		✓		✓			✓			6.7	Electrical thermal system powered by FC
		✓		✓				✓		3.4	Independent thermal system
		✓		✓					✓	3.8	Use of waste heat
H_2-Storage^{El}	0.17kW	✓		✓	✓					0.4	Compressed H_2
		✓		✓		✓				0.6	Liquefied H_2
		✓		✓			✓			0.7	Electrical thermal system powered by FC
		✓		✓				✓		0.4	Independent thermal system
		✓		✓					✓	0.4	Use of waste heat
	0.42kW	✓		✓	✓					1.0	Compressed H_2
		✓		✓		✓				1.4	Liquefied H_2
		✓		✓			✓			1.7	Electrical thermal system powered by FC
		✓		✓				✓		1.0	Independent thermal system
		✓		✓					✓	1.0	Use of waste heat

Key: **Ely.** – Electrolyser; **F.C.** – Fuel Cell; **Aux.** – Auxiliary; **Comp.** – Compression; **Liq.** – Liquefied.

* Hydride storage powered by an electrical system (FC), a part of the primary system.

\+ Hydride storage powered by an independent system such as a solar water heater system.

× Hydride storage utilising waste heat from a FC or ICE.

The hydrogen production rate per hour is $0.024kg/hr = (0.5765kgH_2/day)/24hrs$, which can be associated with eqn (2.15) as

$$0.024\text{kg/hr} = 7.5816\frac{\eta_c I_{ely}}{zF} \tag{3.3}$$

$I_{ely}(A) = i(A/cm^2) \times A_{elc}(cm^2)$, where A_{elc} is the active area of the electrodes. The active area of a typical stand-alone PEM cell is about 100cm^2 with a maximum current density of 1.0A/cm^2 at an operating cell voltage of about 2.0-2.2V [11]. It is important to note that higher current densities (higher current loading) lead to membrane degradation [11]. Substituting *z*, *F* and A_{elc} into eqn (3.3), the number of electrolyser cells can be expressed as a function of the current density, i.e. $\eta_c = 6.1/i$. The operating current density is chosen in the mid-band of 0.4-0.8A/cm^2. Letting i = 0.55A/cm^2 gives 11 electrolyser cells. The maximum stack voltage U_{ely} is therefore $24V \approx 11cells \times 2.2V$.

Substituting η_c = 11 into eqn (3.3) gives a nominal stack current, I_{ely} of 55.5A which is close to 55A computed from the current density. The resulting DC power rating of the electrolyser is in the range of 0.90-1.33kW corresponding to 1.5-2.2V cell voltage for a rated current of 55A. 1.5V is an approximation of the thermoneutral voltage U_{tn} = 1.481V. This is the minimum cell voltage required before current starts to flow [11]. Hydrogen is not generated below this voltage. By increasing the number of cells and connecting them in series, the current rating of the electrolyser can be significantly reduced with a corresponding increase in the stack voltage. For a given number of cells and a fixed cell voltage, the hydrogen production rate becomes a function of current.

A PEM electrolyser has a fast temperature response compared to an alkaline electrolyser due to a reduced thermal mass. The temperature response of a 14-cell stack with 100cm^2 active area without insulation was done in [11], in a thermal self-sustaining mode. The temperature of the feed water was 22˚C. The stack reached its operating temperature as the current density increased to 1.0A/cm^2, with the water exiting at 85-86˚C. The temperature response for 0.8A/cm^2, 0.6A/cm^2 and 0.5A/cm^2 current densities was 80˚C, 73˚C and 67˚C respectively. The heat was generated internally by resistive losses. This proves that it is possible to achieve thermal self-sustaining operation in a stand-alone PEM electrolyser. The desired density can be achieved by adjusting the current or the active area. To achieve 0.8A/cm^2 current density, the active area is reduced to 68cm^2 for a stack current of 55A. It can also be increased to 80A for an active area of 100cm^2. From the data adopted from [11], the variation of temperature as a function of current density can be approximated by a quadratic equation using MS Excel® as

$$T_{ely}(°C) = -83.333i^2 + 151.67i + 12 \qquad (3.4)$$

According to eqn (2.18) efficiency is only dependent on the cell voltage, $U_{cell} \approx U_{ely} / \eta_c$. Faradic efficiency is neglected since it is over 90%, and it is even higher for non-degraded cells [11]. In Fig 3.4(a) efficiency decreases with increasing cell voltage while the specific energy use increases linearly with cell voltage. Fig 3.4(b) shows the effect of increasing the cell voltage for a constant stack current. The production rate is constant but power and the stack voltage increases. This means that more energy is used to produce a unit mass of H_2, and hence the rise in the specific energy use as the cell voltage increases.

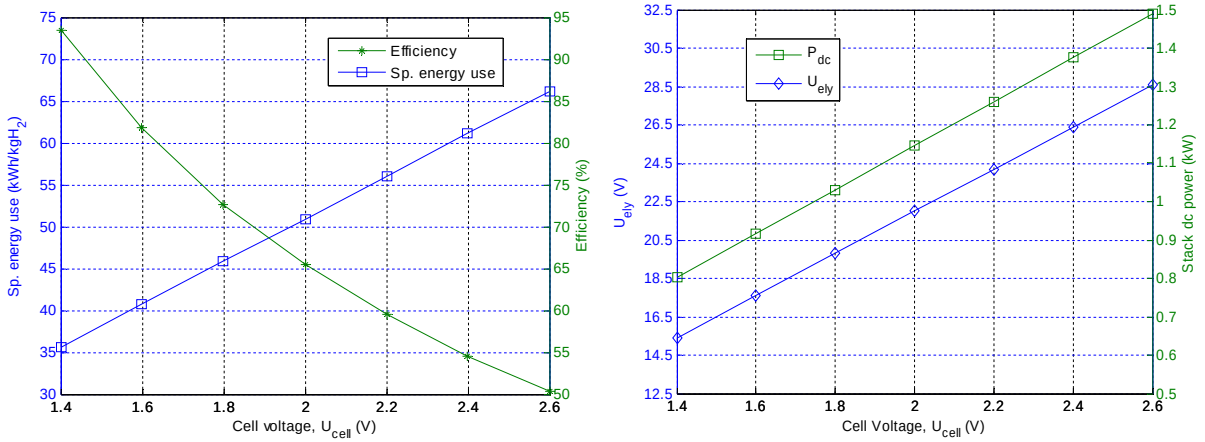

(a) Efficiency and the Specific energy use **(b) Electrolyser rating, P_{ely} and stack voltage, U_{ely}**

Fig 3.4 Electrolyser parameters vs. cell voltage for η_c = 11 cells at I_{ely} = 52A at a H_2 production rate of 22.5g/hr

3.4 *Generator - Electrolyser Interface*

The electrolyser can be interfaced to the generator via a DC/DC converter. The functions of the interface are to extract maximum power from the available wind, limit the current and maintain the output voltage at the electrolyser input. The most popular converter topologies are the buck converter that steps down the input voltage, the boost converter which steps up the input voltage and a combination of the two - the buck-boost converter. The buck-boost topology is selected due to its ability to step-up or step-down the input voltage to the rated output voltage. These low and high input voltages correspond to the low and high wind speeds respectively. Its shortcoming is reduced output to input voltage ratio V_o / V_d as the duty ratio D approaches unity due to parasitic effects. This is due to losses associated with the inductor, the capacitor, the switch and the diode. It also has poor switch utilisation at lower and higher duty ratios [58].

The real power of the generator, P_{gen} can be expressed as a function of the wind turbine power, P_{WT} as $P_{gen} = n_{gen} P_{WT}$, where η_{gen} is the generator efficiency.

$$\left.\begin{aligned} P_{gen} &= \eta_{gen} \times \frac{1}{2} C_p \rho \pi R^2 v_m^{\,3} \\ TSR = \lambda &= \frac{R\omega_m}{v_m} \end{aligned}\right\} \qquad (3.5)$$

A typical 3-bladed Horizontal Axis Wind Turbine (HAWT) has a tip speed ratio, TSR in the range of λ = 5-7 with an optimum power coefficient C_p in the range of 0.35-0.45 [59]. R is the radius of the wind

turbine, ω_m is the mechanical angular velocity, ρ = 1.204kg/m^3 is the air density at 20˚C and 1 atms and v_m is the mean wind speed. The shaft speed, n in rev/min and electrical frequency, f in Hz can be obtained from the TSR as

$$\left.\begin{aligned} n &= \frac{\lambda v_m 60}{2\pi R} \\ f &= \frac{pn}{60} \end{aligned}\right\} \tag{3.6}$$

where p is the number of pole pairs.
The phase voltage, V_{an} can be expressed as a function of the induced back EMF, E_f as

$$V_{an} = \frac{E_f}{\varepsilon} = \frac{\pi\sqrt{2} f N_{ph} k_{w1} \phi_p}{\varepsilon} \tag{3.7}$$

where ε is the ratio of the no-load and load voltages, N_{ph} is the number of turns per phase, k_{w1} is the fundamental winding factor and ϕ_p is the flux per pole. The output voltage of the converter which is the input of the electrolyser U_{ely} can be given as

$$U_{ely} = \left(\frac{D}{1-D}\right) \cdot 1.35 \cdot \sqrt{3} V_{an} \cdot \eta_{convr} \cdot \eta_{rect} \tag{3.8}$$

where η_{convr} and η_{rect} are the converter and rectifier efficiencies respectively. Equation (3.8) can be used to get the duty ratio D since U_{ely} can be set for a given number of electrolyser cells. This can be done by use of the battery pack that powers the electrolyser auxiliaries. The controller should then vary the duty ratio until the electrolyser voltage reaches the set point. After obtaining the phase voltage and duty ratio, the phase current can be obtained from eqn (3.5) and the real power expression as

$$I_{s(rms)} = \frac{\eta_{gen} \times \frac{1}{2} C_p \rho \pi R^2 v_m^3}{3 V_{an} Cos\phi} \tag{3.9}$$

The electrolyser stack current I_{ely} can then be given a function of which is the output of the converter can be obtained as a function of D and $I_{s(rms)}$ as

$$I_{ely} = \left(\frac{1-D}{D}\right) \cdot \frac{1}{0.816} I_{s(rms)} \cdot \eta_{convr} \cdot \eta_{rect} \tag{3.10}$$

A Simulink® model was developed to simulate the wind energy conversion system, a buck-boost converter interface and a PEM electrolyser model derived in eqn (2.29). The input to the model is the wind speed v(m/s) and the outputs are the generator's phase voltage V_{an} (V) and phase current $I_{s(rms)}$ (A), the converter's duty ratio D (%), reference voltage $U_{ely\text{-}REF}$ (V), stack voltages U_{elyA} (V) and U_{elyB} (V) , current I_{ely} (V) and temperature T_{ely} (˚C) and the hydrogen production rate in g/hr. The results for a ramp input are shown in Fig 3.5(a) to (d). The Simulink® model is attached in Appendix B.

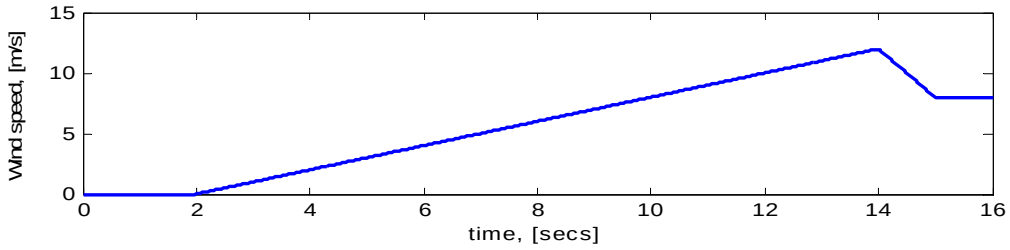

(a) A ramp wind-speed, *v* input

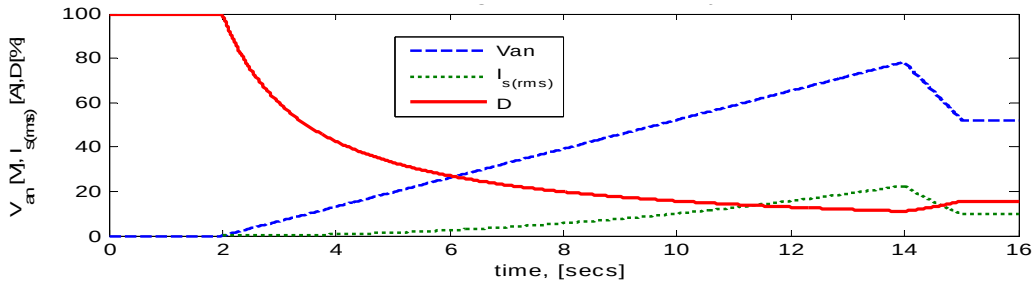

(b) Phase voltage, V_{an}, current, $I_{s(rms)}$ and duty-ratio, D

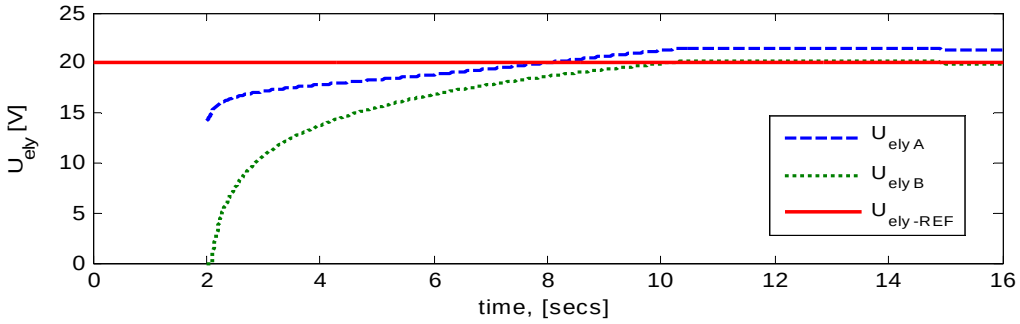

(c) Electrolyser stack voltages, U_{elyA} & U_{elyB} and reference voltages, $U_{ely\text{-}REF}$

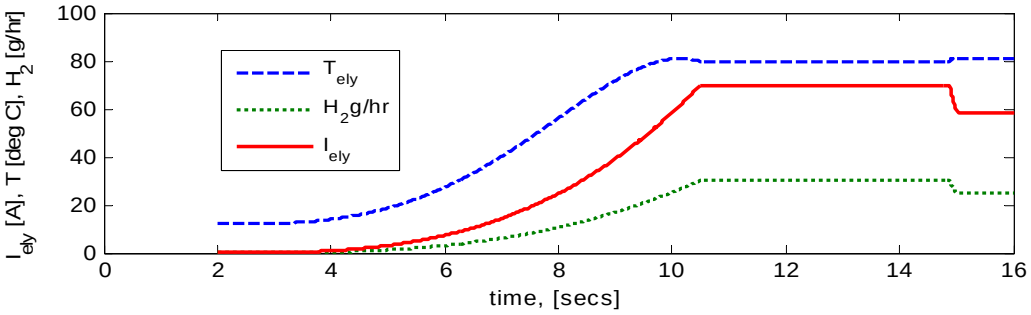

(d) Stack temperature, T_{ely}, current, I_{ely} and production rate, H_2g/hr

Fig 3.5 Response of the Simulink® model to a ramp wind-speed input

As seen in Fig 3.5(b), the output of the generator follows the wind speed and the duty ratio decreases proportionately. The reference electrolyser voltage, $U_{ely\text{-}REF}$ ($=20V=11cells\times 1.81V/cell$) as seen in Fig 3.5(c) is used to obtain the duty-ratio as discussed earlier. The stack parameters in response to the input are shown in Fig 3.5(c) and (d). U_{elyA} is from a PEM electrolyser model derived in eqn (2.29), while U_{elyB} is a comparative empirical expression obtained from Fig 2.9 and modified to include the number of cells as $U_{elyB}=\frac{\eta_c}{13.55}Log\left(\frac{I_{ely}}{0.00009}\right)$. It can be seen that the electrolyser model derived has a higher stack voltage which can be attributed to a higher cell voltage for self-starting capabilities.

The flat tops in Fig 3.5(c) and (d) are due to current limiting by use of saturation blocks provided in Simulink®. The temperature response of the stack is dependent on the stack current as evidenced on Fig 3.5(d). According to the model, hydrogen is produced when the voltage is greater than 1.481V, i.e. when current starts flowing as seen in Fig 3.5(c) and (d). The above discussion holds for the results in Fig 3.6(a) to (b) for a varying input which is within the operating wind speed of 8.5m/s. The effect of wind variation is seen clearly on the electrolyser parameters in Fig 3.6(c) and (d). The transients experienced by the electrolyser can be minimized by incorporating an EES system. This will increase its service life.

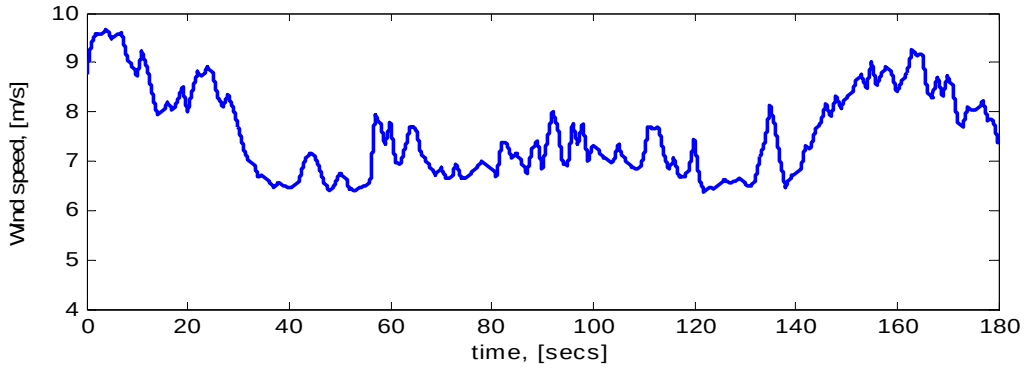

(a) Varying wind-speed, *v* input

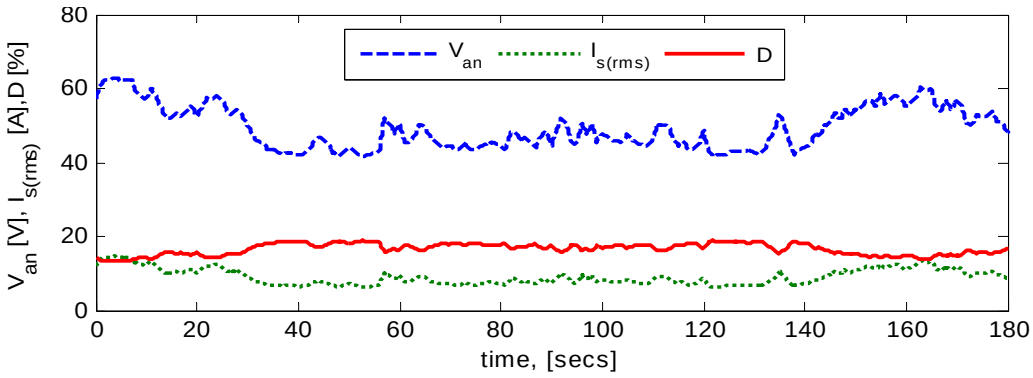

(b) Phase voltage, V_{an}, current, $I_{s(rms)}$ and duty-ratio, D

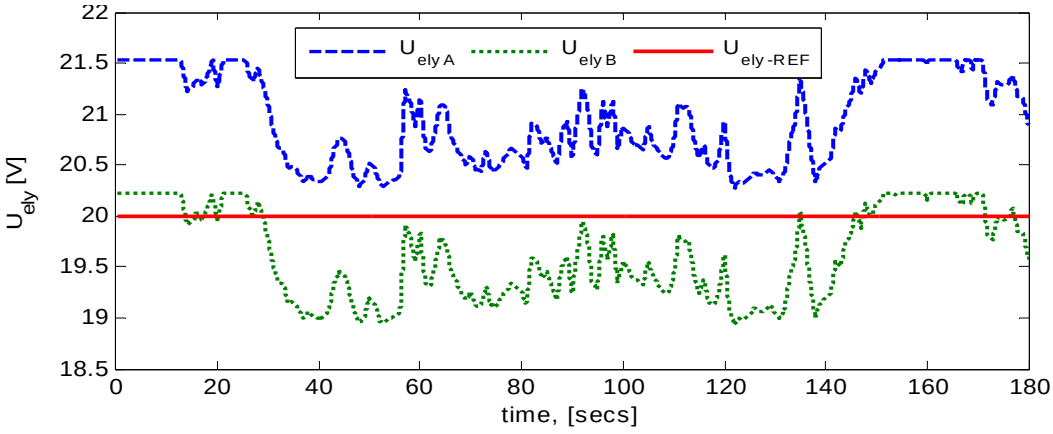

(c) Electrolyser stack voltages, U_{elyA} & U_{elyB} and reference voltages, $U_{ely\text{-}REF}$

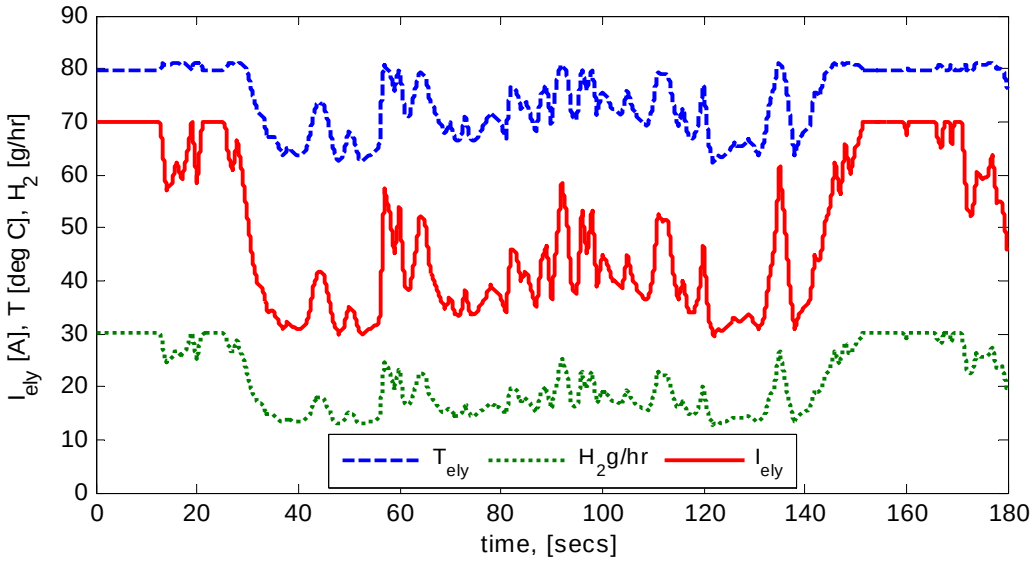

(d) Stack temperature, T_{ely}, current, I_{ely} and production rate, H_2g/hr

Fig 3.6 Response of the Simulink® model to a varying wind-speed input

3.5 *Conclusions*

The future of biogas systems in rural areas is uncertain due to the predicted increase in global populations and global warming. This will put a strain on the availability of organic materials which feed the biogas digester. The alternative to biogas systems is tapping of landfill gas which has to be implemented on a large scale basis, or the use of biogas systems in commercial farms which specialize in animal husbandry. This will prompt the replacement of rural small-scale biogas systems with ELY-H_2 storage-FC systems. These systems are well positioned for both the rural and urban settings. Currently their cost prohibits their implementation.

Compression presents the easiest means of storing hydrogen though the space requirement will be greater than that of hydrides and liquid storage. Liquid storage has the least volume requirement, but it requires more storage energy per unit mass of hydrogen compared to hydrides and compression. It also requires the freezing of the storage to prevent the boiling of hydrogen. Metal hydrides also have less volume than compressed hydrogen but their storage structure is heavy. The prohibitive cost of hydrogen compressors allows hydrides to emerge as the best storage option.

To realize a residential system independent of the grid, an ELY-H_2 hydride storage-FC system is best placed. A variation of the same system would incorporate a pressurized electrolyser that eliminates the need of compressing hydrogen. To further lower the capital costs of the hydrogen system, a set-up incorporating a PEM electrolyser-H_2 storage-EES-FC is recommended. It was seen by just sizing the electrolyser using the base load, the rating was lowered to 0.8kW from 1.7kW using the peak requirement. The ELY-H_2 storage system would be the most expensive since it caters for all forms of storage and loads as shown in Table 3.4.

The analysis provides a guide in the sizing of an electrolyser by considering the load requirements and efficiencies. It led to the characterization of an 11-cell stack, 1kW, 55A and 20V PEM electrolyser with a production rate of 24g/hr operating at 80-100˚C. It was also seen that as the cell voltage increased beyond 1.481V, for constant stack current, the efficiency dropped and the specific energy increased. The excess energy is dissipated as heat. This can be used in the electrolyser start-up procedure in order to reach the operating temperature. The electrolyser temperature and the hydrogen production rate were also shown to be dependent on the current density.

4 Axial-Flux Topologies and Analytical Modelling

Chapters Two and Three lead to the selection and characterization of a PEM electrolyser and also touched on the generator-electrolyser interface. This chapter reviews axial-flux machine topologies and analytical modelling and sizing equations. The latter will be used in the design and analysis of the generator.

4.1 *AFPM Topologies*

AFPM machines can be either single-sided or double-sided. Classification can also be based on the rotor structure. This results in variations in internal or external rotors, which have surface mounted, buried or interior PMs. They can also be single or multi-stage machines with cored or coreless armatures which can be slotted or slotless [22], [24].

4.1.1 Single-sided AFPM Machines

Single-sided machines have one airgap that separates the rotor and the stator as shown in Fig 4.1. According to [24], they have less torque. Their main disadvantage is a strong axial force exerted on the cored stator by the rotor magnets. This force can be reduced by introducing a dummy stator or rotor.

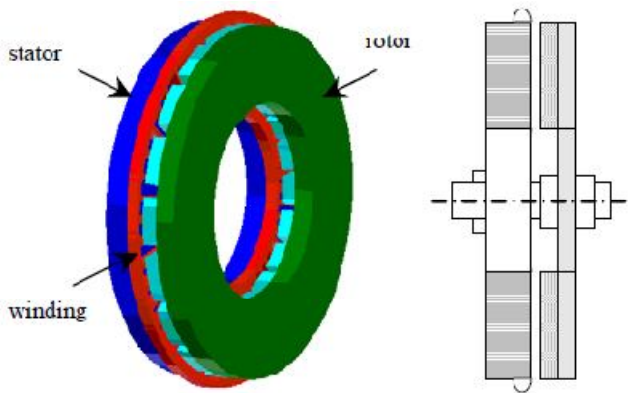

Fig 4.1 Single-sided AFPM structure [22]

4.1.2 Double-sided AFPM Machines

A double-sided machine has two airgaps. This topology can either have a single interior stator with two exterior rotor discs or a single interior rotor disc with twin exterior stators. A twin exterior stator-internal rotor or Axial Flux Internal Rotor (AFIR) topology has two stator cores connected in series or parallel with the PM disc sandwiched between them. The stators can be slotted or slotless but not ironless due to the need for the flux return path. The advantage of a parallel connected stator is continued operation even when one stator fails. It is prone to unbalanced axial forces if the stator currents are not balanced [60]. Series connection is therefore preferred due to cancellation of axial attractive forces [24]. Fig 4.2 shows the flux path in an AFIR machine.

A twin PM rotor-internal stator or TORUS machine can have a cored, coreless, yoke-less or ironless stator. Cogging torque and magnetic saturation are eliminated in slotless and ironless stators. The structure has relatively high inertia due to the two rotor discs that can smooth out torque pulsations at high speeds.

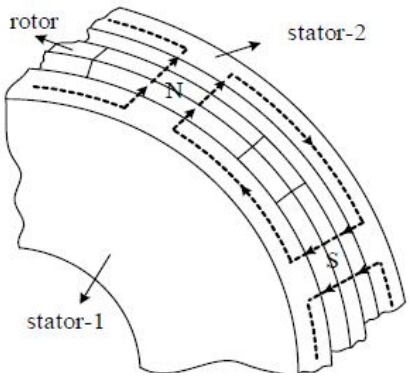

Fig 4.2 Flux path in an AFIR machine [22]

The magnets on opposite discs can be mounted such that NN and NS are realized. Fig 4.3 (a) and (b) illustrate the flux path in a NN and NS configurations respectively. The NN configuration has a longer axial length. Its stator yoke has to be thicker to allow for the summation of fluxes from the two rotor discs. For a NS configuration, the stator can be coreless, ironless, yoke-less with parallel-teeth. Cored machines can also be slotted or slotless.

The magnet grade is lower in a cored design than in a coreless design. This is due to its small airgap and the need to limit the saturation of the magnetic circuit. It also has higher airgap flux density, hence it has less winding losses i.e., eddy-current and copper losses. Unfortunately, core losses increase and a slotted stator introduces cogging torque. Internal coreless stators eliminate iron losses and cogging torque, but eddy-current losses are more pronounced than in a cored design. Coreless

topologies are characterized by their wide airgaps; hence their armature reaction is negligible. Their airgap flux density is also low, thus their number of turns per phase is usually high for the same rating as a cored topology. They also require a large volume of high energy PMs than a cored stator to increase the airgap flux-density.

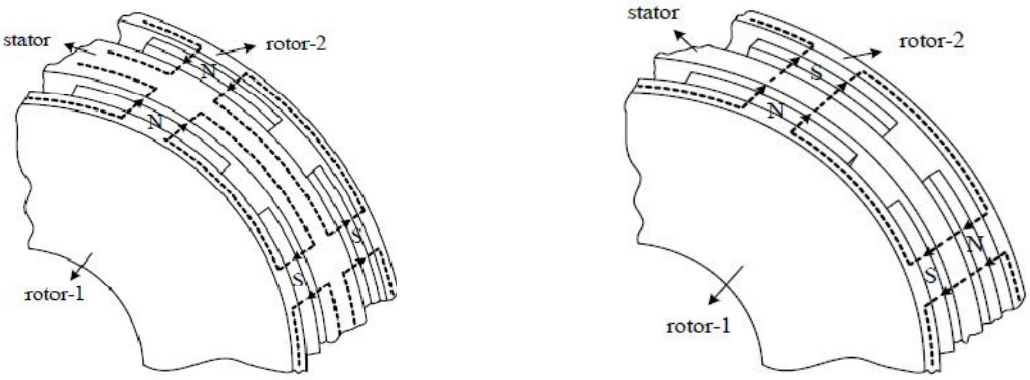

(a) NN configuration **(b) NS configuration**

Fig 4.3 Flux paths in a TORUS machine [22]

4.1.3 Multi-disc AFPM Machines

Single-stage machines can be stacked to obtain multi-disc machines allowing higher torque ratings. The increase of torque in single-disc machines is limited by the axial force taken by the bearings, stiffness of the discs and the mechanical joint between the disc and the shaft [22], [24]. Generally, a multi-disc machine has *n* stators and *n*+1 rotor discs, where *n* is the number of stages as shown in Fig 4.4. Rotors share the same mechanical shaft, while stators are either parallel or series connected. Multi-disc machines are formed by combining a number of single stages, while keeping in mind their flux path. Thus, topologies such as cored or coreless, slotted or slotless, NN or NS and their combinations can be realized.

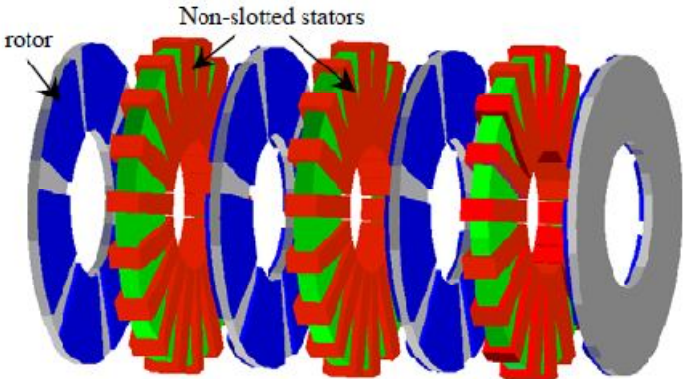

Fig 4.4 A slotless multi-disc machine for *n* = 3 [22]

4.2 *Magnetic Circuits*

Magnetic circuits can be represented by either Thevenin or Norton equivalent circuits as shown in Fig 4.5 where F_c is the coercive MMF, ϕ_M is the magnet flux and R_p is the internal reluctance.

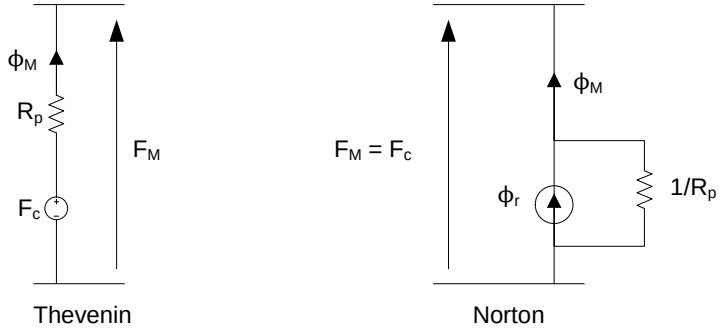

Fig 4.5 Magnetic equivalent circuits

F_c is the MMF needed to coerce the magnet to produce zero flux. It represents the resistance of a magnet to demagnetisation. ϕ_r is the remanent flux which remains in the magnet after magnetisation. The ability of a magnet to retain flux depends on both F_c and ϕ_r. In normal operating conditions, the flux is below ϕ_r due to MMF drops along the flux path. These drops are across the airgap, along the rotor and stator cores and also due to armature reaction effects. These drops act as negative demagnetizing MMFs as seen from the magnet 'terminals'. ϕ_r and F_c are dependent on the material properties and dimensions of the magnet through the following relations

$$\left.\begin{aligned} \phi_r &= B_r A_M \\ F_c &= H_c l_m \end{aligned}\right\} \qquad (4.1)$$

where B_r, A_M, H_c and l_m are the remanent flux density, magnet pole area, magnetizing force of coercivity/magnetic field intensity and the magnet depth.

4.2.1 Demagnetization Characteristic of a PM Material

The demagnetization characteristic of a PM material is expressed as

$$B_M = \mu_{rec}\mu_o H_M + B_r \tag{4.2}$$

This characteristic is shown in Fig 4.6. At the operating point, the flux and the MMF drop are $\phi_M = B_M A_M$ and $F_M = H_M l_m$ respectively. The operating point moves up and down on the slope of the demagnetizing characteristic. This slope is the relative recoil permeability, μ_{rec} in the range of 1.05-1.15 for NdFeB magnets. When the armature current is zero, the operating point is at the Open-Circuit Operating Point, as shown in Fig 4.6. At this point, B_M is in the range of 0.7-0.95 of B_r [61]. The load line intersects the origin and the Open-Circuit Operating Point. The characteristic is often plotted with the horizontal axis being $\mu_o H$ instead of H. For this case, the slope of the load line gives the Permeance Coefficient, PC in the range of 5-15 [61]. When current flows through the armature windings, its demagnetization effect may push the operating point further down, and when it is withdrawn, the operating point recovers to the open circuit point. The recovery is possible as long as the operating point has not left the straight part of the characteristic.

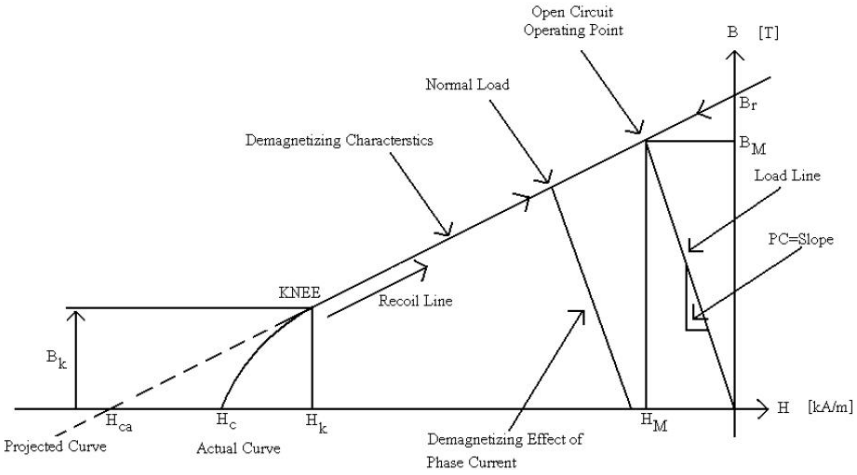

Fig 4.6 B-H characteristic of a permanent magnetic material [61]

The recoil line intersects the negative H axis at the apparent coercivity, H_{ca} point; which is also called the intrinsic coercivity, H_{ci}. The best grades of PMs have a demagnetization characteristic that remains straight in the second quadrant. In some cases, the characteristic may even extend to the third quadrant. This allows the magnets to withstand a demagnetization force that actually reverses flux in the magnet, and still recover with no permanent loss of magnetism. If the operating point extends below the knee, the magnet recovers along a lower recoil line when the demagnetizing field is removed. The knee point can arise as a result of operating the magnets at higher temperatures; a

characteristic of some grades of SmCo and NdFeB or at lower temperatures; a characteristic of ferrite magnets [61].

The remanent flux density, B_r is affected by the operating temperature as shown in Fig 4.7 and can be expressed as [61]

$$B_r(T) = B_r(20) \times (1 + \alpha_{Br}(T - 20)/100) \tag{4.3}$$

where α_{Br}, $B_r(20)$ and T are the reversible temperature coefficient in % per ˚C, B_r at 20˚ C and temperature in ˚C respectively.

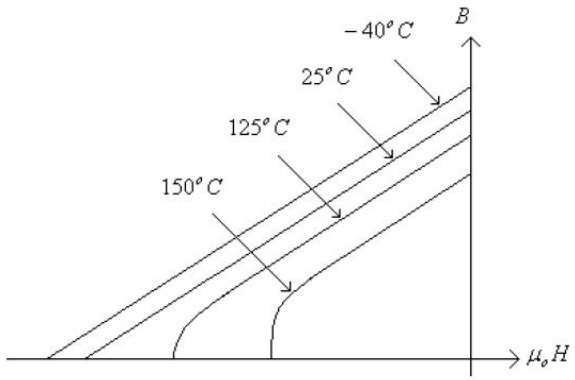

Fig 4.7 Effects of temperature on the demagnetization characteristic [61]

4.2.2 Approximate Calculation of Flux

It requires the identification of the main flux paths and the assignment of reluctances to the magnetic circuit as shown in Fig 4.8(a) and (b). The airgap flux, ϕ_g links the coils of the armature windings. The ratio of air gap flux, ϕ_g to magnet flux, ϕ_M is the leakage coefficient, f_{LKG} which lies within 0.9-0.95 [61]. It is given as

$$f_{LKG} = \frac{\phi_g}{\phi_M} = \frac{\phi_g}{\phi_g + \phi_l} = \frac{R_L}{R_L + R_g} < 1 \tag{4.4}$$

where R_L, R_g and ϕ_l are the leakage reluctance, the airgap reluctance and the leakage flux respectively.

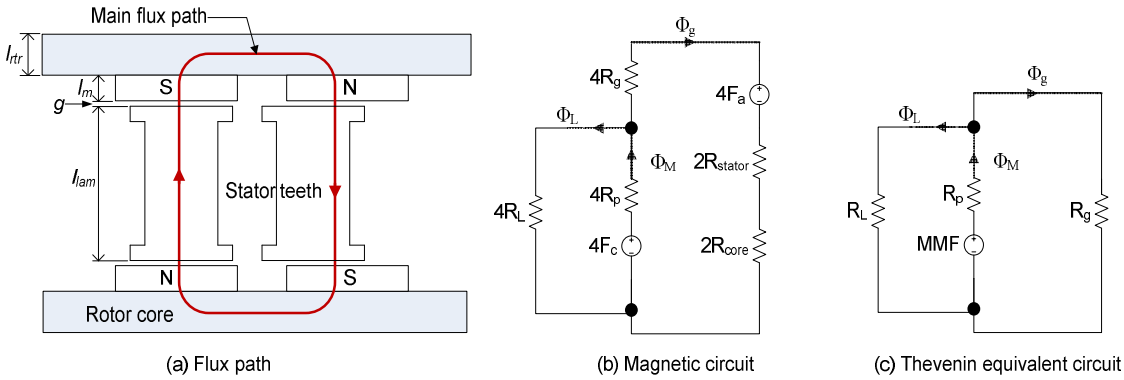

(a) Flux path (b) Magnetic circuit (c) Thevenin equivalent circuit

Fig 4.8 Magnetic circuit of a twin rotor- internal stator AFPM

The MMF ($=R_p\phi_r$) from the magnet drives the useful flux, ϕ_g through the airgap, R_g, stator, R_{stator}, and the rotor iron core, R_{core} reluctances. If armature reaction effects, F_a are neglected and the permeabilities of the stator and rotor are assumed to be high enough, the simplified circuit is as shown in Fig 4.8(c). The magnetic reluctance, R_p and airgap reluctance, R_g can be expressed as $R_p = l_m/(\mu_o\mu_{rec}A_M)$ and $R_g = g/\mu_o A_g$ respectively. g and A_g are the physical airgap and the area of the airgap respectively. Applying the analogous current divider rule to ϕ_g and ϕ_M as shown in

Fig 4.8 Magnetic circuit of a twin rotor- internal stator AFPM

Fig 4.8(c), the relationship between the two fluxes is

$$\phi_g = \phi_M \frac{R_L}{R_L + R_g} \tag{4.5}$$

After some manipulations, ϕ_g is given as

$$\phi_g = \frac{f_{LKG}}{1 + f_{LKG}\left(R_g/R_p\right)}\phi_r \tag{4.6}$$

The permeance coefficient, PC can be expressed as [61]

$$PC = \frac{1}{f_{LKG}} \cdot \frac{l_m}{g} \cdot \frac{A_g}{A_M} \tag{4.7}$$

and related to B_M through

$$B_M = \frac{PC}{PC + \mu_{rec}} B_r \,. \tag{4.8}$$

B_M must always be greater than the knee flux density, B_k . A minimum B_M is obtained as $0.83B_r$ when $PC = 5$. μ_{rec} is assumed to be unity for hard magnets. If PC is unity, the operating point corresponds to the PM's maximum energy product, $(BH)_{max}$. At this point $B_M = 0.5B_r$, which is at half the characteristic. This is rarely used in order to avoid the demagnetizing effects of armature current and temperature. The ratio A_M/A_g is the flux focusing/concentrating factor C_Φ. For open-circuit condition, the magnet volume per pole is given as $V_M = 2W_g / |B_M H_M|$, where $W_g = B_g H_g / 2 \times A_g \times g$ is the magnetic energy stored in the airgap per pole [61].

The airgap flux density, B_g can be obtained by applying KVL to Fig 4.8(b). Leakage flux and armature reaction effects are neglected while the stator and rotor core permeabilities are assumed to be high. This gives

$$H_M l_m + H_g g = 0 \tag{4.9}$$

Substituting $H_g = B_g / \mu_o$ into eqn (4.9) gives $H_M = -B_g g / (\mu_o l_m)$ which when substituted into the demagnetizing equation results in

$$B_M = -\frac{\mu_{rec} B_g g}{l_m} + B_r . \tag{4.10}$$

But, $B_M = B_g A_g / (A_M f_{LKG}) = B_g / (C_\phi f_{LKG})$, by substituting this into eqn (4.10), B_g can be expressed as

$$B_g = \frac{B_r}{\frac{A_g}{A_M f_{LKG}} + \frac{\mu_{rec} g}{l_m}} = \frac{B_r}{\frac{1}{C_\phi f_{LKG}} + \frac{\mu_{rec} g}{l_m}} \tag{4.11}$$

which is an approximation of the airgap flux density.

4.2.3 Nonlinear Calculation of a Magnetic Circuit

The previous calculations neglected the MMF drops in the steel parts of the magnetic circuit. In this case, the useful flux is assumed to cut through the airgap, stator yoke, stator teeth and rotor yoke for

half a pole area. The resultant voltage drop is obtained by using KVL and adding the MMFs together, that is [61]:

$$F = F_g + F_{sy} + F_{st} + F_{ry} + F_M \tag{4.12}$$

where $F_M = H_M l_m$, $F_g = g' \times B_g / \mu_o$ and $F_{sy} = H_{sy} \times L_{sy}$. L_{sy} is the flux-path through the stator yoke over one-half pole-pitch. F_{st} and F_{ry} are the MMF drops across the stator teeth and the rotor core respectively. If the stator yoke flux is assumed to be equal to the airgap flux, then $B_{sy} = B_g \times A_g / A_{sy}$ Therefore, $H_{sy} = f(B_{sy})$ can be obtained from the B-H curve of the stator steel. Equation (4.12) is iterated. If $F > F_{ca} = H_{ca} l_m$, B_g is decreased and the calculation repeated. If it is less, B_g is increased. This is done until F is within 0.1% of F_{ca}. Armature reaction effects are also neglected.

4.3 *Torque Production*

The electromagnetic torque in an AFPM is produced over a range of radii unlike in a cylindrical machine where it occurs at a fixed radius [24]. Therefore relations like flux, developed torque and EMF will be shown to be dependent on the inner and outer diameters of the machine. Pulsating torque which comprises ripple torque and cogging torque is also reviewed.

4.3.1 Magnetic Flux

The average sinusoidally distributed magnetic flux density, B_{ave} is given as $B_{ave} = 2/\pi \, B_{mg}$, while for nonsinusoidal it is $B_{ave} = \alpha_i B_{mg}$, where B_{mg} is the peak/plateau value of the magnetic flux density [24]. The magnetic flux per pole due to the nonsinusoidal magnetic flux is [24]

$$\begin{aligned} \phi_p &= \alpha_i B_{mg} \frac{\pi}{2p} \left(R_o^2 - R_i^2 \right) \\ &= \alpha_i B_{mg} \frac{\pi}{8p} D_o^2 \left(1 - k_d^2 \right) \end{aligned} \tag{4.13}$$

α_i can also be expressed as $\alpha_i = b_p(r)/\tau(r)$ where $b_p(r)$ is the pole-width and $\tau(r) = \pi r/(2p)$ is the pole-pitch at a radius r [24]. $k_d = D_i / D_o$ is the ratio of internal diameter, D_i and outer diameter, D_o

of the PMs. k_d is optimum at either 0.57 or 0.63 for high torque to weight ratio or maximum power [62], [63], 0.68 for maximum efficiency and about 0.7 for minimum magnet volume [64]. The flux per pole can also be expressed as [59]

$$\phi_p = \frac{B_{1\max} L_e D_g}{p} \tag{4.14}$$

where $L_e = (D_o - D_i)/2$, $D_g = (D_o + D_i)/2$ and $B_{1\max}$ are the effective length, average diameter and the specific magnetic loading – the peak value of the fundamental airgap flux density respectively. For a cylindrical machine, the flux per pole is given as $\phi_p = \frac{2}{\pi}\tau L_e B_{mg}$, where L_e is the effective length of an RFPM machine and τ is the pole pitch [24].

4.3.2 Electromagnetic Torque and EMF

The average electromagnetic torque or the developed torque, T_d can be given as [24]

$$\begin{aligned} T_d &= \frac{1}{4}\alpha_i m_1 N_{ph} k_{w1} B_{mg} D_o^2 (1 - k_d^2) I_a \\ &= 2\frac{p}{\pi} m_1 N_{ph} k_{w1} \phi_p I_a \end{aligned} \tag{4.15}$$

The RMS torque for both sinusoidal current and sinusoidal magnetic flux density, i.e., the fundamental torque component, is obtained by multiplying eqn (4.15) by $\pi\sqrt{2}/4$, that is,

$$\left.\begin{aligned} T_d &= \frac{m_1}{\sqrt{2}} p N_{ph} k_{w1} \phi_p I_a = k_T I_a \\ k_T &= \frac{m_1}{\sqrt{2}} p N_{ph} k_{w1} \phi_p, \text{ is the torque constant} \end{aligned}\right\} \tag{4.16}$$

The back-EMF can be obtained by differentiating the fundamental flux, $\phi_{p1} = \phi_p \sin\omega t$ and multiplying it by $N_{ph}k_{w1}$, i.e. $e_f = 2\pi f N_{ph} k_{w1} \phi_p \cos\omega t$. The RMS value is obtained by dividing the peak value by $\sqrt{2}$ giving

$$\left.\begin{aligned} E_f &= \pi\sqrt{2}\, f N_{ph} k_{w1} \phi_p = \pi\sqrt{2}\, p N_{ph} k_{w1} \phi_p n_s = k_E n_s \\ k_E &= \pi\sqrt{2}\, p N_{ph} k_{w1} \phi_p, \text{ is the EMF/armature constant} \end{aligned}\right\} \quad (4.17)$$

where n_s is shaft speed in revs/sec. Equation (4.17) can be obtained from eqn (4.16) from the relation $T_d = m_1 E_f I_a / (2\omega n_s)$.

4.3.3 Pulsating Torque

Torque in a PM machine can be split into the following components:

1. Cogging torque: pulsating torque due to the variation of the airgap reluctance or due to variation of energy in the airgap. Cogging torque is due to slotting and it is not dependent on current excitation.
2. Ripple torque: pulsating torque produced by stator and rotor (PM) MMFs.
3. Pulsating torque: sum of cogging and ripple torques.
4. Total torque: sum of the average torque and pulsating torque.

Torque pulsations are as a result of cogging torque, harmonics due to back-EMF and current, airgap flux density and induction by the electronic controllers and saturation of the magnetic circuit [28], [32]. Ripple torque is dependent on the motor structure and armature current [25], [29]. Cogging torque is solely dependent on the interaction of the magnets and the stator iron. Cogging torque can be obtained by estimating the energy change in the airgap as the rotor rotates. The energy change in the PMs and iron is minimal compared to that of air. It is therefore given as [29], [30]

$$T_{cog}(\theta) \approx -\frac{\partial W_{airgap}(\theta)}{\partial \theta} = -\frac{1}{2}\phi_g^2 \frac{dR}{d\theta} \quad (4.18)$$

where $W_{airgap}(\theta)$ is energy within the airgap, θ is rotor angle and R is the airgap reluctance. Equation (4.18) can be expressed in component form for a symmetric RFPM as [30]

$$T_{cog}(\theta) = \frac{L_e \pi}{4\mu_o}\left(R_2^2 - R_1^2\right) \cdot \sum_{n=0}^{\infty} n N_L G_{N_L} B_{N_L} \sin\left(n N_L \theta\right) \quad (4.19)$$

where R_1 and R_2 are the stator and PM radii respectively for an internal rotor machine. For an external rotor, the counter holds. N_L is the LCM of the number of poles and the number of slots and G_{NL} and B_{NL} are the cosine Fourier transform coefficients. Equation (4.19) can be adopted to fit an AFPM by substituting the airgap volume. N_L gives the cogging frequency, while G_{NL} and B_{NL} determine its magnitude. These parameters can be used to explain the different methods of mitigating cogging torque. For instance, teeth pairing, interpole design and teeth notching reduce G_{NL}, while magnet shaping and pole-arc design reduce B_{NL}. Increasing the cogging frequency, N_L by the proper selection of the pole-slot combination reduces both G_{NL} and B_{NL} [30]. In integral slot machines, the number of slots per pole is an integer. Hence each rotor pole has the same position relative to the stator resulting to high cogging torque. This is because the cogging torque components from the magnets are in phase. In fractional slot machines, the components are out of phase, cancelling each other giving a reduced resultant cogging torque [28]. Therefore, asymmetric windings with a difference of one between the pole and the slot numbers give a high cogging frequency which reduces cogging torque.

Techniques for minimizing cogging torque include: varying the PM pole shape, skewing of stator teeth and/or rotor PMs, magnet or pole shifting, alternating the PM pole-arc ratio, optimizing the pole-slot combination, teeth-pairing, dummy slots, varying the radial shoe depth, control strategy and graded airgaps [28], [29], [30], [32]. Most of these methods are elaborated in [28]. The selection of any particular method is important since it can increase the production cost and also complicate the manufacturing process. The effect of the selected strategy on the performance machine should also be considered.

4.4 *PM Machine Windings*

Conventional concentrated windings have the number of slots/pole/phase, q as unity. They have more harmonics and poor stator utilization and large slots than distributed windings. Distributed windings have a $q > 1$ [65]. The interpretation of windings in PM machines differs slightly from conventional windings. In PM machines, when q is greater or equal to 1, it results in distributed windings which can be either integral (q an integer) or fractional (q is a fraction) windings. If q is less than unity, it results in concentrated windings [66]. Concentrated windings are well suited for high torque machines with a square-wave flux density, but at an increased amount of harmonic content and ripple torque. A distributed non-skewed winding with $q = 1$, has a higher ripple torque than a concentrated winding [31]. Leakage inductance is higher in concentrated windings than in distributed windings. This results in higher core losses and a need for a higher inverter rating, but a lower field weakening current in the constant power region [31], [67]. Distributed windings have higher copper losses than concentrated

windings due to their longer end windings, followed by single-layer windings, with double-layer windings having the least.

Windings can also be overlapping or non-overlapping. Fractional-slot-overlapping windings have their phase coils distributed over a number of slots excluding one. Non-overlapping windings are always fractional [68]. Non-overlapping windings have shorter end turns than overlapping windings. Tooth-concentrated non-overlapping coils can form concentrated or distributed phase groups as shown in Fig 4.9(b) and (c) respectively. In addition, they have a simple structure and can be manufactured in modules. This allows them to have high slot-fill factors and the coil production process can be easily automated [67].

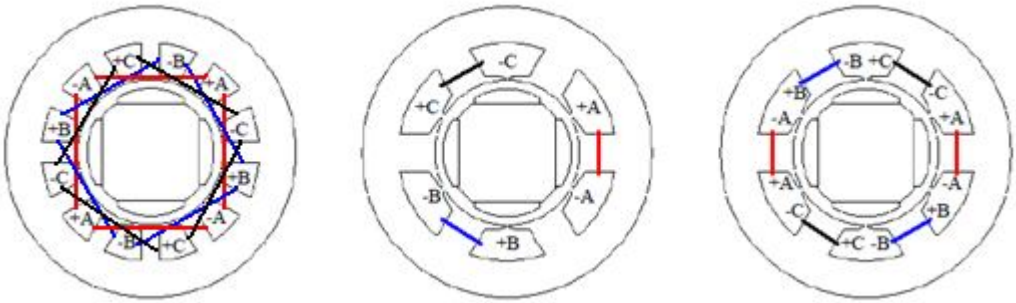

(a) Distributed-overlapping windings **(b) Single-layer windings** **(c) Double-layer windings**

Fig 4.9 Winding layouts for a 4-pole RFPM

Concentrated windings can also be single-layer or double-layer windings. In the former, the teeth are alternately wound while in the latter they all wound. A single-layer winding has an even number of slots. It also allows the improvement of the winding factor by varying the width of the unwound tooth. The coil-pitch is equal to the slot-pitch in a single-layer winding, but it is slightly less in a double-layer winding. Double layer windings have a more sinusoidal back-EMF than single-layer windings which may even have sub-harmonics [31], [67].

4.4.1 Three-Phase Winding Distribution in Slots

A single-layer winding has one coil-side of a turn per slot. Hence, the number of coils is $Q_s/2$ and the number of coils per phase is $n_c = Q_s/(2m_1)$, where Q_s is the number of slots. A double-layer winding has two coil-sides for turns belonging to two different coils in adjacent teeth. The number of coils is therefore Q_s and the number of coils per phase is $n_c = Q_s/m_1$.

The number of slots per pole is $Q = Q_s/(2p)$, while the number of slots per pole per phase is $q = Q_s/(2pm_1)$ for both single and double layer windings. The number of conductors per coil for single and double-layer windings is given as $N_c = a_p a_w N_{ph}/(pq)$ and $N_c = a_p a_w N_{ph}/(2pq)$ respectively [24]. a_p is the number of current paths for a parallel connected stator and a_w is the number of strands per conductor. The number of conductors per slot is the same for both cases, i.e. $N_{sl} = a_p a_w N_{ph}/(pq)$. For a full pitch-coil, the coil-pitch $y = Q$ while for a short pitched coil, it is $y = \frac{w_c(r)}{\tau(r)} \times Q$ where $w_c(r)$ and $\tau_p(r)$ are the coil-pitch and the pole-pitch measured at a radius r. The ratio of coil-pitch to pole-pitch is $\beta = w_c(r)/\tau_p(r)$, hence $y = \beta Q$.

4.4.2 Winding Factor and EMF Harmonics

Distributing and short-pitching or chording of coils decreases the fundamental winding factor. A concentrated winding with the same coil-pitch and pole-pitch has a unity fundamental distribution factor. For this type of winding, the induced EMF per coil can be added algebraically to obtain the induced EMF per phase. In a distributed winding, the induced EMF in different coils has different phases; hence it has to be summed vectorially. By selecting an optimum number of slots for a given number of poles, a high fundamental winding factor can be achieved as derived in [31], [66] and [67]. An optimum winding factor is obtained when $= 1/ _1$ [66].

The winding factor, k_{wn} is the product of the distribution factor, k_{dn}, pitch or slot factor, k_{pn} and the skew factor, k_{skew}, i.e. $k_{wn} = k_{dn} \cdot k_{pn} \cdot k_{skew}$. These factors can be expressed as [66], [67]

$$\left.\begin{aligned} k_{dn} &= \frac{\sin(n\pi/2m_1)}{a\sin[n\pi/(2m_1 a)]} \\ k_{pn} &= \cos\left(\frac{1}{2}n\varepsilon\right) \\ k_{skew} &= \frac{\sin(nz\pi p/(Q_s))}{[nz\pi p/(Q_s)]} \end{aligned}\right\} \qquad (4.20)$$

where $a = Q_c/\gcd(Q_c, (2p \cdot m_1))$ with Q_c being the number of coils. $Q_c = Q_s$ for all teeth wound and $Q_s/2$ for alternate teeth wound. $\varepsilon = \pi - \gamma_s$ is the chording or the coil-span angle and $\gamma_s = 2p\pi/Q_s = \pi/(qm_1)$ is the slot-pitch angle in electrical degrees. A stator can be skewed with

one slot pitch, *z* to reduce cogging torque but at a reduced winding factor and EMF. This increases the copper losses and it also complicates the manufacture of the stator. Stator skewing is therefore rarely done especially in concentrated windings where *q* is less than one. Magnet skewing is therefore preferred [67]. Fig 4.10 shows the effect of k_{p1} and k_{d1} on k_{w1} for a 10 pole-12 slot machine. From the relation in eqn (4.20), k_{d1} is a constant (= 0.9659), since it is dependent on fixed parameters. k_{p1} is determined by *p* and Q_s as discussed previously. The feasible region for *q*, for $k_{w1} > 0.9$ is between 0.3 and 0.4. By optimizing the selection of *p* and Q_s, a high k_{w1} can be realized but the effect on cogging torque for slotted stators should also be considered.

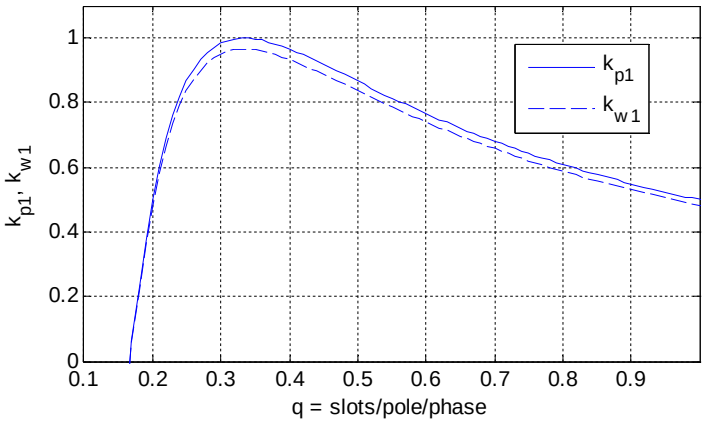

Fig 4.10 k_{p1} and k_{w1} vs. *q* for Q_s = 12 slots, *p* = 5 pole pairs and m_1 = 3 phase

Space harmonics are due to the spatial distribution of the airgap flux density which induces time EMF harmonics. These harmonics can be lowered by optimising the shape of the magnet, the pole-arc ratio (pole angle) and the pole-slot combination. The induced EMF per phase for an *n*th harmonic flux is [65]

$$E_n = 4.44(nf)N_{ph}\phi_n k_{wn} \tag{4.21}$$

where ϕ_n is the flux per pole corresponding to the *n*th harmonic flux density via the relation $\phi_n = A_n B_{gn}$. A_n is the *n*th harmonic pole area and $B_{n(ave)}$ is the average flux density of the *n*th harmonic which are given as

$$\left.\begin{aligned} A_n &= \frac{\pi}{4}\frac{\left(D_o^2 - D_i^2\right)}{n}\cdot\frac{1}{(2p)} = \frac{\pi}{n8p}D_o^2\left(1-k_d^2\right) \\ B_{n(ave)} &= \alpha_i B_{n(mg)} \\ \phi_n &= \alpha_i B_{n(mg)}\cdot\frac{\pi}{n8p}D_o^2\left(1-k_d^2\right) \end{aligned}\right\} \tag{4.22}$$

where $B_{n(mg)}$ is the amplitude/plateau value of the nth harmonic flux density wave. Equation (4.21) can be written as $E_n = KB_{n(mg)}k_{wn}$, where $K = 4.44\,fN_{ph}\alpha_i\left(1-k_d^2\right)D_o^2\,\pi/(8p)$ is a constant. Therefore, winding factors can be used to capture the influence of a given pole-slot configuration on harmonics, while the effect of shape and strength of PMs can be captured by the flux density harmonics. It is also important to note that asymmetric windings present many more harmonics than symmetric windings. This leads to pulsating magnetic fields in the rotor iron which causes eddy currents in the poles and iron losses in the rotor iron [31].

4.4.3 Pole-Slot Combinations for Concentrated PM Windings

The following are general design rules for pole-slot combinations for concentrated windings [66]:

1. The number of poles must be even.
2. The number of poles cannot be equal to the number of slots, since this would worsen cogging.
3. The number of slots must be a multiple of the number of phases.
4. The number of pole pairs, p in a section F $(=\gcd(Q_s, p))$ cannot be a multiple of the phase number since it would lead to unbalanced windings.

These rules gives the possible number of slots as 3, 6, 9, 12,....3x for double layer windings and 6, 12, 18, 24,….6x for single layer windings, where x is an integer.

4.4.4 Synchronous Reactance

Synchronous reactance, X_s is the sum of the armature reaction or mutual reactance, X_a and stator winding leakage reactance, X_1. For surface mounted PM machines, the d and q axes reactances are equal. The armature reaction reactance is due to armature excitation. It can be expressed as [24]

$$X_a = 2m_1\mu_o f\left(\frac{N_{ph}k_{w1}}{p}\right)^2\left(\frac{R_o^2 - R_i^2}{g'}\right) \tag{4.23}$$

where $g' \approx 2(g + l_m)$ for a twin rotor-inner stator AFPM topology. g is the single-sided mechanical clearance and l_m is the magnet depth.

Stator leakage reactance is the sum of the slot leakage reactance, X_{1s}, the end winding leakage reactance, X_{1e} and the differential reactance, X_{1d} for higher harmonics, i.e. [24],

$$\left.\begin{aligned} X_1 &= X_{1s} + X_{1e} + X_{1d} \\ X_1 &= 4\pi f \mu_o \frac{L_e N_{ph}^2}{pq}\left(\lambda_{1s} k_{1X} + \frac{l_{in}}{L_e}\lambda_{1ein} + \frac{l_{out}}{L_e}\lambda_{1eout} + \lambda_{1d}\right) \end{aligned}\right\} \tag{4.24}$$

where k_{1X} is the skin-effect coefficient for leakage reactance, l_{in} is the length of the inner end windings, l_{out} is the length of the outer end windings, λ_{1s} is the coefficient of slot leakage permeance, λ_{1ein} is the coefficient of the leakage permeance of the inner end connection, λ_{1eout} is the coefficient of the leakage permeance of the outer end connection and λ_{1d} is the coefficient of the differential leakage. Tapered semi-open slots can be assumed to rectangular as shown in Fig 4.11. Therefore, λ_{1s} is given as a function of slot dimensions as

$$\lambda_{1s} = \frac{h_{11}}{3w_s} + \frac{h_{12}}{w_s} + \frac{h_{13}}{w_o} \ . \tag{4.25}$$

This is for a single-layer winding. For a double-layer winding, eqn (4.25) is multiplied by a factor of $(3\beta+1)/4$. Such approach is justified if $\beta = w_c(r)/\tau_p(r)$ is in the range of 2/3 to 1.

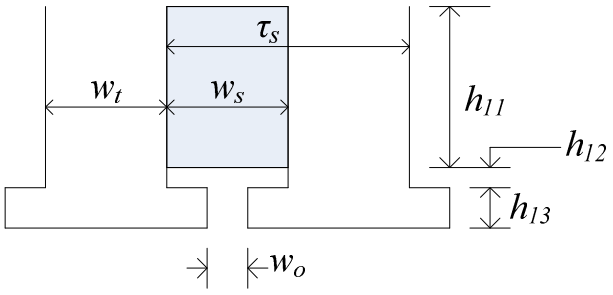

Fig 4.11 Tooth and slot dimensions; slot-width, w_s; tooth-width, w_t; slot-pitch, τ_s

The leakage permeance coefficient for the inner and outer end windings for a double-layer winding for low-voltage small and medium power machines can be expressed as,

$$\left.\begin{aligned} \lambda_{1ein} &\approx 0.17q\left(1 - \frac{2w_{cin}}{\pi \cdot l_{in}}\right) \\ \lambda_{1eout} &\approx 0.17q\left(1 - \frac{2w_{cout}}{\pi \cdot l_{out}}\right) \end{aligned}\right\} \tag{4.26}$$

where w_{cin} and w_{cout} are the inner and the outer coil spans respectively. Finally λ_{1d} can be given as

$$\left.\begin{aligned}\lambda_{1d} &= \frac{m_1 q \tau \cdot k_{w1}^2}{\pi g' k_{sat}} \tau_{d1} \\ \tau_{d1} &= \frac{\pi^2 \left(10q^2 + 2\right)}{27} \sin\left(\frac{30^2}{q}\right) - 1\end{aligned}\right\} \tag{4.27}$$

where $k_{sat} \geq 1$ caters for the saturation of the magnetic circuit. The specific permeance coefficient, $\lambda_{1t} \approx \frac{5g/w_o}{5 + 4q/w_o}$ between the heads of the teeth should be added to λ_{1d} for slotted stator windings.

4.5 *Losses and Efficiency*

Stator winding losses, core losses and rotational losses are reviewed in this section from reference [24]. The reference also models eddy current losses in slotless and coreless stators, losses in permanent magnets, rotor core losses and losses due to nonsinusoidal currents. For low speed machines, copper losses are the most dominant [69]. This is because other losses are mainly dependent on the operating frequency and rotational speed.

4.5.1 Stator Winding Losses

The stator resistance per phase is $R_{1dc} = N_{ph} l_{ave} \big/ a_p a_w \sigma A_{cond}$ for a DC current when temperature effects are assumed. l_{ave} (= $2L_e + l_{in} + l_{out}$) is the average length per turn, σ is the conductivity and A_{cond} is the cross-sectional area of the conductor. For AC current and distributed windings, the resistance is due to the radial portions of the conductors, R_b and end connections R_e, that is,

$$R_{ac} = R_b + R_e = \frac{N_1}{a_p \sigma A_{cond}} \left(2L_e k_{1R} + l_{in} + l_{out}\right) \approx k_{1R} R_{dc} \tag{4.28}$$

where k_{1R} is the skin-effect coefficient which is given in [24]. $R_{ac} \approx R_{dc}$ for small motors with round conductors operating at 50 or 60 Hz. The power loss due to armature winding losses is therefore,

$$\Delta P_{Cu} = m_1 I_a^2 R_{ac} \approx m_1 I_q^2 R_{dc} k_{1R} \tag{4.29}$$

4.5.2 Stator Core Losses

Stator core losses are due to non-sinusoidal magnetic flux, hysteresis losses, switching or rectification effects on the current which results in harmonics and eddy current losses induced on laminations. These losses can be segregated as done in [24] into eddy current and hysteresis losses. They can also be combined if the specific core losses are known. This is given as [24], [69]

$$\Delta P_{Fe} = \Delta p_{1/50}\left(\frac{f}{50}\right)^{4/3}\left[k_{adt}B_t^2 m_t + k_{ady}B_y^2 m_y\right] \tag{4.30}$$

where k_{adt} = 1.7 to 2.0 and k_{ady} = 2.4 to 4.0, m_y is the mass of the yoke and m_t is the mass of the teeth, $\Delta p_{1/50}$ is the specific core loss in W/kg at 1T and 50Hz, B_t is the maximum magnetic flux density in a tooth and B_y is the magnetic flux density in the yoke.

4.5.3 Rotational Losses

Rotational or mechanical losses, ΔP_{rot} consist of friction losses in bearings, ΔP_{fr}, windage losses, ΔP_{wind} and ventilation losses, ΔP_{vent} due to forced cooling, that is,

$$\Delta P_{rot} = \Delta P_{fr} + \Delta P_{wind} + \Delta P_{vent} \tag{4.31}$$

For small machines the frictional loss in bearings can be expressed as

$$\Delta P_{fr} = 0.06k_{fb}\left(m_r + m_{sh}\right)n_s \tag{4.32}$$

with k_{fb} = 1-3 m^2/s^2, m_r is the mass of the rotor in kg, m_{sh} is the mass of the shaft in kg and n_s is the speed in revs/sec. Windage losses can be expressed as

$$\left.\begin{aligned}\Delta P_{wind} &= \frac{1}{2}c_f\rho\left(2\pi n_s\right)^3\left(R_o^5 - R_{sh}^5\right)\\ c_f &= \frac{3.87}{\sqrt{\mathrm{Re}}} \quad \text{and} \quad \mathrm{Re} = \rho\frac{R_o v}{\mu} = \frac{2\pi n_s \rho R_o^2}{\mu}\end{aligned}\right\} \tag{4.33}$$

where ρ is the specific density of the cooling medium, c_f is the coefficient of drag for turbulent flow, R_e is the Reynolds number for a rotating disc whose outer radius is R_o, $v = v_x = 2\pi R_o n_s$ is the linear velocity at the outer radius, R_{sh} is the shaft radius and μ is the dynamic viscosity of the fluid which is 1.8×10^{-5} Pa s at 1 atms and 20˚C if the machine is air cooled. If the machine is designed without a cooling fan which is usually the case, then $\Delta P_{vent} = 0$ and $\Delta P_{rot} = \Delta P_{F\&W}$.

4.5.4 Efficiency

Efficiency, η of a generator is the ratio of the output electrical power, P_{out} over the input shaft power, P_{in}. The power input is the sum of the power output and the total power loss, that is, $P_{in} = P_{out} + \Delta P$.

$$\eta = \frac{P_{out}}{P_{in}} = \frac{P_{out}}{P_{out} + \Delta P} \tag{4.34}$$

where $\Delta P = \Delta P_{Cu} + \Delta P_{Fe} + \Delta P_{rot}$. Stray load losses are additional iron losses. They are due to permeance-variation-induced high-frequency losses in the ferromagnetic cores of AC machines and other anomalous electromagnetic losses. They are difficult to calculate accurately hence they are approximated according to [69] as $\Delta P_{stray} = k_{stray} P_{out}$. The stray load coefficient, k_{stray} is given as,

$$k_{stray} = \begin{cases} 0.03 - 0.05; & \leq 10kW \\ 0.005 - 0.01; & \leq 100kW \\ 0.003 - 0.005; \text{for large } machines \end{cases}$$

4.6 *Sizing Equations for Diameters, Current Loading, Magnet Depth, Rotor Back Iron Thickness and Power Density*

Traditionally rotating machines are sized from the relation $D_g^2 L_e$, where D_g is the airgap surface diameter and L_e is the effective stack length [63]. In [63], an equation that substitutes D_g with the outer diameter of the machine D_o is derived. The generator power, P_{gen} equation is obtained by neglecting leakage inductance, armature reaction effects and stator resistance. Furthermore, saturation of the magnetic circuit is neglected especially in coreless machines and the airgap is assumed to be uniform. Therefore, D_o can be expressed as function of P_{gen} as [63], [70], [71]

$$\left.\begin{aligned} P_{gen} &= \frac{\pi^2}{2}\cdot 0.881\cdot \eta B_g A_s \frac{f}{p}\left(1-k_d^2\right)\frac{1+k_d}{2} D_o^3 \\ D_o &= \sqrt[3]{\frac{P_{gen}}{\frac{\pi^2}{2}\cdot 0.881\cdot \eta B_g A_s \frac{f}{p}\left(1-k_d^2\right)\frac{1+k_d}{2}}} \end{aligned}\right\} \tag{4.35}$$

The product $D_g^2 L_e$ can be expressed in terms of k_d as [62]

$$D_g^2 L_e = \frac{1}{8}\left(1+k_d\right)\left(1-k_d^2\right)D_o^2 = K_D D_o^3 \tag{4.36}$$

D_o for a double airgap machine can also be given as [24]

$$D_o = \sqrt[3]{\frac{\varepsilon \cdot P_{gen}}{\pi^2 k_{W1} K_D n_s . A_s . B_{1\max}\cdot \cos\phi}} \tag{4.37}$$

For a single-airgap machine, eqn (4.37) is multiplied by $\sqrt[3]{2}$. Equation (4.37) considers voltage regulation, $\varepsilon = E_f / V_{an}$ which is neglected in eqn (4.35). The inverse of this factor, falls within a range of 0.7-0.8 for a small machine supplying a purely resistive load [72], n_s is the speed in rev/sec which falls within $20/6 - 80/6$ revs/sec giving 10-18 pole pairs [72], A_s and $B_{1\max}$ are the specific electrical loading and specific magnetic loading respectively. A_s is in the range of 10,000-40,000A/m for small PM machines [62]. The specific magnetic loading is the peak value of the fundamental airgap flux density. The machine efficiency, η is within 80-95% [26], [62] for small to medium power

ratings, the frequency, f is in the range of 10-80Hz [62], [72]. The electrical loading for a double rotor-inner stator AFPM machine is given as [24]

$$A_s = \frac{2\sqrt{2}m_1 N_{ph} I_a}{\pi D_g} = \frac{4\sqrt{2}m_1 N_{ph} I_a}{\pi D_o (1+k_d)} \tag{4.38}$$

The axial length of the machine is $L_{stk} = L_{cs} + 2L_r + 2g$, where L_{cs} is the axial length of the stator when end winding protrusions are neglected. It is expressed as [63], [70], [71]

$$\left.\begin{aligned} L_{cs} &= \frac{B_{mg}\pi D_o (1+k_d)}{B_{cs} 4p} \\ B_{cs} &= \begin{cases} 5.47 f^{-0.32} & f > 40Hz \\ 1.7 - 1.8T & f \le 40Hz \text{ for AFTPM} \end{cases} \end{aligned}\right\} \tag{4.39}$$

The axial depth of the rotor is $L_r = L_{cr} + l_m$, where L_{cr} is the axial depth of the rotor disc and l_m is the axial depth of the permanent magnets

$$\left.\begin{aligned} L_{cr} &= \frac{B_{mg}\pi D_o (1+k_d)}{B_{cr} 8p} \\ B_{cr} &= 1.6 \text{ to } 1.8T \end{aligned}\right\} \tag{4.40}$$

B_{cs} and B_{cr} are the flux densities in the stator core and rotor cores respectively. The length of the magnet is expressed as [62]

$$l_m = (PC - p_{rl}\mu_{rec}) C_\phi k_C g \tag{4.41}$$

where PC is the permeance coefficient, p_{rl} is the normalized rotor leakage permeance in the range of 0.05-0.2, k_C is the Carter's coefficient and $C_\phi = A_{pm} / A_p$ is the flux focusing factor which is a ratio of the pole area, A_{pm} to the pole-pitch area, A_p.

The power density, ξ of an axial-flux machine can be expressed as

$$\xi = \frac{P_{gen}}{\frac{\pi}{4} D_o^2 L_{stk}} \tag{4.42}$$

Protrusion of the end windings are neglected in eqn (4.42).

4.7 *Conclusions*

Different generator topologies were discussed and the various parameters governing an AFPM generator were modelled analytically. Equations governing the physical size of the generator, that is diameters, effective stack length, rotor sizes and power density were also reviewed. These will be used in the analytical design and estimation of generator performance parameters in the next chapter. These parameters will then be verified and analysed using finite element analysis (FEA).

5 Design and Analysis of an Axial-Flux Generator

This Chapter focuses on machine design and analysis. In design, the procedure for determining machine parameters is discussed. These parameters include: the number of poles and slots, the phase voltage and current, magnet grade and slot and tooth geometry. Analysis involves the use of FEA in determining the flux density distribution to ensure there is no saturation of the magnetic circuit, analysis of the back-EMF, comparing cogging torque minimizing techniques and analysing the effect of the pole-arc on torque ripple in motor mode. Cogging torque minimization techniques which will be considered are optimising the pole-arc ratio, teeth-notching and skewing of magnets. The effect of these methods on the performance of the machine will be considered at a rated load current of 10A at 600rpm. A method of simulating an AFPM machine as an equivalent RFPM machine will also be presented. This method will be used in 2D-FEA analysis of all the machine topologies. It is verified by comparing its results with that of the conventional method where the AFPM is analysed like a linear machine. The performance of the proposed machine which has parallel-teeth and trapezoidal poles is compared with one with trapezoidal-teeth and trapezoidal-poles.

5.1 *Machine Design*

The practical operating electrolyser cell voltage for a self-heating electrolyser falls within 2-2.2V [11]. Taking the mean gives an electrolyser rating of $1.25kW \approx 2.1V \times 11cells \times 55A$. This rating is assumed to ensure self-starting of the electrolyser. The generator rating is then obtained as 1.42kW which can be approximated to 1.5kW. The maximum mechanical power, $P_{m(\max)}$ and electrolyser power, P_{ely} are obtained from Fig 5.1 as 1.875kW and 1.323kW respectively.

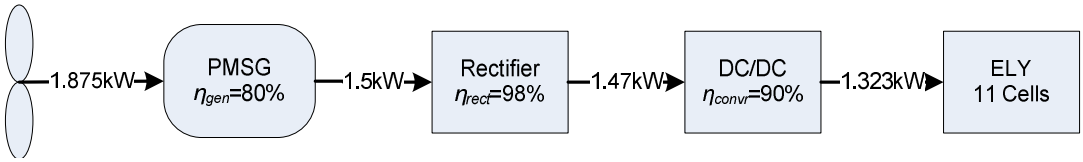

Fig 5.1The power flow diagram for a WECS-ELY system

5.1.1 Number of Poles and Slots

The number of pole-pairs is given by the TSR expression as $p = 2\pi fR/(v_m \lambda)$. Setting *TSR* = 7 and f = 50Hz and v_m = 8m/s, gives a radius, R of 2.2m and 24 poles with a shaft speed of 243rpm. From Table C.2 of Appendix C, the highest winding factor for 24 poles and 27 slots combination is 0.945

with an LCM of 216 for $q = 3/8$. This value of q exacerbates cogging [31]. Therefore an alternative of 22 poles is considered. It is important to note the following in the selection of the number of slots [31], [67].

1. Asymmetrical windings (Q_s odd) present many more harmonics which contribute to ripple torque significantly by re-introducing even number harmonics than symmetrical (Q_s even) windings, but at a reduced cogging torque.

2. An odd number of slots results in asymmetrical windings which leads to unbalanced magnetic forces which results in noise and vibrations. Symmetrical windings however, have their magnetic forces evenly distributed. For an asymmetrical winding layout, the whole machine is modelled in finite element analysis (FEA) while in symmetrical windings only a section is modelled. The number of sections is given as $F = \gcd(Q_s, p)$ [66].

3. Cogging torque is minimised if the slot and pole number have their least common multiple (LCM (Q_s,2p)) as a large value. The LCM gives the number of cogging periods per revolution. A higher cogging frequency lowers the cogging amplitude. Windings with q = 2/5 and 3/8 have a lower LCM and present a higher cogging torque, but with a lower torque ripple.

4. $q < 1/2 = a/b$ for non-overlapping tooth-concentrated fractional windings where a and b have no common divisor and b should not be a multiple of the number of phases, m_1.

Using 22 poles, the frequency is obtained as 46Hz with the other factors held constant. This can be extended to various stages for an AFPM as shown in Table 5.1, where the radius is for an individual stage. It is evident that the options give fractional-slot combinations (Q_s/(2p) = fraction); insuring that fewer pole-edges line up with the slots [61].

Table 5.1 Comparison of various pole-slot configurations

Stages	Q_s	2p	Q_s/(2p)	q	k_{w1}	f (Hz)	v_m (m/s)	R (m)	LCM (Q_s,2p)
1	27	24	9/8	3/8	0.945	50	8	2.2	216
1	18	22	9/11	3/11	0.902	46	8	2.2	198
1	21	22	21/22	7/22	0.953	46	8	2.2	462
1	24	22	12/11	4/11	0.950	46	8	2.2	264
2	15	16	15/16	5/16	0.951	46	8	1.6	240
3	15	14	15/14	5/14	0.951	46	8	1.3	210
4	9	12	3/4	1/4	0.866	46	8	1.1	36
4	18	12	3/2	1/2	0.866	46	8	1.1	36
4	*12*	*10*	*6/5*	*2/5*	*0.933*	*46-50*	*8.5*	*1.0*	*60*

According to [27], ripple torque is minimized if $q \approx 1/3$, that is, when the number of poles is close to the number of slots. It is also important to note that even number of slots give low LCM which leads to lining up of teeth and poles; hence high cogging torque. 21 slots are therefore selected since they give a higher winding factor, a relatively low ripple torque and a high LCM. A high LCM gives a very small mechanical angle per cogging cycle which is difficult to measure. Therefore the machine was decomposed to a 375W 4-stage machine, where a single-stage would be prototyped and analysed. The topology was designed to have a low LCM as shown in the italicised last row of Table 5.1. A double-layer winding layout for the 10pole-12slot combination is obtained from Table C.3 of Appendix C as A|A'A'|AB'|BB|B'C|C'C'|CA'|AA|A'B|B'B'|BC'|CC|C'.

5.1.2 Phase Voltage and Phase Current

The electrolyser power is obtained from the generator rating of $375W = 1.5kW/(4\,stages)$ as $P_{ely(\max)} = P_{gen(\max)} \cdot \eta_{rect} \cdot \eta_{conv} = 330.75W$. To maintain the same operating conditions as the earlier characterized PEM electrolyser, the stack current is held constant at 55A. The stack is reduced to three cells, with a stack voltage, U_{ely} of 6V ($\approx 2.1V \times 3cells$). The generator phase current, $I_{s(rms)}$ and phase voltage, V_{an} can then be expressed as functions of electrolyser parameters by manipulating rectifier and buck-boost equations from [58] as

$$\left.\begin{aligned} I_{s(rms)} &= 0.816\left(\frac{D}{1-D}\right)\frac{I_{ely}}{\eta_{conv}\eta_{rect}} \\ V_{an} &= \frac{\pi}{3\sqrt{6}}\left(\frac{1-D}{D}\right)\frac{U_{ely}}{\eta_{conv}\eta_{rect}} \end{aligned}\right\} \qquad (5.1)$$

To lower losses and armature conductor size the phase current is set to 10A, giving a duty ratio, D of 16.42% ≈ 17%. The phase voltage is obtained as 14V and the line-to-line voltage as 24V.

5.1.3 Magnet Grade

A choice for the grade of the magnets depends on whether the stator is coreless or cored. In coreless topologies, the magnets must have a high remanence in order to establish the necessary airgap flux, while in a cored design the saturation of the teeth limits the flux density - to keep iron losses low. The grade of the magnet gives the remanent flux density, B_r. The plateau value of the airgap flux density in a coreless design is given by $B_{mg} = 0.8B_r$. This is sufficient for a coreless stator but in a cored

design, the saturation of the stator yoke/core, B_{cs} (1.5-1.8T) determines the magnetic loading of the machine. For a cored topology, $B_{mg} < \left(1 - \frac{w_s}{\tau_s}\right) K_s B_{cs}$, where w_s is the slot-width, τ_s is the slot-pitch and K_s is the stacking factor in the range of 0.95-0.98. The peak value of the fundamental space harmonic of the airgap which is also called the specific magnetic loading is then obtained as [62]

$$\left.\begin{aligned} B_{1\max} &= k_f B_{mg} \\ k_f &= \frac{4}{\pi}\sin\left(\alpha_i \frac{\pi}{2}\right) \end{aligned}\right\} \qquad (5.2)$$

where k_f is the form of excitation field for a single smooth PM. The average flux density, B_{ave} or the air gap flux density, B_g is then given as $B_g = \alpha_i B_{mg}$. The flux per pole and the back-EMF can then be obtained. It is important to note that for a reduced ripple torque due to the interaction of the MMFs of the PMs and armature current, the optimum pole arc ratio, α_i is 0.81 [25], [70]. While according to [62], 0.67 minimizes cogging torque. Thus, 0.80 is selected to reduce ripple torque since cogging toque is to be mitigated. Letting $w_s/\tau_s = 0.5$ and K_s = 0.95 and B_{cs} = 1.5T B_{mg} is obtained as 0.7125T and B_g as 0.57T. The latter value should be greater than the critical airgap flux density, $B_{crit} = 0.5B_r$. The grade must ensure $B_g > B_{crit}$. Grade 33 NdFeB whose B_r falls within 1.13-1.17T is selected. Its B_r temperature coefficient is -0.11% per °C. At an operating temperature of 80°C, B_r falls to a range of 1.06-1.09T. The temperature effect is assumed to be negligible, though B_g is slightly less than B_{crit} in this condition. Having the minimum possible grade ensures the contribution of magnets to cogging torque is minimum since it is proportional to the square of B_g, as expressed in eqn (4.18).

5.1.4 Tooth and slot widths

For this particular topology, parallel-teeth are considered due to their ease in manufacturing. They allow modular assembly and maintenance of the stator and they inherently reduce cogging torque. This type of stator has an inherent design flaw. If the lamination length is excessive in the axial direction, the effective flux component decreases with an increasing leakage component. Thus the aspect ratio coefficient $K_L = D_o/L_{stk}$ should be within 2-7.14 [62].

The average slot-pitch is given as $\tau_s = \pi D_g / Q_s$ while the slot-width, w_s is expressed as $w_s = h\tau_s$ where h is between $0.5 \le h \le 0.6$. The sum of the tooth-width and slot-width is equal to the slot-pitch, i.e. $\tau_s = w_t + w_s$ as shown in Fig 4.11. Therefore, the tooth-width can be expressed as a function of h as $w_t = \tau_s(1-h)$.

Parallel-teeth have a constant tooth-width with respect to the radius. Therefore the slot-width varies with radius giving trapezoidal/tapered slots. The maximum tooth-width is set by the inner diameter and is expressed as $w_{t-in(\max)} = \dfrac{\tau_{s-Di} \cdot B_{mg}}{K_s \cdot B_{cs}}$, where $\tau_{s\text{-}Di}$ is the slot-pitch at the inner radius. The fundamental flux density at any radius in a tooth can be expressed as $B_{1t} = B_{mg} \cdot \tau_s(r) / w_{s-Di}(r)$ [24]. Therefore, the tooth flux density is highest at D_i, where the teeth have a reduced proximity.

The maximum tooth-tip width is obtained by setting an allowance at the inner diameter, i.e., slot opening, w_o which allows for the assembly of the teeth into the stator. w_o is then deducted from the inner diameter slot pitch, i.e. $w_{tip} = \tau_{s-Di} - w_o$. The tooth-tip width like the tooth-width is constant for all diameters.

The area of the slot is given as [24]

$$\left.\begin{aligned} A_{slot} &= \frac{N_c A_{cond}}{k_{sf}} = \frac{\text{No. of cond./slot} \times \text{Area of each cond.}}{\text{Slot - fill fator}} \\ A_{cond} &= \frac{I_a}{a_w J_s} = \frac{\pi D_{cond}^2}{4} \text{ and } N_c = \frac{a_p a_w N_{ph}}{2pq} \end{aligned}\right\} \qquad (5.3)$$

where N_c is the number of conductors per coil for a double-layer winding, a_p is the number of parallel current paths, a_w is the number of parallel conductors and $I_a = I_{s(rms)} / a_p$ is the armature current per stator. The approximate slot-depth can be computed by dividing the slot area by the minimum slot-width at the inner diameter, D_i.

The number of turns in series per phase, N_{ph} is obtained from the EMF equation. Dividing N_{ph} with the number of coils per phase for a double-layer winding, gives the number of turns per tooth, N_t. The current loading, A_s is computed from N_{ph}. For this machine, the windings are made up of two stators connected in series. The current I_a in each stator is therefore equal to the phase current, $I_{s(rms)}$ of 10A which gives a conductor diameter of approximately 1.6mm.

A Matlab® code was used to compute various generator parameters. Some of the constants were initialized as follows: $I_{s(rms)} = 10A$, $K_s = 0.95$, $k_{sf} = 0.48$, $B_{cs} = 1.5T$, $B_{cr} = 1.7T$, $\alpha_i = 0.80$, $A_s = 10{,}000A/m$, $p_{rl} = 0.2$, $PC = 6$, $E_f/V_{an} = 1.15$, $k_d = 0.7$, $w_s/\tau_s = 0.5$ and Grade 33 magnets with $B_r = 1.13T$. Table 5.2 shows the analytical results of the code.

Table 5.2 Analytical machine parameters

Torque (Nm)	6.33
n (rpm)	600
D_o (mm)	180
D_i (mm)	126
D_q (mm)	153
L_e (mm)	27
g (mm)	1.5
l_m (mm)	7
L_{stk} (mm)	81.5
$K_L = D_o/L_{stk}$	2.2
Slot-body-width, $w_{s\text{-}Dq}$ (mm)	16
Slot-opening, $w_{o\text{-}Dq}$ (mm)	9
Tooth-body-width, $w_{t\text{-}Dq}$ (mm)	24
Tooth-tip-width (mm)	31
B_{mq} (T)	0.742
$B_{1\max}$ (T)	0.899
B_{crit} (T)	0.565
B_q (T)	0.593
$B_{1tmax\text{-}Di}$ (T)	1.81
Flux/pole (Wb)	0.0007
k_{w1}	0.9331
PM Flux-linkage (Wb-turns)	0.0509
L_{cr} (mm)	12
N_{ph} (turns)	104
R_{ph} (Ohms)	0.16
E_f (V)	16
E_f/V_{an}	1.1436
V_{an} (V)	14
Current loading/stator, A_s (A/m)	9885.8

5.2 *Machine FEA Analysis*

The following machines are analysed and compared:

1. An AFPM machine and its equivalent RFPM with semi-open slots and a pole-arc ratio of 0.80.
2. Equivalent RFPM machines with semi-open slots and pole-arc ratios of 0.67, 0.72 and 0.61-0.80 (alternating pole-arcs).
3. An equivalent RFPM machine with open slots and a pole-arc ratio of 0.80.

4. An equivalent RFPM machine with semi-closed slots and a pole-arc ratio of 0.80.

An *equivalent RFPM machine* implies the modelling of an AFPM as an RFPM machine. All the machines have 10 trapezoidal poles and 12 slots. Machines under points one and two have parallel-teeth and trapezoidal slots (see Fig 5.2(a)). The last point has trapezoidal teeth and parallel slots (see Fig 5.2(b)). The open slots machine has no tooth-tips. Its tooth body is constant and resembles Fig 5.2(a) but with wider slots.

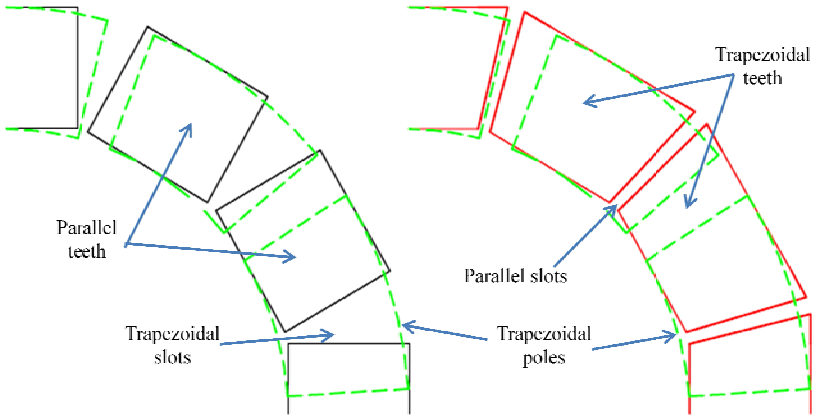

(a) Parallel-teeth and trapezoidal-poles **(b) Trapezoidal-teeth and trapezoidal poles**

Fig 5.2 Interaction of teeth and poles in an axial-flux machine

Setting-up and solving a FEA problem involves the following:

1. Determining the repeating basic winding element, i.e. periodicity, *F*. It is given as $F = \gcd(Q_s, p)$ in [66] and [68]. This applies if the coil configuration for the subsequent repeating winding elements remains the same, say C'A|A'A'|AB'|*C'A*|*A'A'*|*AB'*|…. If the FEA program (e.g. Flux 2D and 3D) has the capability of reversing the connection of the subsequent winding elements, i.e. C'A|A'A'|AB'|*CA'*|*AA*|*A'B*|…., then $F = \gcd(Q_s, 2p)$ [73]. The repeating element allows a section of the machine to be modelled saving on computation time.

2. The geometry is then generated using a CAD software and exported to the FEA environment. It can also be generated in the FEA program using primitive elements, i.e., lines and nodes.

3. Materials are then defined and assigned to the respective components of the geometry. Boundary and symmetric conditions are also assigned. The boundary conditions assigned to the ends of the elements depend on the ratio 2*p*/*F* [73]. If the ratio is odd, then negative or anticyclic boundary conditions are applied and if it is even, then positive or cyclic boundary

conditions are assigned. There are also conditions that can force the flux density to be perpendicular (Neumann) or parallel (Dirichlet) to a given boundary.

4. The problem is then meshed, solved and post-processing of the file is done.

The whole machine was modelled in Femm 4.2 environment, which is an open source 2D- FEA program available at http://femm.software.informer.com/4.2/download/. *F* was taken as unity to reduce the complexity of assigning some boundary and symmetric conditions. Fig 5.3 and Fig 5.4 shows a portion of an AFPM and that of an equivalent RFPM machine modelled in Femm 4.2 environment. In Flux 2D or 3D environment, a quarter of the machine was modelled (see Fig 5.5(a) and Fig 5.5(b) respectively). Anticyclic boundary conditions were assigned to the ends of the repeating unit since $F = 2$. The AFPM has symmetry along the dashed horizontal line as shown in Fig 5.3. The boundary conditions are the same in both 2D and 3D Flux models.

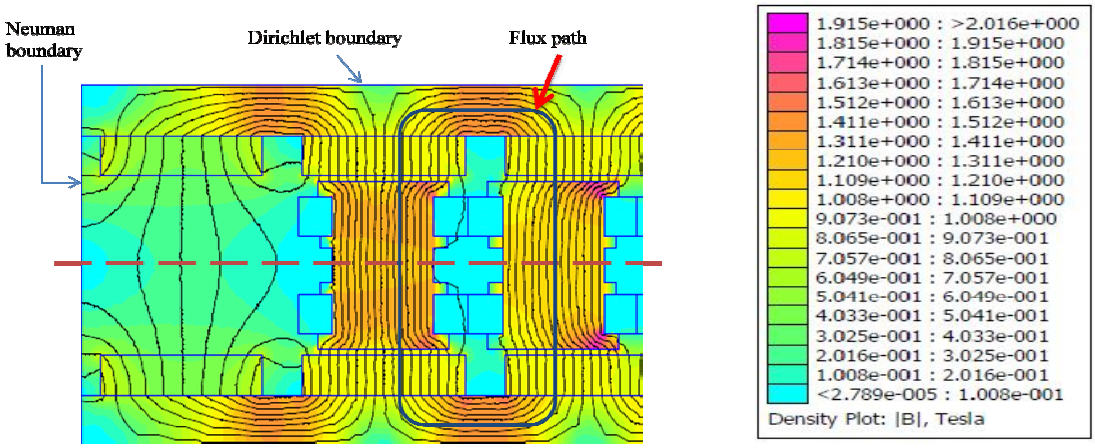

Fig 5.3 Flux density distribution in an AFPM machine

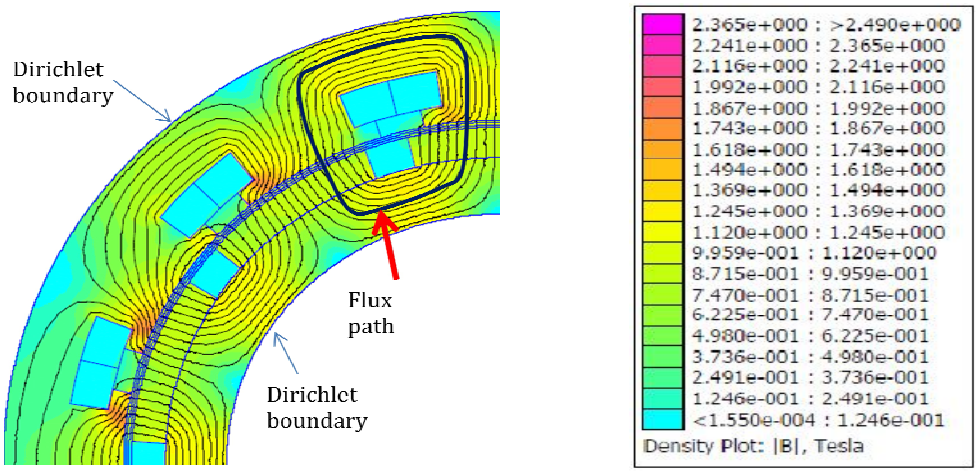

Fig 5.4 Flux density distribution in an RFPM machine

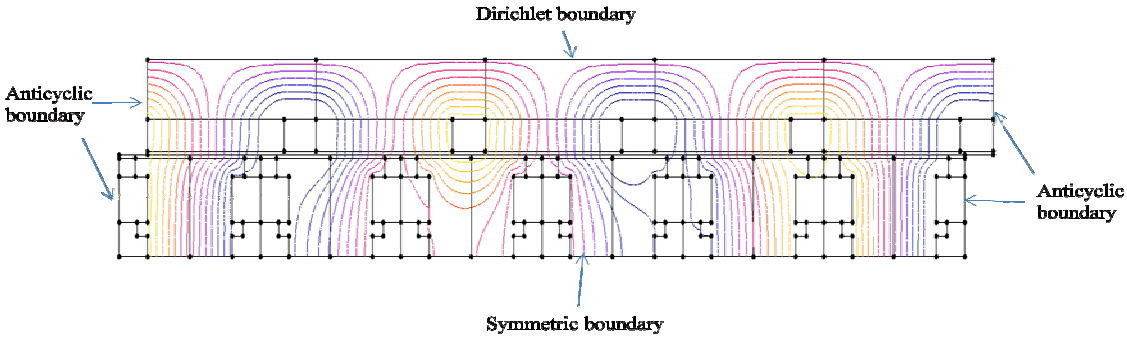

(a) 2D-model

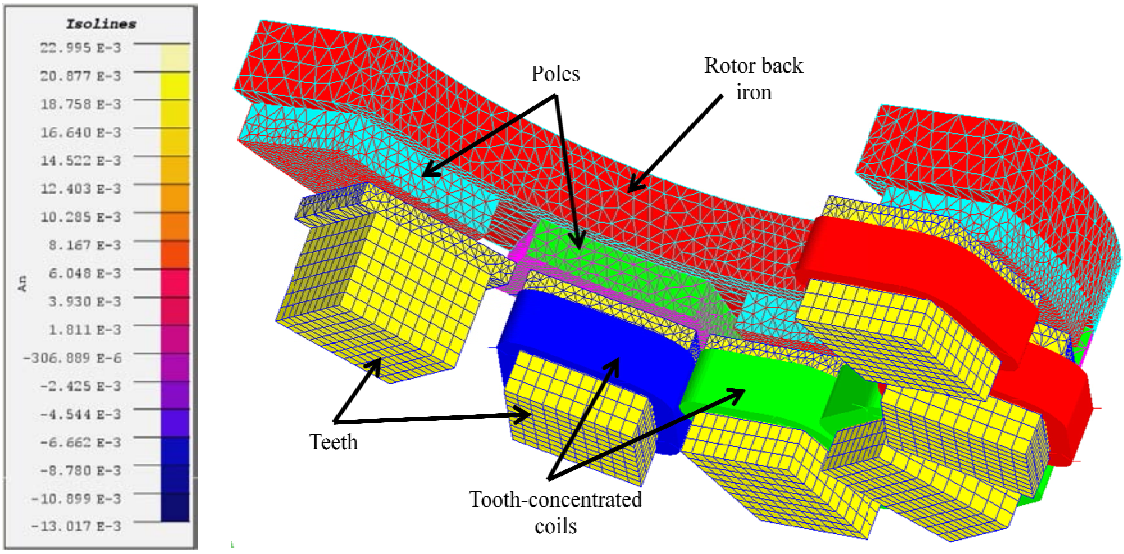

(b) 3D-model

Fig 5.5 Models in Flux environment; Isolines show the flux density in the 2D model

5.2.1 Modelling of an AFPM Machine as an Equivalent RFPM Machine

An AFPM machine can be modelled as an equivalent RFPM machine. This simplifies the problem by utilising existing RFPM methodology; especially in cogging torque analysis. The airgap diameter and the effective length of the RFPM are equated to the average diameter, $D_g = (D_o + D_i)/2$ and effective length, $L_e = (D_o - D_i)/2$ of the AFPM machine. The tooth-widths and the pole-widths are kept constant so that the interaction of the teeth and the poles is maintained after transformation. A half of the AFPM (along the dashed horizontal line in Fig 5.3) is modelled as an RFPM machine seen in Fig 5.4. In this case, the back-EMF and the torque obtained from the FEA analysis of the RFPM must be multiplied by a factor of two in order to model the whole AFPM machine.

An AFPM machine is usually simulated like a linear machine in 2D-FEA. Hence, dummy pole-pairs are added at the end of the machine as shown in Fig 5.3. This allows the translation of the rotor or stator laterally while keeping the flux density distribution uniform like that of a 'continuous' machine. This is solved by adopting the equivalent RFPM method. The flux path per pole pair in the AFPM machine is shorter (127mm) than that of the equivalent RFPM machine (151mm). This is evident by inspecting Fig 5.3 and Fig 5.4. Hence the airgap flux density of the equivalent RFPM machine will be slightly lower and will affect machine performance.

An AFPM machine can be modelled at the average diameter, D_g in 2D-FEA. Unfortunately it is inherently a 3D problem, i.e. most of the machine parameters are dependent on the radius. In addition, 3D electromagnetic effects such as leakage flux are neglected in analytical and 2D-FEA [69]. Analytical and 2D-FEA reduce complexity, preparation and computational time over 3D-FEA. This is especially true when complex shapes like skewing and alternating pole-arcs have to be analysed. It requires the whole machine to be modelled due to the lack periodicity. The accuracy of 2D-FEA can be improved by using quasi-3D-FEA. It involves sub-dividing the machine stator or pole into computational planes. In [69], quasi-3D analysis is compared with analytical, 2D-FEA and 3D-FEA. The stator or a pole is sub-divided into N slices which are then modelled as N machines using 2D-FEA. This is analogous to N machines which are mounted on the same shaft. This allows the back-EMF, the load voltage and torques to be summed algebraically. It also neglects 3D electromagnetic behaviour but it improves on the accuracy of the results. Fig 5.6 shows three pole slices which can be modelled at D_{g1}, D_{g2} and D_{g3} airgap diameters.

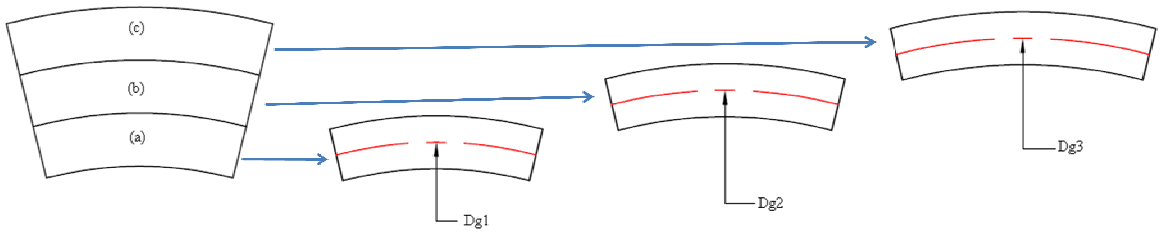

Fig 5.6 Pole slices

The number of slices, N is dependent on the purpose of the computation and also on the complexity of the machine geometry [69]. For instance, when the machine ratios, i.e. the slot-opening to slot-pitch and the pole-arc ratios are constant for all diameters, then one slice at D_g is sufficient to compute the back-EMF, the load voltage and torques. For a complex pole shape, like skewed poles, a number of planes that captures the general profile of the pole or stator are necessary.

5.2.2 Flux Density Distribution

Flux density was analysed at D_g since the pole-arc ratio is constant along the effective length. Fig 5.7(a) shows the full load normal, B_n and tangential, B_t components of airgap flux density. This was achieved by injecting a DC current of 10A into the three phases of the machine. The density was then obtained along a contour defined in the airgap. The effect of slotting on the reluctance is seen as cusps on the waveforms. The no-load airgap flux density will be approximately equal to that of the load, since the armature reaction effect is small, as seen in Fig 5.7(b). To obtain the airgap flux density due to armature reaction, the magnets were deactivated and the full load procedure was repeated. If the no-load airgap flux density is desired, there is no injection of the current into the windings.

Fig 5.7(c) and (d) shows both the normal and tangential components of flux densities in the rotor, B_{rtr}, the tooth-tip, B_{tip}, in the interface between the tooth-tip and tooth body, B_{int} and in the tooth body, B_{wt}. From Fig 5.7(c), the rotor flux density is fairly constant; about 0.5T which ensures the rotor discs are not saturated. Its tangential component varies with a peak density of about 0.2T as shown in Fig 5.7(d). Therefore, rotor losses like eddy-currents and core losses can be assumed to be negligible. From Fig 5.7(c) it can be seen that the stator steel is not saturated; the maximum is less than 1.5T. This is comparable to the flux density distribution in Fig 5.3. The maximum flux density is at the interior portion of the tooth body (Fig 5.7(c)). The tooth-tip has a wide area hence it has a low flux-density. This is because most of the flux 'gathered' by the wide tooth-tips cuts through the tooth body which has a reduced area. It is also high at the interface between the tooth-tip and the tooth body. The magnitudes of the tangential components for the tooth decreases towards the centre of the tooth as seen in Fig 5.7(d), as the reluctance increases.

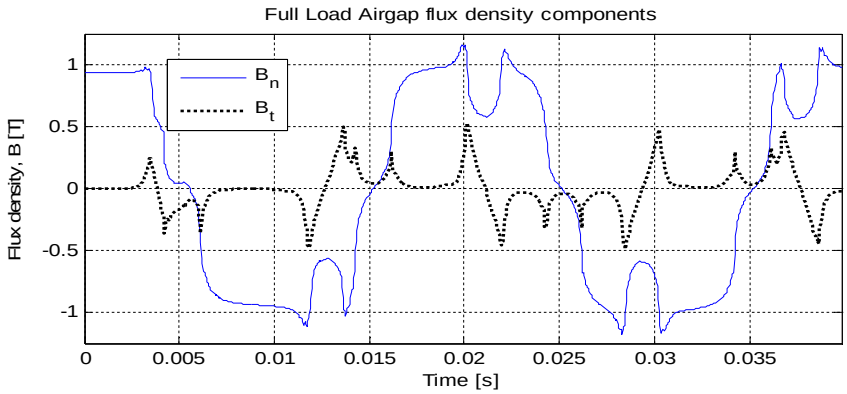

(a) Full load airgap flux-density components

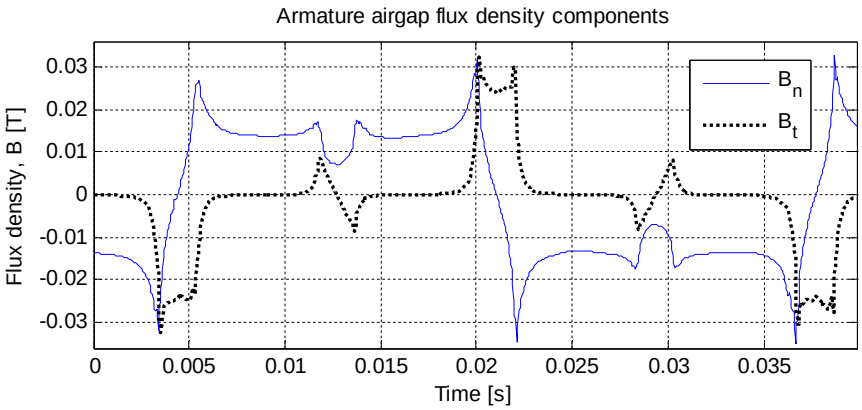

(b) Armature reaction airgap flux-density components

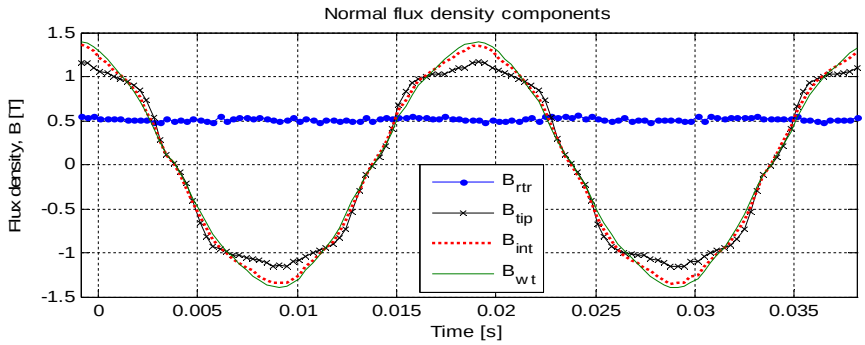

(c) Normal flux-density in the rotor and tooth structure

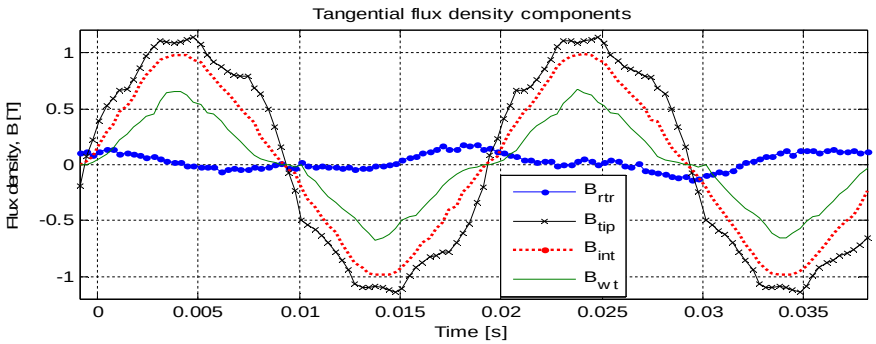

(d) Tangential flux-density in the rotor and tooth structure

Fig 5.7 Normal and tangential flux-density components

5.2.3 Back-EMF

To obtain back-EMF, zero currents are assigned to the stator windings and the rotor is stepped for one electrical cycle. The instantaneous flux-linkage, $\lambda(t)$ is obtained from Femm 4.2 which is then differentiated into the instantaneous phase voltage, $e(t)$ according to the relation $e(t) = -d\lambda(t)/dt$. It is important to verify the results of the equivalent RFPM methodology with those of the AFPM topology. They are comparable, though the phase back-EMF for the AFPM is slightly higher as

shown in Fig 5.8. This can be attributed to the higher flux-density in the AFPM due to a shorter flux path as noted earlier. The approximate RMS values for both the AFPM and equivalent RFPM are 18V and 17V respectively. The plot of the back-EMF at D_g and for N = 3 match for the two topologies (see Fig 5.8). Therefore analysis at D_g for back-EMF is sufficient and saves on computational time.

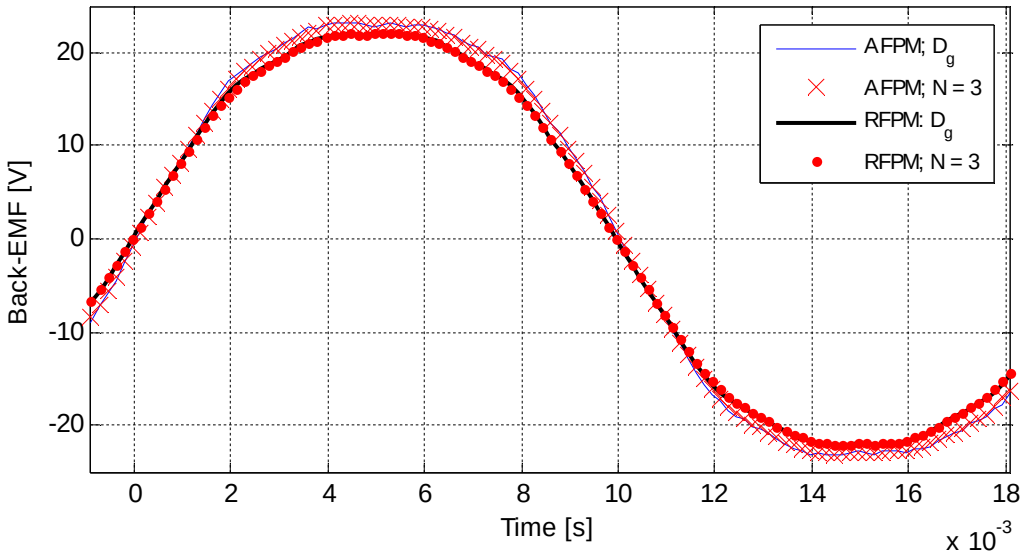

Fig 5.8 Back-EMF results at D_g and for N = 3 slices for an AFPM machine and its equivalent RFPM machine

Fig 5.9 shows the computation of per phase back-EMF using slices applied to the equivalent RFPM machine. EMF_1, EMF_2 and EMF_3 are the back-EMFs obtained at D_{g1}, D_{g2} and D_{g3} respectively, while *total* is their algebraic sum. In Table 5.3 and Table 5.4, the back-EMFs for all the machines with trapezoidal-teeth and parallel-teeth are compared. All the cases are analysed at the average diameter, D_g. A pole-arc ratio of 0.80 for the AFPM topology gives the highest back-EMF.

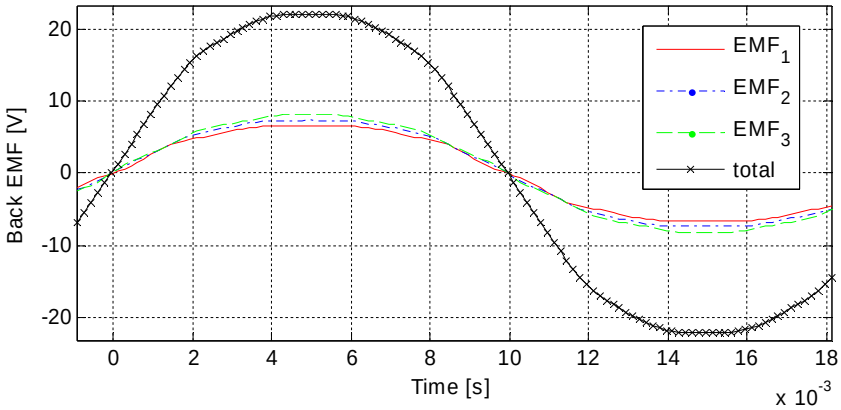

Fig 5.9 Back-EMF results at D_{g1}, D_{g2} and D_{g3} for the equivalent RFPM machine

In Femm 4.2, the load voltage is modelled by injecting current and accounting for the voltage drops. Flux allows the machine to be connected to a resistive load. Fig 5.10(a) shows 2D and 3D phase load

voltages, whose RMS values are 15.28V and 12.56V respectively. The 3D value is expected to be lower than that of the 2D value. Unfortunately, the difference is quite high and cannot be completely attributed to 3D leakage flux. 2D analysis also assumes a uniform pole area in the *z*-axis direction, which may make it to be slightly higher than that of the 3D model. The assignment of materials and boundary conditions was the same for the two models, but it seems that there was more MMF drop in the 3D case than in the 2D case. This is expected to affect other parameters of the machine such as cogging torque as shown in Fig 5.10(b).

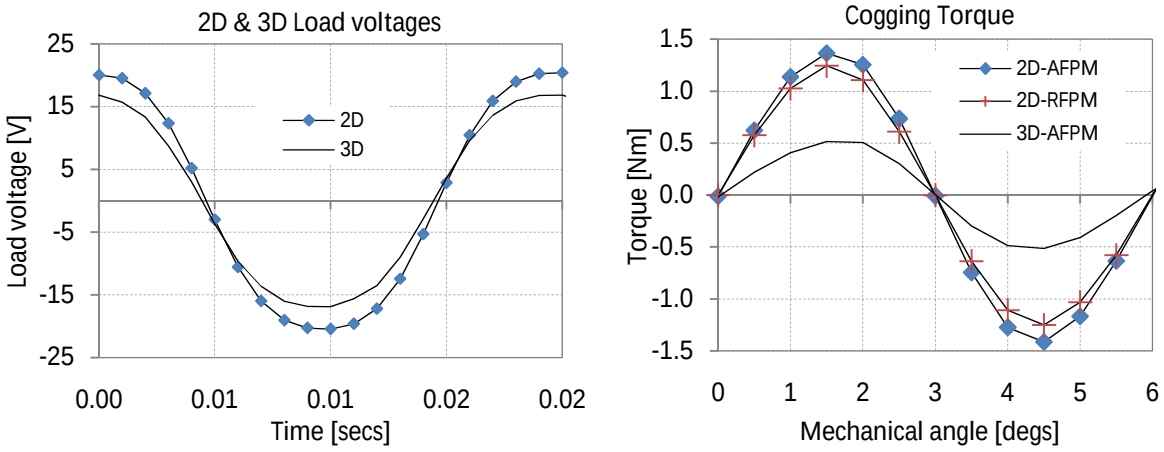

(a) Load voltage **(b) Cogging torque**

Fig 5.10 Comparison of load voltage and cogging torque in 2D and 3D-FEA

5.2.4 Quasi-3D Analysis of Cogging Torque

A parallel teeth-trapezoidal pole topology (which will be referred to as the parallel topology) has inherently less cogging torque than a trapezoidal teeth-trapezoidal pole topology (which will be referred to as the all trapezoidal topology). This is because the teeth have a rectangular skew which makes the machine ratios vary with diameter. This causes some cogging torque waveforms to be phase shifted as shown in Fig 5.11(a) at certain diameters. In the all trapezoidal topology, there is no phase shifting as evidenced in Fig 5.11(b). Therefore it can be analysed at the average diameter since the machine ratios are constant for all diameters.

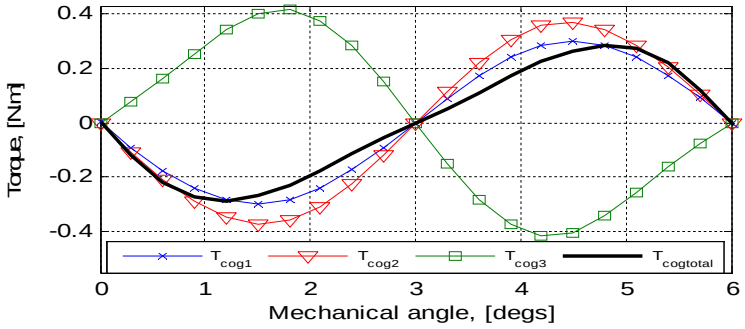

(a) Parallel case

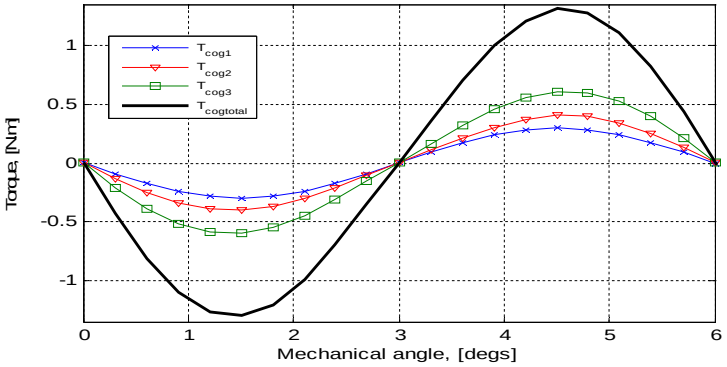

(b) All trapezoidal case

Fig 5.11 Quasi-3D cogging torque analysis for three slices

Cogging torque analysis was done for 3, 6 and 10 slices for the parallel topology. The results are as shown in Fig 5.12 (b). In Fig 5.11(a), cogging torque is shown for 3 planes. The waveform for the third slice is phase shifted by $n\pi$ where n is an integer. This is repeated in Fig 5.12(a) for 6 planes where it affects the fifth and the sixth slice. For 10 planes it affects the eighth to the tenth slice. From Fig 5.12(b), the resultant cogging torque waveforms for different slices are not consistent. Therefore, quasi 3D-FEA is not applicable to this particular case of parallel-teeth. This allows the use of the all trapezoidal topology for the analysis of cogging torque at the average diameter, D_g. It is used for comparing different methods of minimizing cogging torque. The best technique can then be adopted for the parallel case which is expected to have less cogging torque as noted previously.

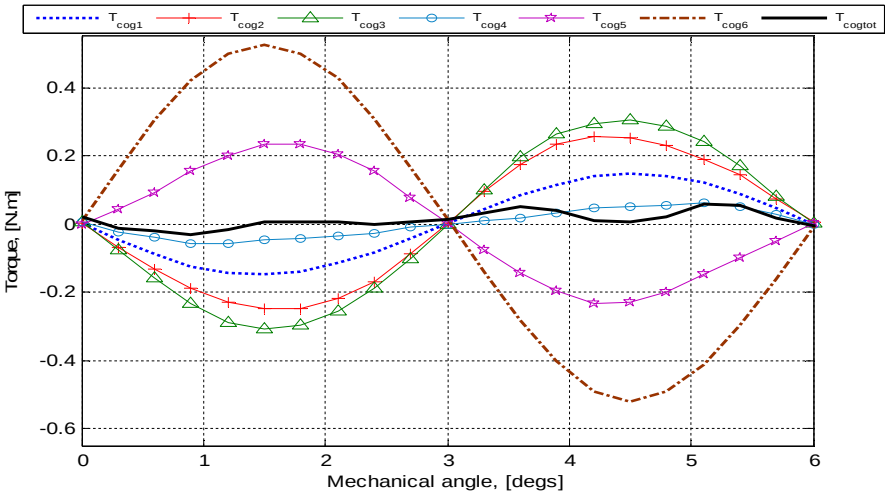

(a) 6 planes

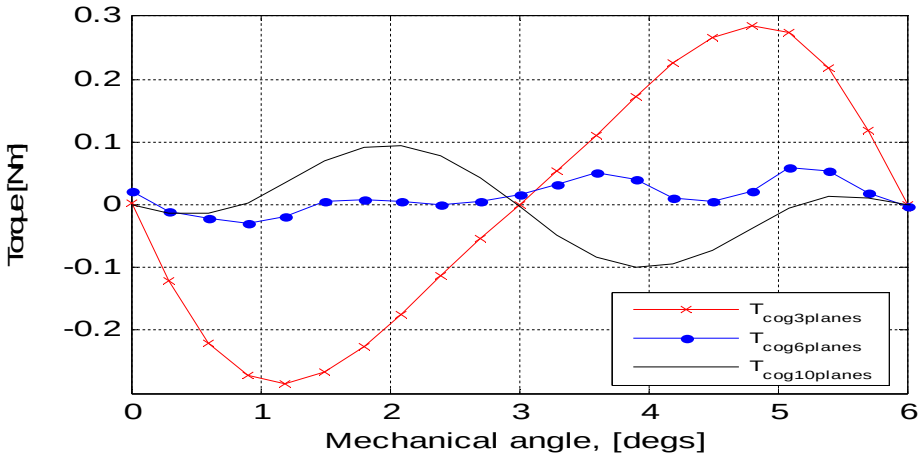

(b) Comparison of the 3, 6 and 10 planes

Fig 5.12 Application of quasi 3D-FEA to 3, 6 and 10 planes

5.2.5 Cogging Torque Minimization Techniques

The following methods will be analysed due to their practicality and ease in implementation. They include optimizing the pole arc ratio, alternating the pole-arc ratios, skewing, teeth-notching and combination of teeth notching and pole arc ratios. Most of these are as shown in Fig 5.13. It is easier to skew poles in AFPM machines than in RFPM. Alternating pole-arcs only require two sets of magnets. Notching is easier to implement in parallel-teeth where they can be blanked or laser cut during the manufacturing process.

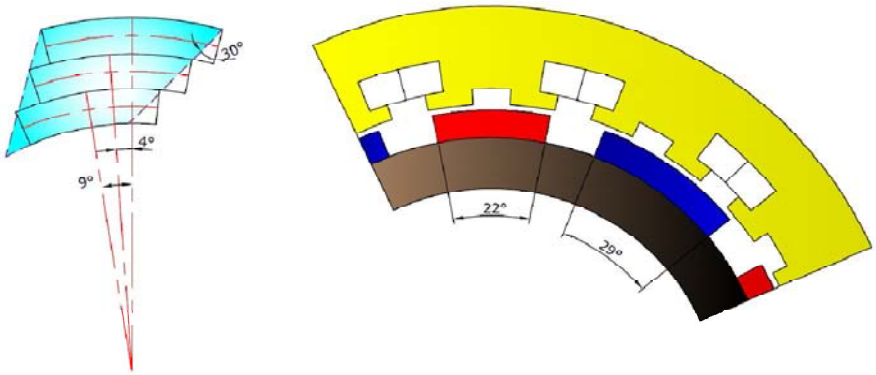

(a) Skewing **(b) Alternating pole-arcs and teeth notching**

Fig 5.13 Methods of minimizing cogging torque using the equivalent RFPM methodology

Fig 5.13(a) can be used to explain how skewing reduces cogging torque. The waveform for the middle slice is displaced by 4 mechanical degrees, whereas that of the inner portion is shifted by 9 mechanical degrees in reference to the outer slice. The resultant is the summation of the three waveforms which will not completely eliminate cogging torque. This is because the outer slice has the highest cogging torque since it has a longer pole-width at this diameter.

The cogging torque waveforms for different pole-arcs are as shown in Fig 5.14(a). A ratio of 0.72 and alternating pole-arcs of 0.61 and 0.80 give the least cogging torque. Teeth notching is applied to these pole-arc ratios except 0.67 as shown in Fig 5.14(b). This method reduces the magnitude of cogging torque effectively by doubling its frequency. Their peak torque is approximately the same.

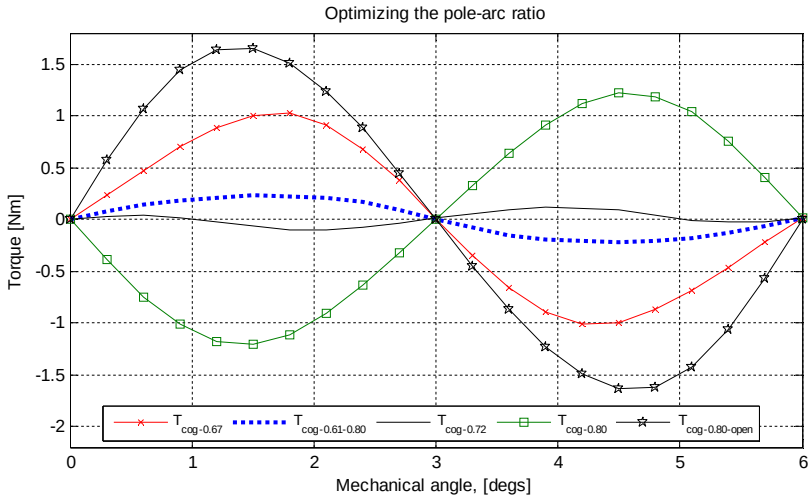

(a) Optimizing the pole-arc ratio

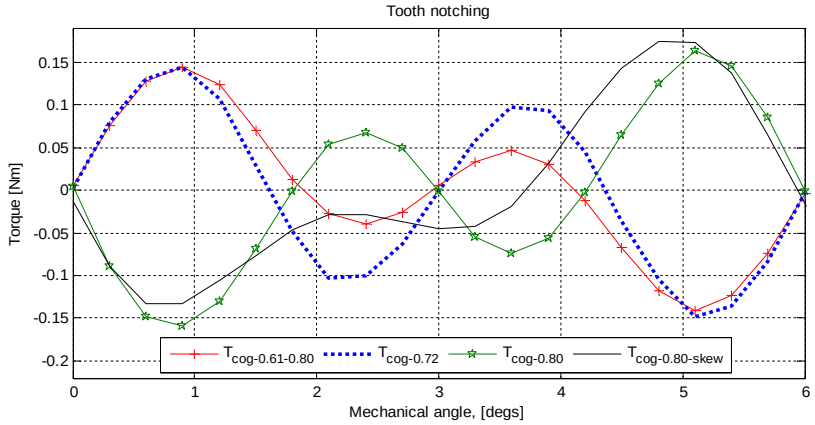

(b) Teeth-notching

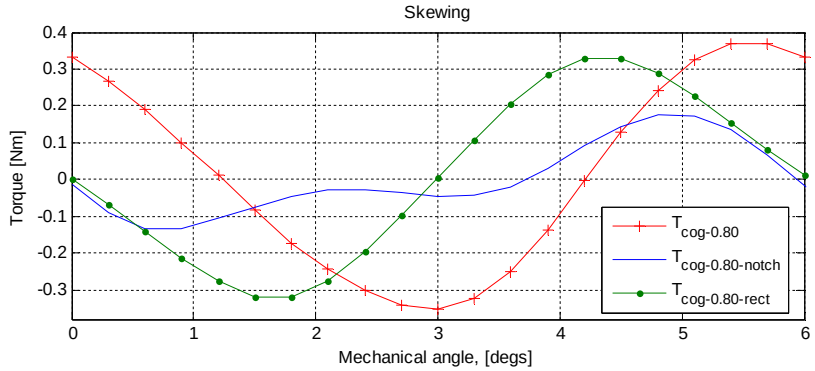

(c) Skewing

Fig 5.14 2D-FEA cogging torque results

Skewing is not as effective as teeth notching but it reduces the magnitude (see Fig 5.14(c)). In rectangular skew (rect), the pole width is the same for all diameters. It has high leakage flux at the inner diameter due to the proximity of the teeth. Its effectiveness compared to the ordinary skew is minimal. In all these cases the skew angle was one slot pitch.

In AFPM machines skewing does not completely eliminate cogging torque since the pole width is not the same for all diameters. Skewing allows the cogging torque waveforms to be phase shifted. This reduces the magnitude effectively by cancelation. This is usually the case in RFPM machines where skewing practically eliminates cogging torque when the skew angle is one slot pitch. The rectangular skew of the teeth and leakage flux at the inner diameter may have affected the effectiveness of the rectangular skew technique which was envisioned to reduce cogging torque effectively.

In Fig 5.15, 3D-FEA cogging torque results are presented. As expected the all trapezoidal case has the highest magnitude with a peak of 0.71Nm while the parallel case has a peak 0.54Nm. Skewing of the poles reduces the magnitude with the same result, i.e. 0.21Nm while the alternating pole-arc gives the

least cogging torque of about 0.1Nm. Table 5.3 shows the effect of cogging torque minimization methods on machine performance. The results are from 2D-FEA.

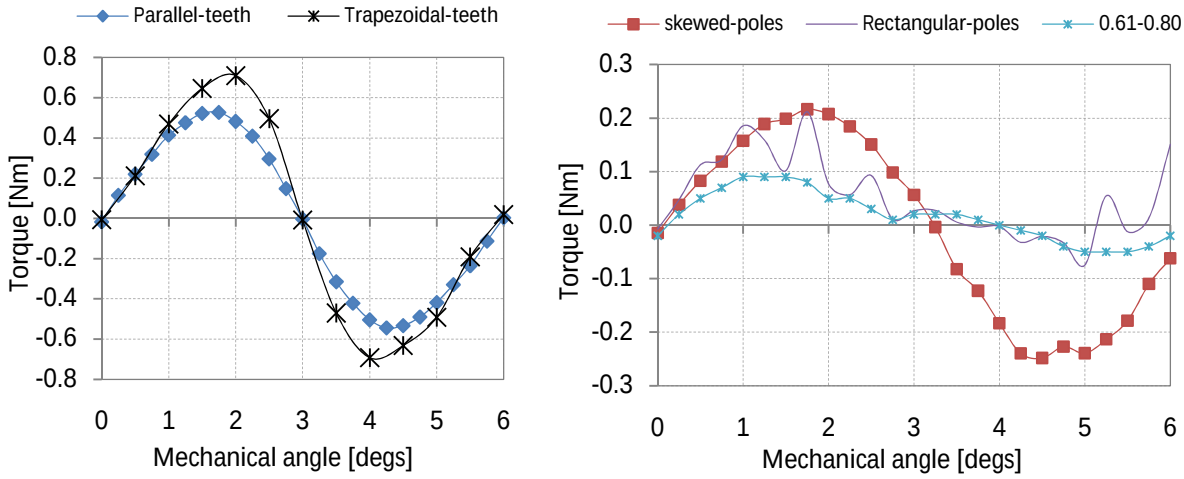

(a) **(b)**

Fig 5.15 3D-FEA cogging torque results

5.2.6 Developed Torque

In this case the machine was simulated like a motor. Currents were injected into the windings using *d-q* machine theory. The developed torque was then obtained by Maxwell's stress tensor method. The results for unity power operation are as shown in Fig 5.16(a)-(c). The effect of the pole area which affects the flux distribution can clearly be seen in the respective magnitudes. From the results, the cogging torque component is superimposed on the main torque. From Fig 5.16 (a) and (b), a pole-arc ratio of 0.72 minimizes torque pulsation. Notching and skewing also reduced the pulsations with notching giving the least by inspecting Fig 5.16(b) and (c).

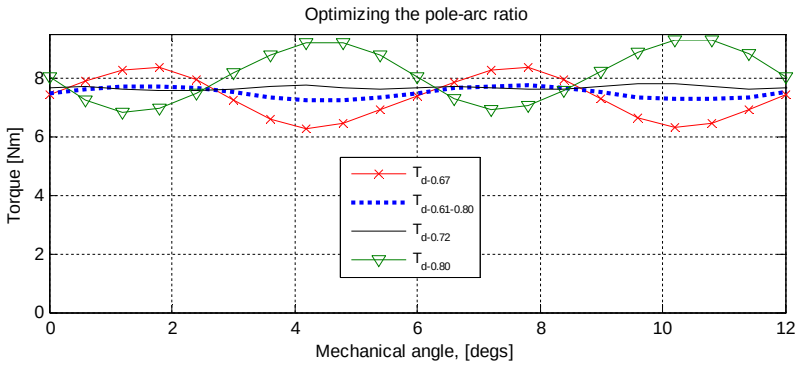

(a) Optimizing the pole-arc ratio

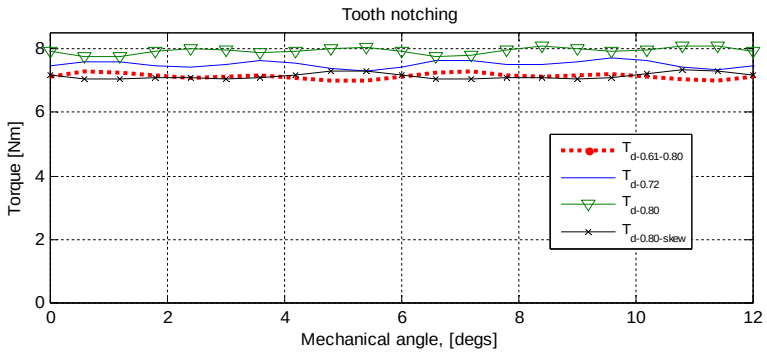

(b) Teeth-notching

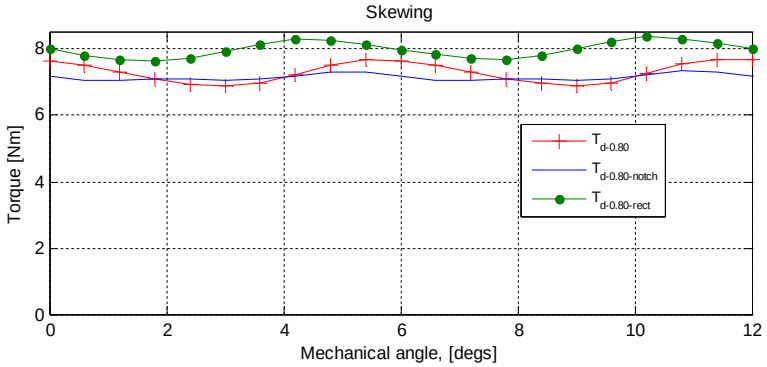

(c) Skewing

Fig 5.16 Torque developed

5.2.7 Analytical and FEA Estimation of Machine Performance parameters

The performance of the machines was determined using analytically and/or FEA methods. Losses were calculated analytically from the theory developed in Section 4.5. Unity power operation was assumed with a phase current of approximately 10A at a shaft speed of 600rpm.

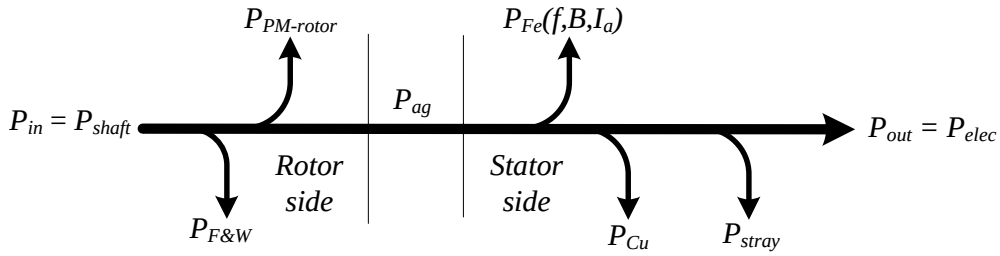

Fig 5.17 Power flow diagram in a PMSG

Fig 5.17 shows the power flow diagram in a PMSG. The rotor eddy-current and core losses are lumped as $P_{PM\text{-}rotor}$. They are assumed to be negligible since the rotor's flux-densities were shown to be constant in Section 5.2.2. For analytical estimation of the generator performance, the input shaft

power, P_{in} is given by the summation of airgap power, P_{ag} and friction & windage losses, $P_{F\&W}$. The output electrical power, P_{out} is obtained by deducting copper losses, P_{Cu}, core losses, P_{Fe} and stray load losses, P_{stray} from airgap power. The airgap power is given as $P_{ag} = 3E_f I_{s(rms)}$; assuming all the phases are balanced. The core losses are assumed to be independent of load, hence constant. For core losses, k_{adt} is set to 1.85 and k_{ady} = 0 since the stator is yoke-less. The specific core loss, $\Delta p_{1/50}$ is 1.1W/kg at 1T and 50Hz for M270-50A steel, the bearing friction factor, k_{fb} was equated to $2m^2/s^2$ and the stray load coefficient, k_{stray} was set to 0.04. The losses were obtained as ΔP_{Cu} = 48W, ΔP_{fr} = 9.76W, ΔP_{wind} = 0.016W, ΔP_{Fe} = 19.35W and ΔP_{stray} = 15W, giving a total loss of 92.126W. It can be seen that the copper losses are dominant and the windage losses are low since the machine is operating at relative low speeds.

In Table 5.3 the effect of cogging torque minimization methods on machine performance are presented.

Table 5.3 Effect of cogging torque minimization on machine performance for all trapezoidal case

Pole-arc	Cogging Torque		$EMF_{(RMS)}$ [V]	$T_{d\ (RMS)}$ [Nm]	P_{ag} [W]	P_{in} [W]	P_{out} [W]	Eff [%]	P_{out}/P_{rated}
	T_{cog_pk} [Nm]	% of 6.33Nm							
0.67	1.025	16.19	15.6	7.39	475	485	391	81	0.93
0.61-0.80	0.239	3.78	15.9	7.5	484	494	401	81	0.95
0.72	0.113	1.79	16.3	7.66	497	506	413	82	0.98
0.8	1.219	19.26	17.2	8.25	524	534	440	82	1.05
Open-slots-0.80	1.653	26.11	15.4	7.58	469	479	385	80	0.92
0.61-0.80-notch.	0.144	2.27	15.2	7.16	463	473	379	80	0.90
0.72-notch.	0.145	2.29	16	7.53	487	497	404	81	0.96
0.80-notch.	0.167	2.64	16.9	7.95	515	525	431	82	1.03
0.80-skew	0.368	5.81	16.3	7.29	497	506	413	82	0.98
0.80-skew-notch.	0.177	2.80	16	7.16	487	497	404	81	0.96
0.80-rect.-skew	0.335	5.29	16.8	7.54	512	522	428	82	1.02

The performance of different machines employing parallel-teeth is also investigated and the results are as shown in Table 5.4. Their performance is similar to that of the machines with trapezoidal teeth. Table 5.4 also compares the performance of the equivalent RFPM and the AFPM. The ratio P_{out}/P_{rated} is used to check whether a given topology meets the rated power, P_{rated} of 420W = 3×10A×14V. It can be seen that all efficiencies are within a range of 79-82%. Topologies with a pole-arc ratio of 0.80 have better performance than the rest of the machines in terms of torque developed and the back-EMF. This can be attributed to higher flux due to a wider non-skewed pole area.

Table 5.4 Performance of machines with parallel-teeth

Pole-arc	$EMF_{(RMS)}$ [V]	$T_{mtr\ (RMS)}$ [Nm]	P_{ag} [W]	P_{in} [W]	P_{out} [W]	Eff [%]	P_{out}/P_{rated}
0.67	15.3	7.27	466	476	382	80	0.91
0.61-0.80	15.7	7.38	479	488	395	81	0.94
0.72	16.0	7.54	487	497	404	81	0.96
0.8	17.0	7.95	518	528	434	82	1.03
AFPM-0.8	18.1	-	550	560	466	83	1.11
0.61-0.80-notch.	14.6	6.88	445	455	362	79	0.86
0.72-notch.	15.0	7.04	457	467	373	80	0.89
0.80-notch.	15.8	7.41	481	491	398	81	0.95
0.80-skew	16.8	6.25	510	520	426	82	1.02
0.80-skew-notch.	15.3	6.78	466	475	382	80	0.91
0.80-rect.-skew	16.7	7.86	509	519	426	82	1.01

The voltage regulation and efficiency of the equivalent RFPM and AFPM are compared in Fig 5.18. The difference in the two parameters can be associated to the flux-density as noted previously. This affects the back-EMF (see Table 5.4) which is used to compute the efficiency and the load voltage by factoring in the per phase resistance.

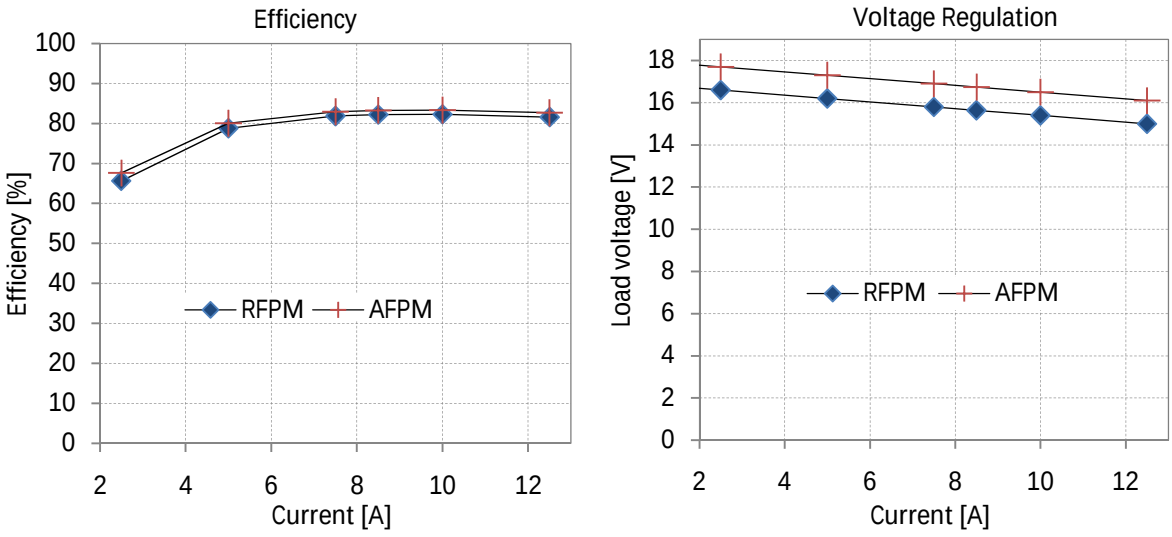

(a) Efficiency **(b) Voltage regulation**

Fig 5.18 Performance comparison of the equivalent RFPM machine with the AFPM machine

5.3 *Conclusions*

In the machine design section, it was shown that by optimizing the number of poles and slots, cogging torque can be mitigated by increasing its frequency. The section also showed the selection of the magnet grade which affects the magnet loading of the machine and cogging torque.

The AFPM was also modelled as an equivalent RFPM. This allowed the use of existing RFPM FEA methods in analyzing the AFPM machine. This was especially helpful in determining cogging torque, which was difficult when the AFPM was modelled in Femm 4.2. It also allowed the comparison of different cogging torque minimizing techniques and their effect on machine performance. A pole-arc ratio of 0.72, teeth-notching, alternating pole-arcs and skewing reduced cogging torque to less than 6% of the rated torque. These topologies also had a reduced torque ripple. A pole-arc ratio of 0.72 gives the least cogging torque of about 1.8% of the rated torque. The topology with open slots had a poor performance with a maximum cogging toque of 26.11% of the rated torque. Machines with pole-arc ratios of 0.67 and 0.80 had the highest cogging torque of about 16% and 19% of the rated torque. Their torque ripples were also high. This is expected since the contribution from current harmonics is negligible. This is because sinusoidal currents and unity power factor operation were assumed for the simulations. Hence the pulsating torque is mainly due to cogging torque.

This chapter also showed the limitations of 2D-FEA and quasi-3D-FEA in analysing cogging torque in machines with parallel-teeth. This allowed the use of the trapezoidal case as a bench mark for comparison. The methods analysed can then be applied to the parallel case, banking on the fact that this case is expected to have less cogging torque due to its inherent rectangular skew. Quasi-3D analysis can also be used to explain the working principle of skewing by phase shifting of cogging torque waveforms. This in effect leads to cancellation which reduces its magnitude.

The parallel-teeth topologies were also compared with trapezoidal-teeth topologies. The results show that the difference is very minimal. For instance the back-EMF was 17.2V for the trapezoidal and 17V for the parallel case. The AFPM topology was also shown to perform better than the equivalent RFPM machine. This is due to higher flux density due to a shorter flux path as pointed out earlier. Its back-EMF was 18.1V, which subsequently affected all the other parameters of the machine. It also has a higher efficiency of 83%, whereas the equivalent RFPM has an efficiency of 82%. Despite this, the methodology was successfully employed in analysing and comparing different topologies of AFPM machines.

From the FEA analysis, it can be said that the machine theory holds and it was verified using simulations, but for mitigating cogging torque and torque ripple every machine can be said to be unique. From literature [25], [62], [70], a pole-arc of 0.67 was said to be effective in reducing cogging torque and a pole arc of 0.80 in mitigating ripple torque. From this analysis a pole-arc of 0.72 proved to be optimum.

6 Prototyping and Testing

In this chapter, the construction of a parallel-teeth stator and the assembly of the machine are discussed in detail. Three machines were prototyped, i.e. one with a pole-arc ratio of 0.80, another with alternating pole-arcs of 0.61 and 0.80, and finally one with skewed poles. The experimental performance of these machines is compared to investigate the effect of minimizing cogging torque by skewing and using alternating pole-arcs. Experimental performance parameters such as no-load voltage, voltage regulation and efficiency are determined. An estimation methodology for core losses and stray losses is also described. Finally, the experimental machine parameters are compared with analytical and FEA values. This is will show that the machines met performance requirements.

6.1 *Prototyping*

This section deals with the prototyping and the assembly of the machine structure. The requirements for the teeth support structure is to prevent the rocking of the teeth due to the strong magnetic forces, and to prevent the short-circuiting of laminations. One of the main set-backs in iron-cored AFPM machines is associated with the manufacture of the stator slots. They are typically made by coiling a pre-punched strip or by machining slots in a pre-coiled steel core. The problem associated with each is alignment of slots in the pre-punched case and short-circuiting of laminations in the slot machining process [59]. This can be solved by using pre-formed soft magnetic composite (SMC) teeth or a yoke-less parallel-teeth stator.

In an SMC core, the teeth are made of a composite material with 3D-electromagnetic properties. They are then fitted onto a laminated yoke. This introduces assembly problems in holding the teeth and also the integrity of the electromagnetic circuit [59]. Other disadvantages of SMC cores are: higher core losses, lower relative permeability and the need for machining the slots, which have detrimental effects on the same that require chemical treatment [59]. Parallel-teeth can solve most of these problems by adopting a twin rotor-inner stator topology. This topology eliminates the need for a yoke and the challenge reduces to that of holding the teeth.

In Chapter 5, FEA analysis was used to compare the performance of the parallel-teeth topology to that of a trapezoidal-teeth topology. It was concluded that the parallel-teeth topology met the performance requirements and inherently lowered cogging torque. Another significant advantage of topology is the standardisation of the punch and die because the laminations are identical. This eliminates the

problem of advancing the lamination strip when teeth are made from a pre-punched strip. It is important to point out that a yoke-less trapezoidal-teeth stator structure would require different sizes of punches and dies as the tooth width increases with the average diameter in order to keep the slots identical. The parallel-teeth topology eliminates the need for machining slots which has to be done for a pre-coiled core and for SMC cores. It also allows the teeth to be pre-wound with coils and assembled in modules. It results in tightly wound coils that improve heat transfer and have a high slot-fill factor. Another advantage of the modular assembly is the ease of rewinding the stator coils, where faulty coils can be wound independently.

6.1.1 PM Rotor Discs

The PM rotors were made of low carbon steel (Grade 1018) which has relatively good permeability. The three rotors are as shown in Fig 6.1(a) to (c). The skewed PM pole pieces have a skew of one slot pitch, i.e. 30 mechanical degrees. The shaft was made of non-magnetic stainless steel (Grade 316).

(a) 0.61-0.80

(b) Skew

(c) 0.80

Fig 6.1 PM rotor discs

6.1.2 Stator Structure

The laminations were made of non-oriented silicon steel (M270-50A or 50H270 or 50A270). This type of steel has better performance than 50A310 and 50A350. It has lower core losses as shown in Table 6.1 and higher permeability and an acceptable saturation curve as shown in Appendix D.

Table 6.1 Core losses in some machine steels

JIS	Thickness [mm]	W/kg at 50Hz 1T	1.5T	Density [kg/dm^3]	Resisitivity [μΩ-cm]
35A270	0.35	1.1	2.7	7.65	54
50A310	0.50	1.25	3.10	7.65	54

50A270	0.50	1.1	2.7	7.60	55
50A350	0.50	1.5	3.5	7.65	51
Source: http://www.jfe-steel.co.jp/en/ (01 June, 2010)					

The main challenge in this type of stator is holding the teeth without short-circuiting the laminations and to provide mechanical integrity. The teeth were to be held by an aluminium flange arrangement as shown in Fig 6.2(a). From the figure it can be seen that the laminations are short-circuited on both sides, which would increase eddy-current losses. The structure was modified to the one shown in Fig 6.2(b), where a bakelite insulator was used to break the eddy-current path. A peg structure was used to retain the teeth in the slot. Extra mechanical support was provided for the peg by sandwiching it between the aluminium flanges. This would also establish a current path but it was assumed that its effect would be negligible. This structure was expected to perform optimally. It is applicable to low frequency machines like wind generators where core losses are small compared to the more dominant copper losses. The actual fabricated teeth support is shown in Fig 6.3.

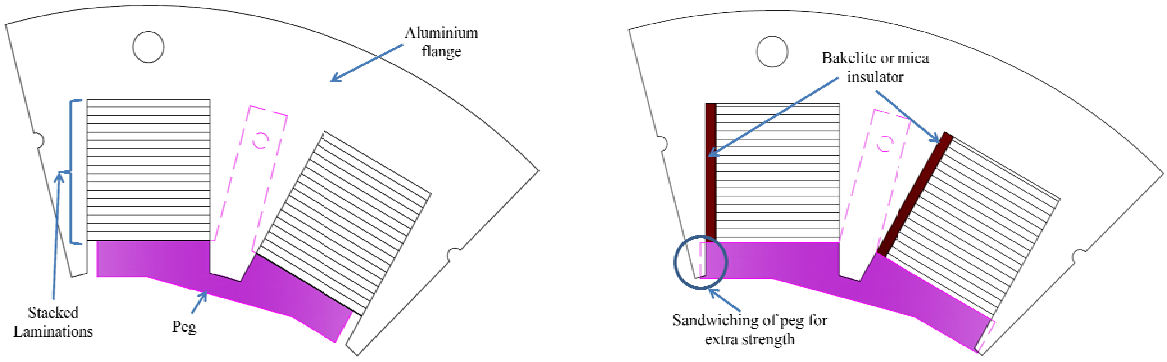

(a) **(b)**

Fig 6.2 Holding of the teeth

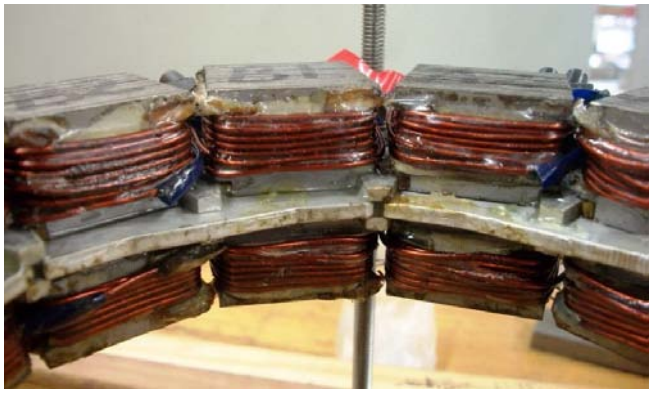

Fig 6.3 The actual fabricated teeth holding structure

Epoxy was used to hold and eliminate voids between the coils to improve heat conductivity. The windings were made of 1mm copper wire with a temperature rating of 200 ºC. Each phase was made up of 8 coils connected in series and each coil had 12 turns. An insulation test was done on each coil

at 500V. A Perspex dummy stator, which was used in the estimation of friction & windage losses, was also constructed. A wound tooth, the aluminium support structure for the teeth, the assembled stator and the dummy stator are as shown in Fig 6.4.

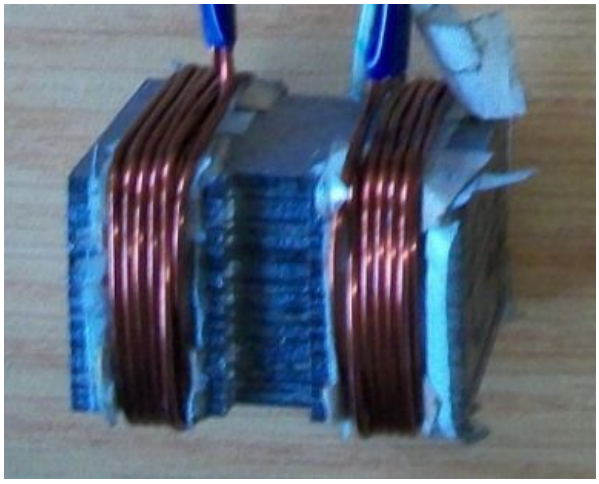

(a) A wound tooth

(b) Aluminium flange

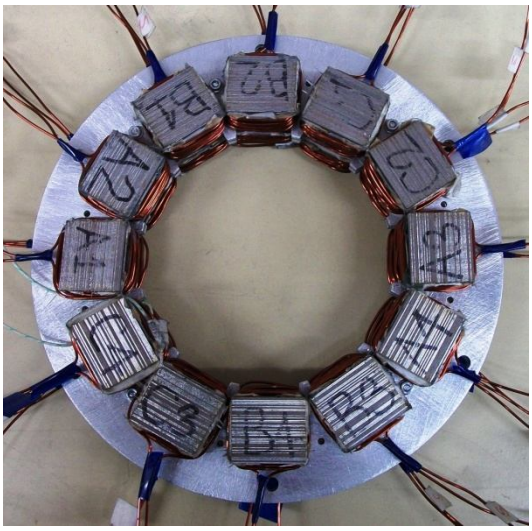

(c) Assembled stator

(d) Dummy stator

Fig 6.4 Assembly of parallel-teeth stator and dummy stator

The assembly and disassembly of an AFPM machine is difficult due to the strong axial forces between the PM rotors and the risk of injury to the personnel. This was achieved by securing the frame of the machine by means of a non-magnetic structure that withstands the axial loading as a result of the attractive force between the stator teeth and PM rotors. Threaded non-magnetic stainless steel rods met these requirements. The threaded rods allowed the airgap to be adjusted in the axial direction (parallel to the machine shaft). Fig 6.5 shows an assembly rig that allows the PM rotor discs

to be advanced and retracted without clamping onto the stator teeth. The rig proved to be a perfectly safe way to handle the PM rotor discs and facilitated the safe assembly of the machines.

Fig 6.6 shows the machine mounted onto a test rig. A DC machine was used as a prime mover and a Magtrol® in-line torque transducer with a rating of 200Nm measured the shaft speed and torque. A WT 1600 Yokagawa® power analyzer was used to acquire the current, voltage, power, speed and torque readings.

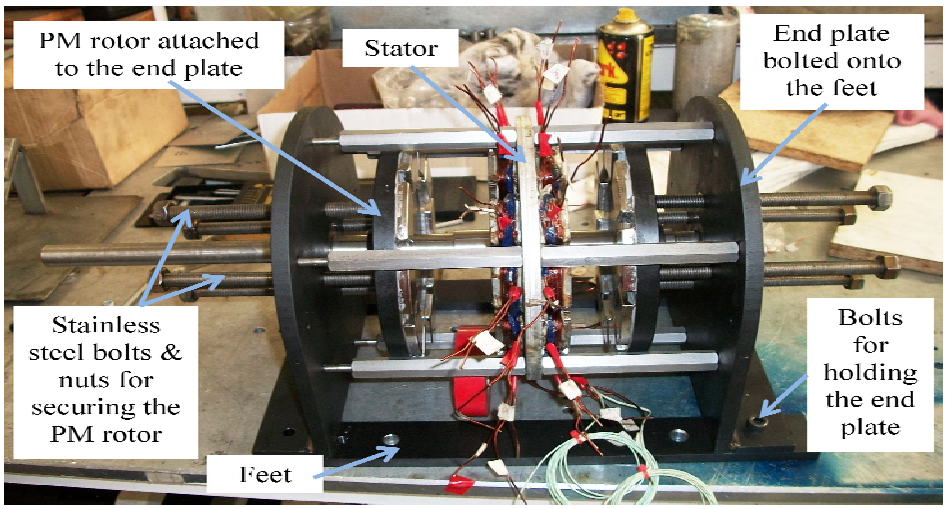

Fig 6.5 Assembly and disassembly rig

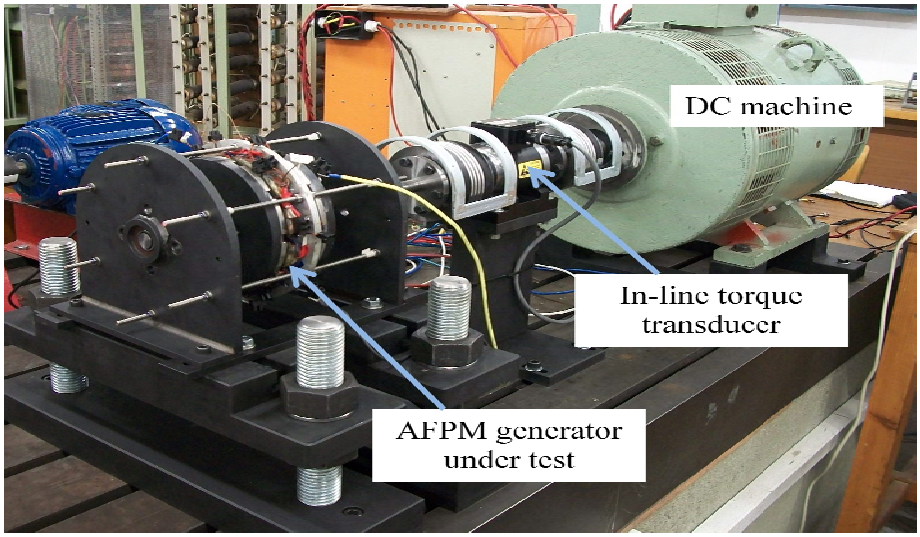

Fig 6.6 AFPM generator mounted on the test rig

6.2 *Experimental Results*

This section presents the no-load, the load and cogging torque experimental results. The no-load test was used to estimate core-losses at no-load and the back-EMF. The load test was used to estimate voltage regulation, efficiency, stray load losses and core losses due to loading.

6.2.1 Back-EMF

The coil, phase and line no-load voltages are shown in Fig 6.7(a) to (c) for a machine with a pole-arc ratio of 0.80. The line voltage, *U*1 is inverted by the power analyzer. Their RMS values at a rated speed of 600rpm are 2.34V, 17.91V and 30.88V respectively. From Fig 6.7(b), it can be seen that the machine is balanced in magnitude and in phase.

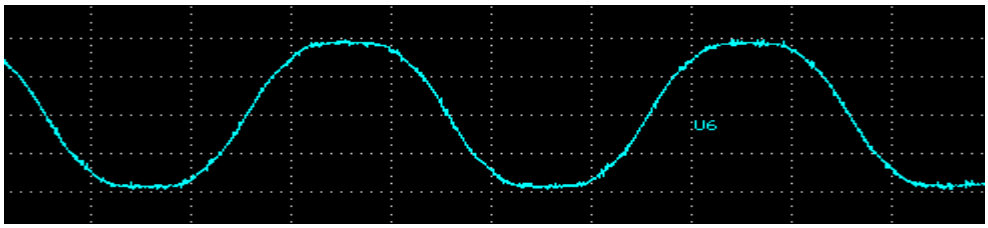

(a)Tooth no-load voltage

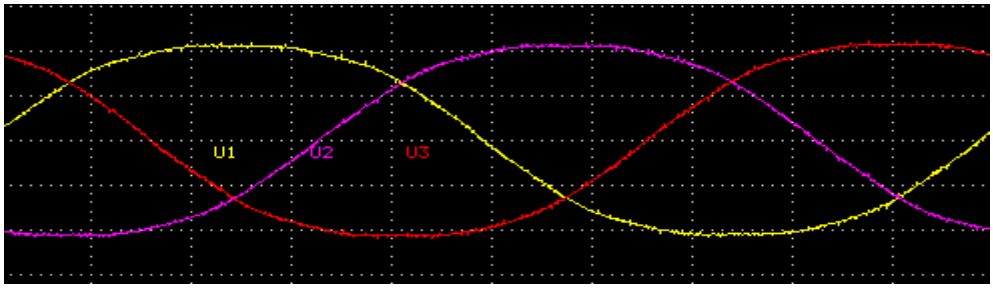

(b)Phase no-load voltages

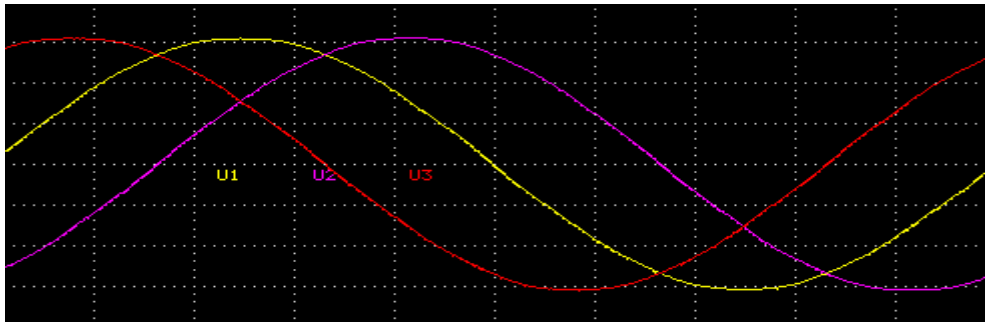

(c)Line-to-line no-load voltages

Fig 6.7 Induced no-load voltages of a machine with a pole-arc ratio of 0.80

The total harmonic distortions (THD) for the coil, phase and line back-EMFs are 9.71%, 6.61% and 0.61% respectively. This is evident by the reduced flat tops in Fig 6.7(c). The low harmonic content is due to the distribution of the windings, i.e. connection of the distributed individual coil voltages into a phase and elimination of triplen harmonics in the line-line voltage of a 3-phase connection. The harmonics for the coil, phase and line-line no-load voltages are shown in Fig 6.8(a). In Fig 6.8(b), the harmonics in the no-load phase voltage for the three topologies. Their total harmonic distortions of the rotors with a pole-arc ratio of 0.80, alternating pole-arcs and the skewed PM rotor are 6.61%, 2.51% and 4.18%, respectively. It can be seen that the magnitude of the 3rd harmonic is proportional to the fundamental voltage induced, i.e. 17.9V, 16.5V and 17V respectively. Therefore, the contribution of magnets to harmonic is related to the pole area and the useful airgap flux. It is important to note that it is only the 3rd harmonic which is approximately 3% of the fundamental voltage.

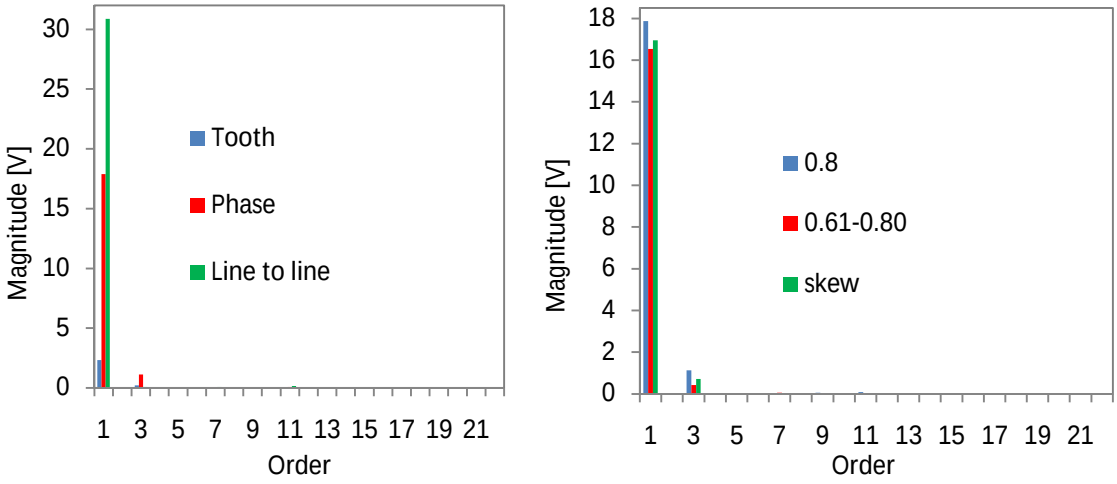

(a) **(b)**

Fig 6.8 No-load voltage harmonics at 50Hz

The no-load voltage as a function of shaft speed is shown Fig 6.9. A pole-arc ratio of 0.80 has the highest values. This can be attributed to the uniformly distributed flux-density, associated with the pole shape which gives a higher flux-linkage of 0.0567Wb-turns. It also has more useful flux compared to the case with alternating pole-arcs. The rotor with skewed poles has the same magnet volume as that of the pole-arc ratio of 0.80, but due to its shape its flux-linkage is reduced to 0.0540Wb-turns. The alternating pole-arc has the lowest magnetic volume giving a low flux-linkage of 0.0525Wb-turns. The PM flux-linkage, λ_{PM} is given by the stator flux-linkage, λ_s obtained from eqn (6.1), and the slope of the experimental data at steady-state and no-load conditions.

$$v_s = \omega_e \lambda_s \tag{6.1}$$

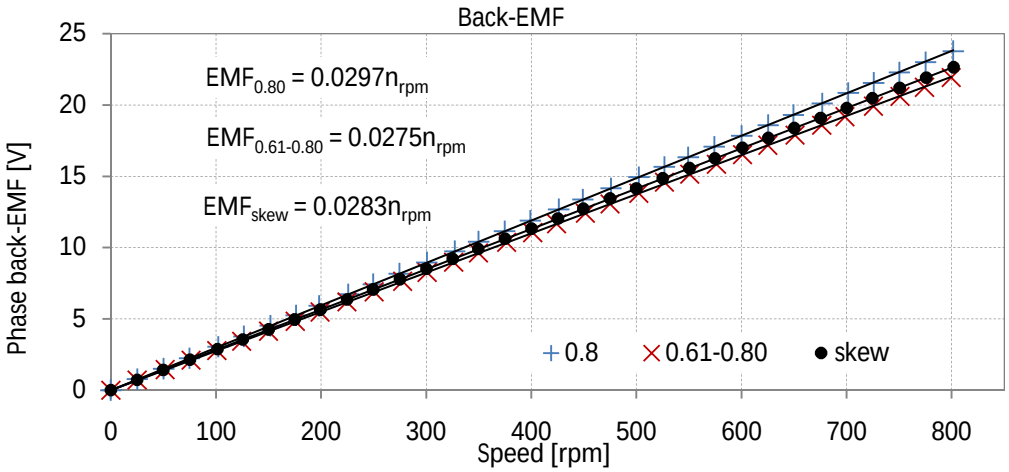

Fig 6.9 Experimental phase back-EMF

6.2.2 No-load Losses

The no-load losses, $P_{x\text{-}No}$ are given by the summation of friction & windage losses, $P_{F\&W}$ and core losses, P_{Fe}. No-load losses were obtained by running the machines at zero load current, whereas the friction & windage losses were determined by running the machines with a dummy stator. The latter eliminates core losses from the measured losses. The no-load losses are shown in Fig 6.10 as a function of shaft speed. They should not vary much from each other since the rotor masses are approximately the same although the alternating pole-arc has a slightly reduced mass. The windage losses are expected to be the same since they use the same stator structure and the differences in the pole shapes can be assumed to be negligible. It is important to point out that the friction losses do not cater for the axial loading due to the attractive forces between the PM rotors with the stator steel. This force will result in higher friction loss on the radial bearings, compared to a purely radial load.

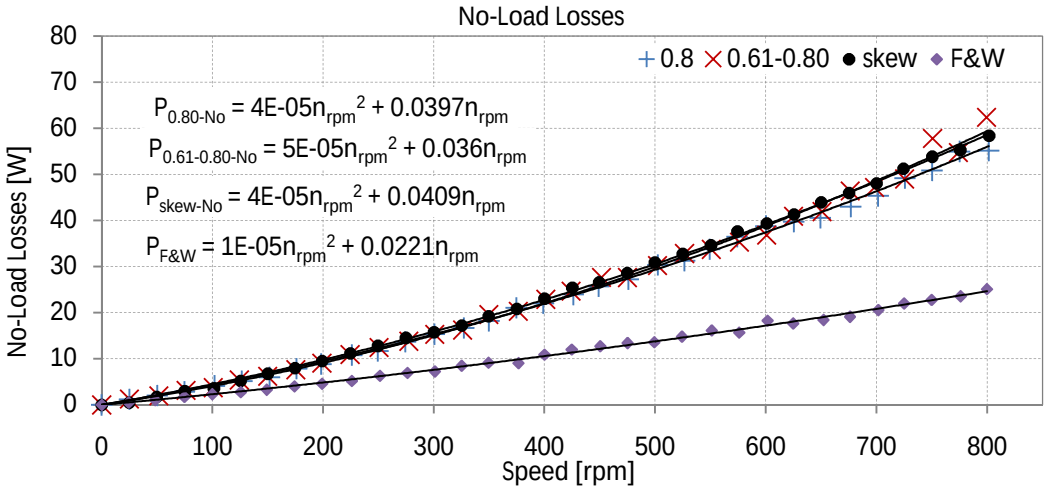

Fig 6.10 No-load losses

6.2.3 Core Losses

Core losses are obtained by deducting the friction & windage losses from the no-load losses. Core losses are present at no-load in a PMSG and are a function of speed and flux-density. An addition of core loss component is present due to armature reaction effects under loaded conditions. These can be approximated as [59]

$$\left.\begin{aligned} P_{Fe}(f,B,i_s) &\approx K_c(f)\lambda_s^2(B,i_s) \\ \lambda_s^2 &= \lambda_d^2 + \lambda_q^2 = (\lambda_{PM} - L_s i_d)^2 + (-L_s i_q)^2 \end{aligned}\right\} \qquad (6.2)$$

where L_s is the synchronous inductance and $K_c(f)$ is the core loss constant which is a function of speed. The inductance, L_s was calculated analytically as outlined in Section 4.4.4 for the topology with a pole-arc ratio of 0.80, as 0.32mH. This value will have an effect on the results. It is assumed for the rest of the topologies since the stator is the same and the change in reluctance, $\Re$ due to the different rotors structure can be assumed to be negligible; $L_s = N_{ph}/\Re$. The *d* and *q* axes currents for unity power operation are given as [59]

$$\left.\begin{aligned} i_d &= \frac{L_s}{\lambda_{PM}} 2i_s^2 \\ i_q &= \sqrt{\frac{\lambda_{PM}}{L_s} i_d - i_d^2} \end{aligned}\right\} \qquad (6.3)$$

The core loss constant is determined from core losses at no-load, i.e.,
$K_c(f) = P_{Fe}(f,B,i_s = 0)/\lambda_{PM}^2$, where $\lambda_s = \lambda_{PM}$.

The 0.80 topology should have the highest core losses. From Fig 6.11, they are slightly lower than those of the other two rotors. This discrepancy can be attributed to machine assembly which affects friction losses. This is because the amount of axial loading on the bearings due to the tightening of the stator supporting structure could not be regulated. This would have an effect on the no-load losses due to the relatively low values for the no-load torque. The core loss constant as a function of speed for the three machines is given in Fig 6.12.

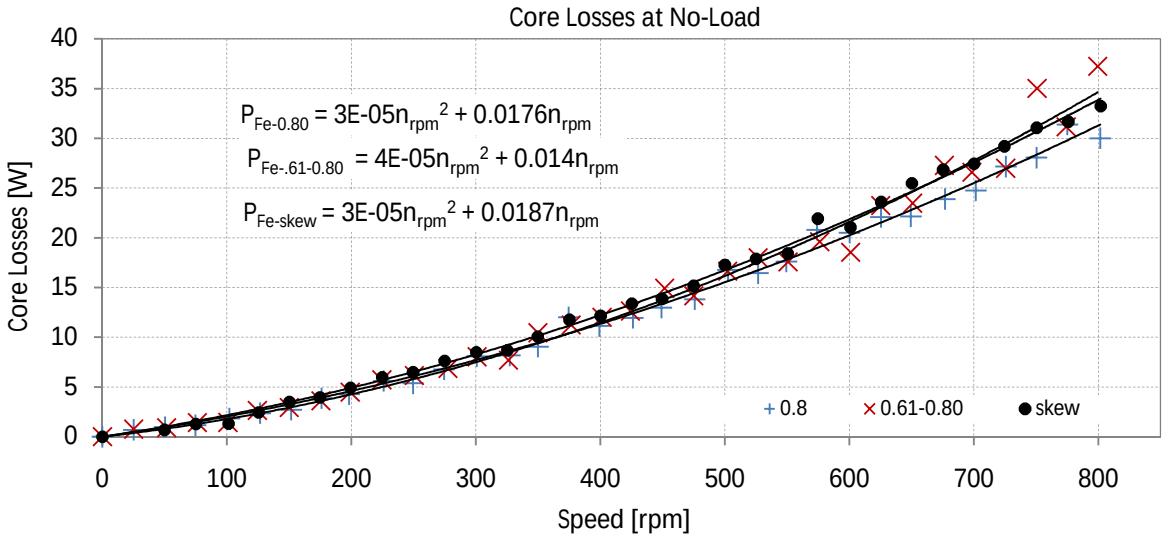

Fig 6.11 Core losses at no-load

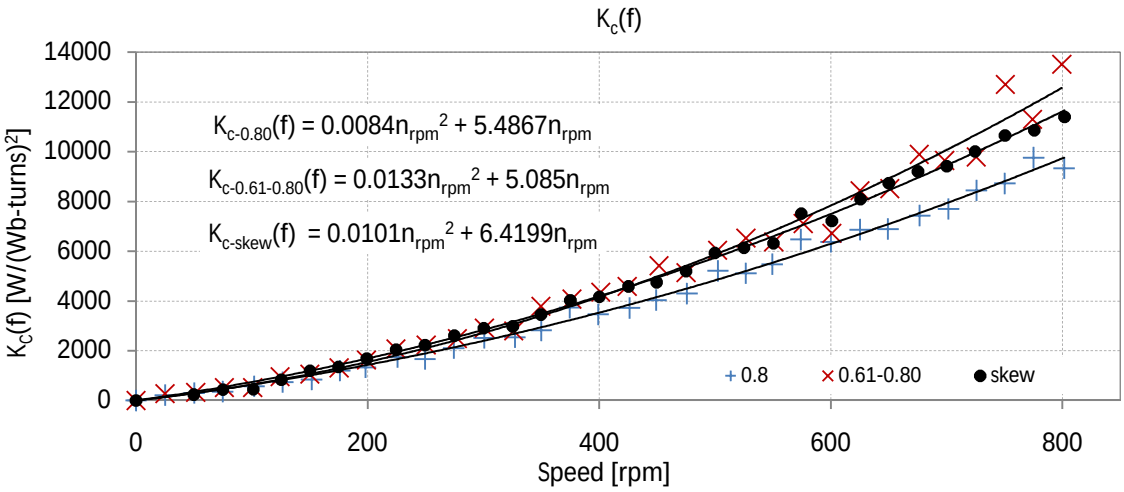

Fig 6.12 Core loss constant as a function of shaft speed

6.2.4 Stray Load Losses

Stray load losses consist of all unaccounted losses in the above mentioned loss components. They are due to slot harmonics and leakage flux induced losses. They are dependent on the loading of the machine and are more pronounced at higher current loadings as shown in Fig 6.13. They are given by the relation

$$P_{stray} = T\omega_m - P_{out} - P_{Cu} - P_{Fe} - P_{F\&W} \tag{6.4}$$

Equation (6.2) is used to estimate core losses while friction & windage losses are estimated using the equations given in Fig 6.10. It is difficult to give the best fit plots for stray load losses for the data in Fig 6.13. This is because the loading points are scattered and they do not give a coherent picture.

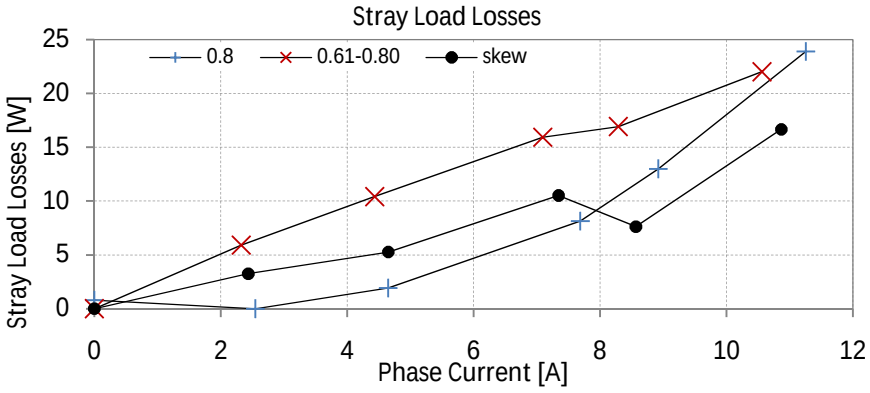

Fig 6.13 Stray load losses at 600rpm and 50Hz

6.2.5 Terminal voltage

The voltage regulation per phase is shown in Fig 6.14 for a resistive load at 600rpm. The machines have good voltage regulation, $\varepsilon = E_f / V_{an}$ of 1.17, 1.19 and 1.18 for a pole-arc ratio of 0.80, alternating pole-arcs and skewed rotors, respectively at a phase load current of 10A. The load voltages at 10A can be estimated as 15.2V, 14V, 14.4V using the best fit curves, respectively. The machines met design requirements for the load voltage at the rated current. The current harmonics were the same as those of the no-load voltages, giving the total harmonic distortions for the power as 0.37% for the 0.80, 0.05% for the alternating pole-arcs and 0.16% for the skewed poles.

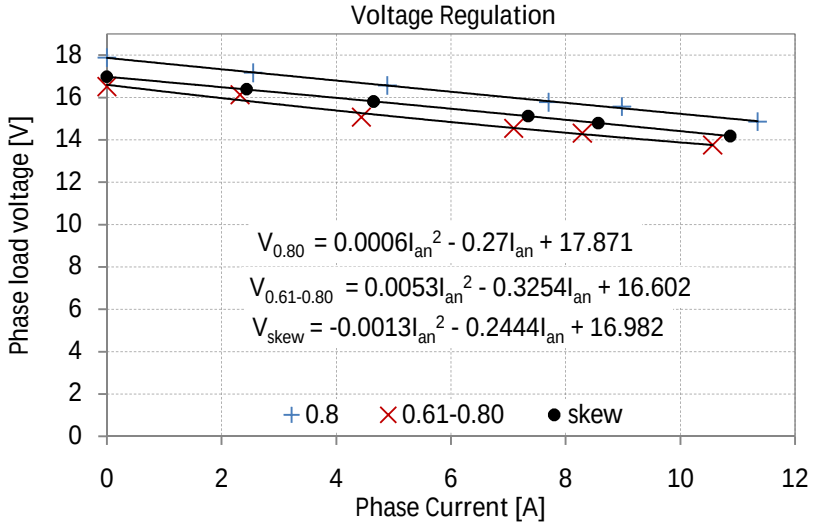

Fig 6.14 Terminal voltage at a rated speed of 600rpm and 50Hz

6.2.6 Efficiency

The efficiency was obtained as a ratio of the measured input shaft power, $P_{in} = T\omega_m$ to the output electrical power, P_{out} for unity power operation at the rated speed of 600rpm. Efficiency at the operating load current of 10A can be obtained by using the best fit curves in Fig 6.15 as 80% for a pole-arc of 0.80, 79% for a alternating pole-arcs and 78% for the skewed topology. These values are acceptable especially for small machines where copper losses are more dominant.

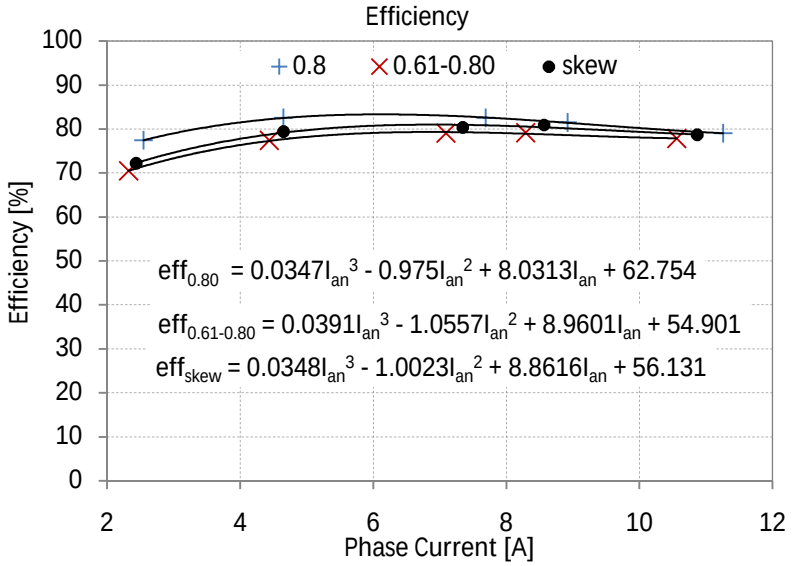

Fig 6.15 Efficiency at a rated speed of 600rpm and 50Hz

6.2.7 Cogging torque

Cogging torque is affected by the assembly and alignment of the machine which adds a pre-load friction component to the machine. If this component is high enough it affects the reading. Therefore, there is a trade-off on relieving the shaft in order to reduce the axial loading on the radial bearings and maintaining an airgap of 1.5mm. This problem may be eliminated or reduced by use of thrust bearings. Cogging torque values are usually obtained at low shaft speeds in order to eliminate no-load losses form the readings. Other factors that could affect torque readings are the non-uniformity of the airgap and the relative magnet positions in one rotor disc relative to the other. The latter is important, noting that the cogging period for the prototyped 0.80 topology was 6 mechanical degrees. Thus by shifting one rotor disc or magnet (when gluing them on the rotor disc) relative to the other, can lead to either cancellation or amplification of cogging torque.

Three methods were used to measure cogging torque. The first involved capturing the torque readings from the transducer using an Oscilloscope at 18rpm as shown in Fig 6.16.

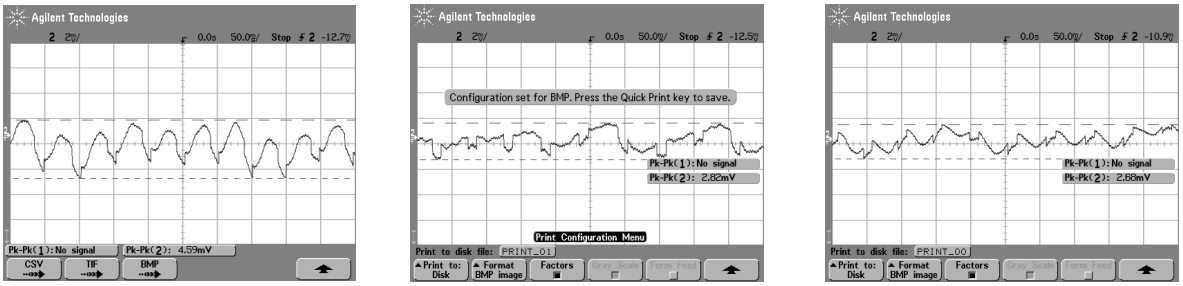

(a) Pole-arc ratio of 0.80 **(b) Alternating pole-arcs** **(c) Skewed poles**

Fig 6.16 Oscilloscope cogging torque results

The second method involved the use of a force balance scale as described in [74] to record the reaction force on the shaft by rotating the stator in discrete steps. The set-up is shown in Fig 6.17.

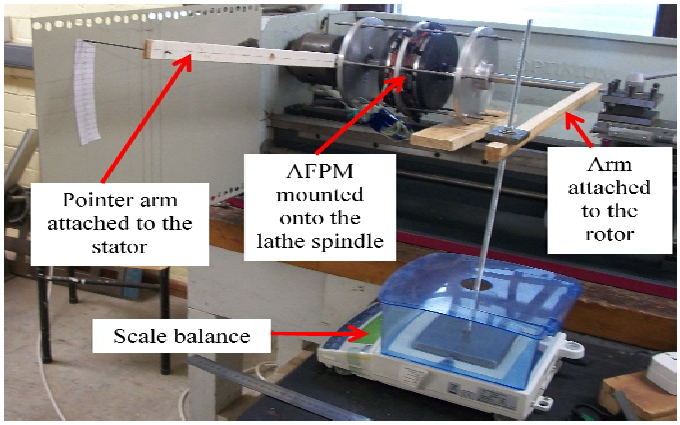

Fig 6.17 Scale balance method

The third method involved capturing the torque readings at around 18rpm and conditioning the signal by FFT. The unfiltered signal is shown in Fig 6.18(a), while in (b) the lower and higher frequency components are filtered. The cogging torque frequency is around 18Hz and is shown in Fig 6.18(c).

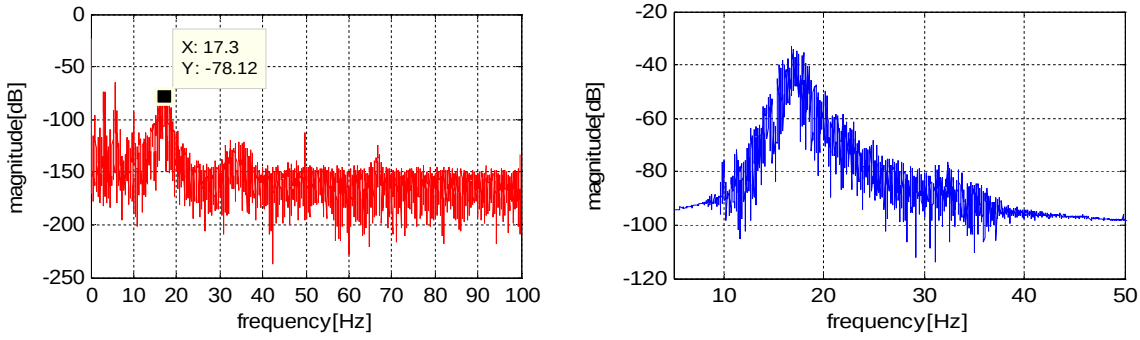

(a) Unfiltered signal **(b) Filtered signal**

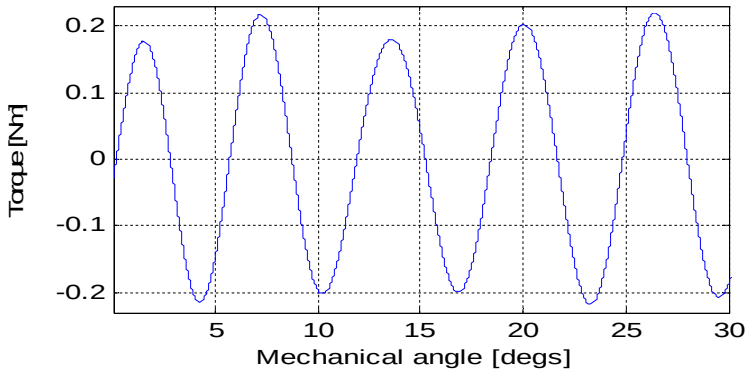

(c) Cogging torque for a pole-arc ratio of 0.80

Fig 6.18 The FFT method

The peak cogging torque readings from the three methods are given in Table 6.2. It was difficult to get reliable results for the alternating pole-arcs and skewed topologies using the scale method. From the Oscilloscope and the FFT readings it can be inferred that the alternating pole-arc method and skewing reduce cogging torque. The readings for the 0.80 topology from the Scale and the FFT methods were used to get the final values which are italicised in Table 6.2. The scale was used to obtain the magnitude while the FFT gave the periodicity as shown in Fig 6.18(c). This was for a topology with a pole-arc ratio of 0.80. The FFT readings were multiplied by a factor of $1.48 = 0.52/0.35$. The readings for the other two topologies were multiplied by the same factor. This argument is shown in Fig 6.19(a) to (c).

Table 6.2 Cogging torque experimental values

Method	0.80 [Nm]	0.61-0.80 [Nm]	Skew [Nm]
Oscilloscope	0.092	0.056	0.054
Scale	0.52	-	-
FFT	0.35	0.11	0.22
Scale + FFT	*0.52*	*0.17*	*0.34*

Fig 6.19(a) shows the results of using one rotor disc and two rotor discs in getting cogging torque. One disc allowed the airgap to be uniform compared to two rotor discs. Its step size was also reduced which gave a better resolution which improved the wave shape.

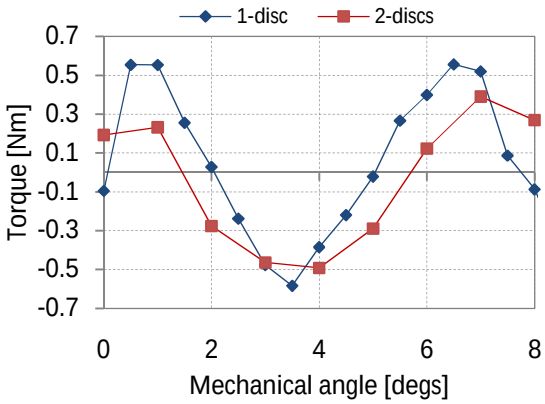

(a) Scale method

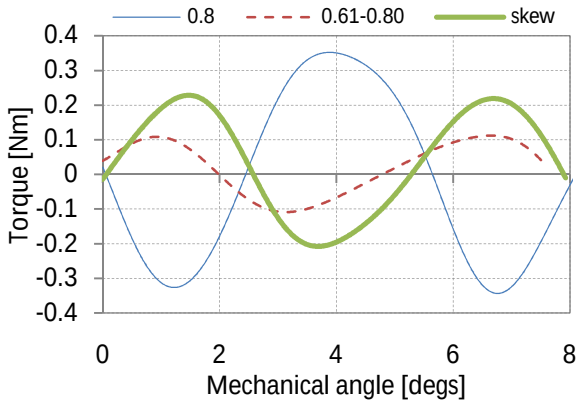

(b) FFT method

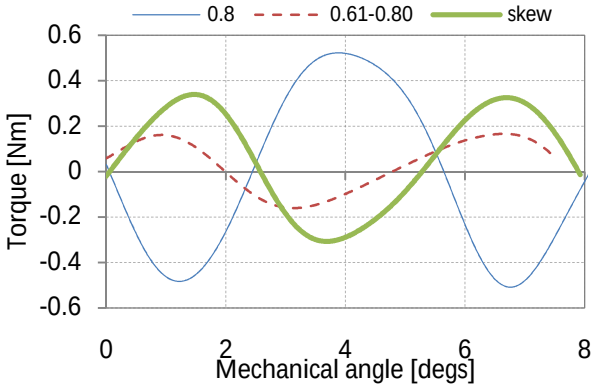

(c) Combination of the Scale and the FFT methods

Fig 6.19 Experimental cogging torque waveforms

6.2.8 Temperature response of the Machine

Thermocouples were fixed to one of the coils, tooth and aluminium flange. They were used to check the effectiveness of the parallel-teeth stator in evacuating heat. Fig 6.20(a) shows the temperature plot at no-load. The temperature was not allowed to level-off but it shows the effect of core losses. Fig 6.20(b) shows the response for the loaded case. The spikes in the core and winding temperatures are due to loading at different points, and clearly indicate the poor heat conduction to the aluminium flange. However, there is good conduction from the windings to the teeth. For the regions bounded by 0-30 minutes and 75-150 minutes (i.e. smooth regions) for the load case, they indicate good conductivity between the flange and the teeth but poor conductivity between the flange and the machine frame. The plot of the aluminium flange temperature shows that its thermal mass and its contact area with the teeth are not able to conduct the heat to the surrounding. The ideal plot should be much closer to the ambient temperature. This would indicate that the aluminium flange is able to conduct heat.

To increase the thermal mass of the aluminium flange, the length of the laminations in the axial direction can be increased. This will increase the axial depth of the aluminium flange and hence the contact area with the teeth, while keeping the slot depth constant. The effect on the electromagnetic circuit can be checked by a plot of flux-density for the new lamination depth and comparing it with the initial plot. This can be used to optimize the length of the lamination and airgap flux-density. The design of the thermal circuit also ensures adequate evacuation of heat generated in the stator core. For the prototyped topology, the aluminium flange had to dissipate most of the heat by convection, since the contact area between the stainless steel supporting rods and the stator had relatively small diameters.

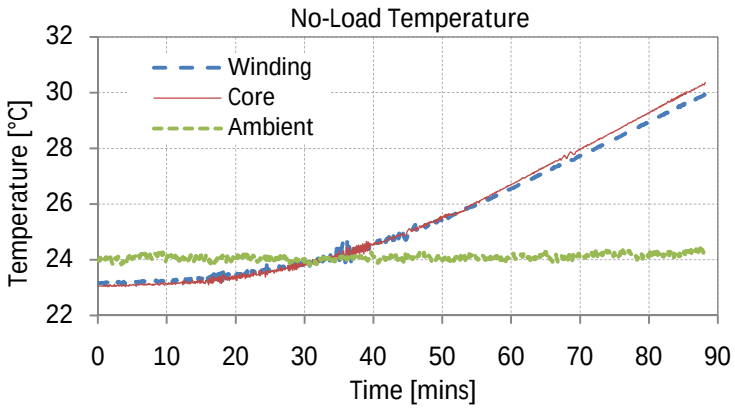

(a) No-load temperature

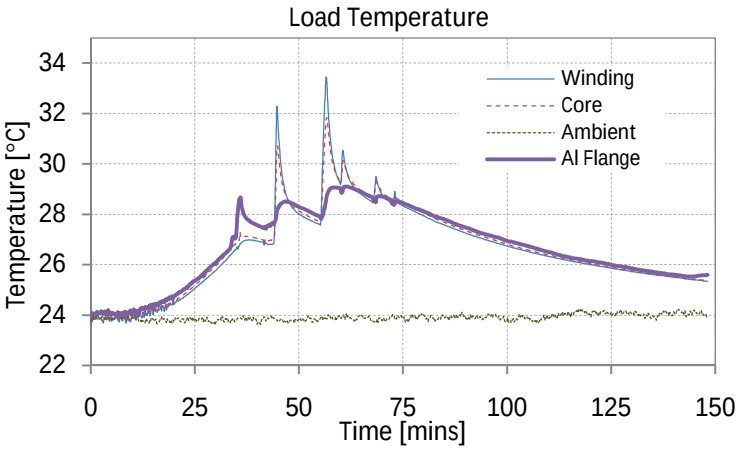

(a) Load temperature

Fig 6.20 Temperature response of the machine

6.3 *Comparison of Results*

Analytical, FEA and experimental results are shown in Table 6.3 at a rated speed of 600rpm. It can be seen that most of the parameters have negligible variation such as λ_{PM} , N_{ph} , R_{ph} , E_f , V_{an}, P_{Fe} *and* P_{stray}. Copper losses for the tested machines are higher than the analytical value. This is due to the higher phase winding resistance. The additional resistance is due to the leads linking the coils to form a phase group and the leads connecting the machine to the power analyser. The friction & windage loss component of the actual machines are also higher. This can be attributed to the axial pre-load component from assembly of the machine. This can be lowered by replacing radial bearings with thrust bearings. Core losses at no-load and load are approximately the same. This can be attributed to operation at low frequencies and negligible armature current for the given loading point which is also evident on the voltage regulation. Another effect on the core loss would be the assumption that all the machines have the same inductance, and the use of the analytical inductance value. The analytical core loss was constant and independent of the load. The low number of turns per phase will also contribute to a low inductance which gives a good voltage regulation and keeps the core losses fairly constant for the given loading points. Stray load losses are approximately the same, although the value for the skewed topology was given by the mean of the stray losses at 7.3A and 10.9A. The value at 8.6A was half the mean value, hence it was negated. The efficiencies of the prototyped machines are lower due to the higher copper and friction & windage losses.

Table 6.3 Comparison of analytical, FEA and experimental results

Parameter	Analytical	FEA				Experimental		
	0.80	0.80		0.61-0.80	skew	0.80	0.61-0.80	skew
		RFPM	AFPM					
B_{mg} (T)	0.742	Max of 0.9 to 1						
λ_{PM} (Wb-turns)	0.0509	0.0586		0.05	0.0535	0.0567	0.0525	0.0540
N_{ph} (turns)	104	96		96	96	96	96	96
R_{ph} (Ohms)	0.16	-		-	-	0.197		
E_f (V)	16.0	17	18.1	15.7	16.8	17.9	16.5	17
E_f / V_{an}	1.1436	-		-	-	1.17	1.19	1.18
$V_{an@10A}$ (V)	14	-		-	-	15.2	14	14.4
ΔV_{an}*% of 15.2V*	-	-		-	-	0	7.9	5.3
P_{Cu} (W)	34.68 $_{@8.5A}$	-		-	-	47$_{@8.9A}$	40.6$_{@8.3A}$	43.4$_{@8.6A}$
$P_{F\&W}$ (W)	9.776	-		-	-	14.15	15	17.41
P_{Fe} (W) - No-load	19.35	-		-	-	20.50	18.54	21.05
P_{Fe} (W) - Load	-	-		-	-	20.10$_{@8.9A}$	21.30$_{@8.3A}$	21.47$_{@8.6A}$
P_{stray} (W)	15	-		-	-	13$_{@8.9A}$	16.9$_{@8.3A}$	14$_{@8.6A}$
P_{out} (W)	357$_{@8.5A}$	364	391	332	358	415$_{@8.9A}$	356$_{@8.3A}$	380$_{@8.6A}$
Eff$_{@10A}$ (%)	80	82	83	82	83	80	78	79
$T_{cog\text{-}pk}$ (Nm) -3D	-	-	0.54	0.10	0.21	0.52	0.17	0.34
$\Delta T_{cog\text{-}pk}$*% of 6.3Nm*	-	-	8.6	1.6	3.3	8.3	2.7	5.4

The experimental and 3D-FEA cogging torque results are compared in Fig 6.21 (a) to (c). Their peak values are given in Table 6.3. The experimental values for the alternating pole-arcs and skewed rotors

are slightly higher than the 3D values. This may be attributed to the methodology used in their computation, i.e. it was assumed the ratio 1.48 is applicable to all the topologies.

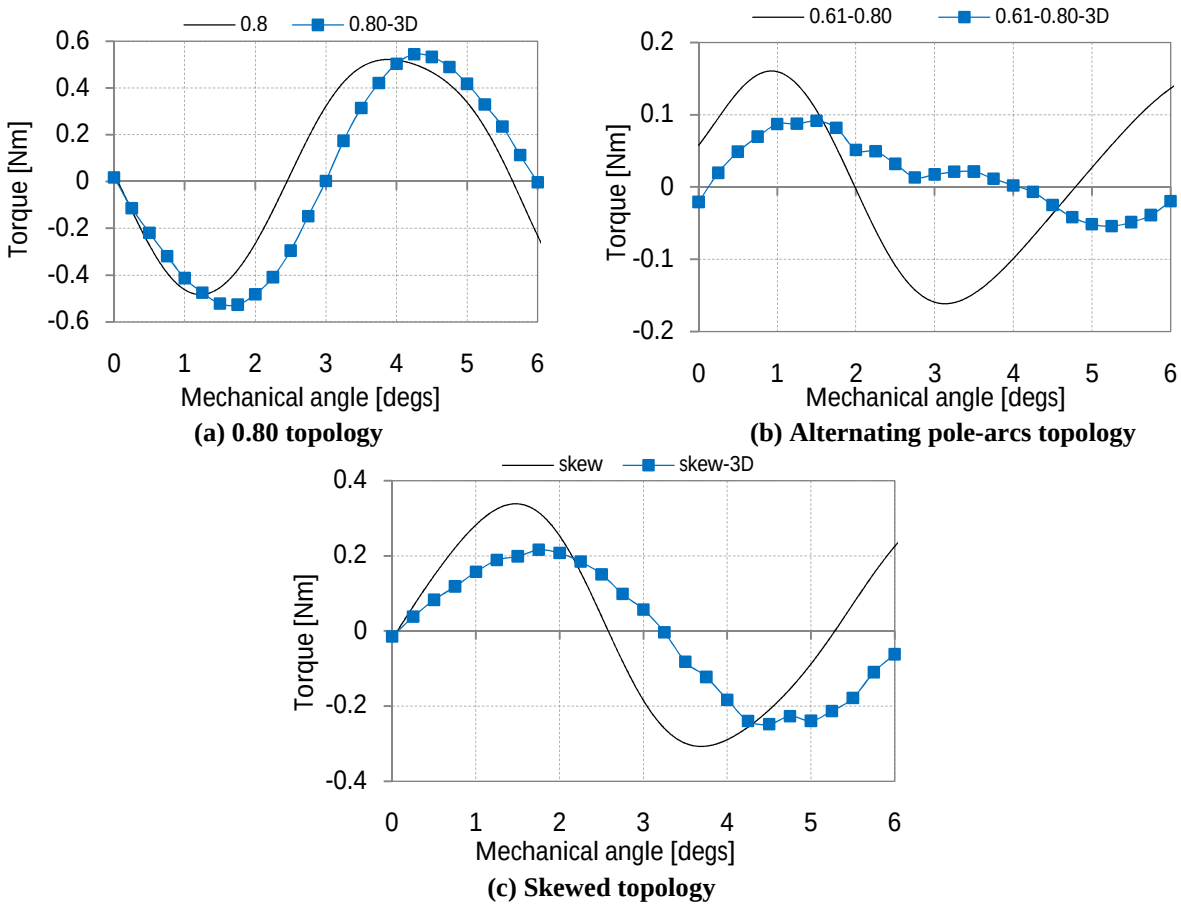

(a) 0.80 topology

(b) Alternating pole-arcs topology

(c) Skewed topology

Fig 6.21 Comparison of experimental and 3D-FEA cogging torque values

Fig 6.22 shows the comparison of experimental and 2D-FEA results for voltage regulation and efficiencies at different loading points for a pole-arc ratio of 0.80. These plots are used to compare and verify the equivalent RFPM 2D-FEA methodology. As seen on the plots, all the values are comparable. The variation in the voltage regulation can be attributed to the differences in flux-linkage, which is evident on the no-load voltage variations. The plots droop due to the demagnetising effect of i_d current which increases with the load current and hence reduce the stator flux-linkage. The variation of the efficiency beyond 6A is not that significant, though the experimental value decreases slightly as the load increases. This is also evident on the voltage regulation plot. The other machines are expected to exhibit similar characteristics, with slightly reduced magnitudes.

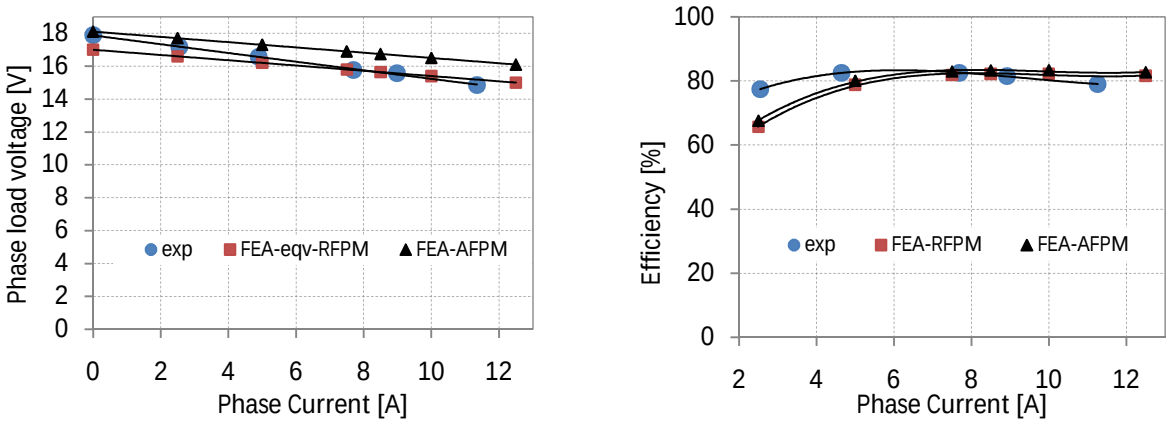

(a) Voltage regulation **(b) Efficiency**

Fig 6.22 Comparison of 2D-FEA and experimental load performance for a pole-arc ratio of 0.80

6.4 *Electrolyser Requirements and Machine Performance*

The electrolyser characterization analysis done in Section 3.3 is used to get electrolyser parameters shown in Table 6.4 for the three generator topologies. This was done at a load current of 10A per phase at 600rpm. The assumed PEM electrolyser has three cells and has a hydrogen production rate of 6.5g/hr. All the parameters of the electrolyser are analytical. It can be seen that the machine performance affects the hydrogen production rate. It is reduced by 6% for a machine with alternating pole-arcs and by 3% for a machine with skewed poles. The electrolyser would operate at a reasonable efficiency and temperature.

Table 6.4 PEM electrolyser performance parameters under rated machine parameters

Topology	V_{an} [V]	D [%]	I_{ely} [A]	H_2 [g/hr]	P_{ely} [W]	Sp. Energy Use [kWh/kgH_2]	Eff [%]	T_{ely} [^oC]
0.8	15.2	0.16	56	6.66	339	51	65	80
0.61-0.80	14.0	0.17	52	6.13	312	51	65	79
skew	14.4	0.17	53	6.31	321	51	65	80

Fig 6.23 shows the effect of generator phase current at 600rpm for a topology with a pole-arc ratio of 0.80 on electrolyser performance. The efficiency is constant at 65% since it is dependent on stack voltage which is assumed constant. The stack voltage is determined by the generator phase voltage, which does not fall below 14V for the given loading points. The stack current is determined by the duty ratio which is fairly constant at 15% and the phase current. The electrolyser stack current, the hydrogen production rate and the stack temperature are all shown to be dependent on the generator current for a fairly constant terminal voltage.

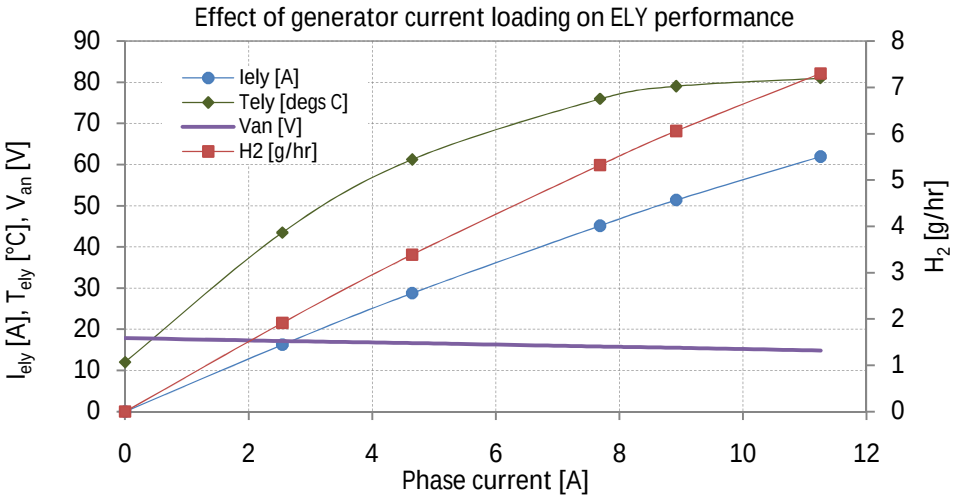

Fig 6.23 Electrolyser performance parameters as a function of voltage regulation

Fig 6.24 can be used in the selection of electrolyser parameters. These include the number of cells, *Ely cells*, the stack voltage, *Uely* and the active area of the cell, *A-MEA*. It is derived for a production rate of 6.5g/hr at a phase current of 10A and phase voltage of 15.2 V for the 0.80 machine. The duty ratio, *D* is for a buck-boost converter which has poor performance at lower and higher ratios. This is important in the design of the converter interface. By having a low number of cells, the converter operates at a lower duty ratio and higher current ratings. The active area of the cells also increases linearly with stack current. This can be offset by increasing the number of cells which lowers the current requirement and increases the stack voltage. It also reduces the active area of the cells (when comparing the number of cells with the active area please trace the values in the vertical direction). Cells can also be connected in parallel, thereby splitting the current into the respective branches. The set-back with this is that the converter loading problem is not alleviated, i.e. the converter load current remains the same. Therefore, the connection of cells in a stack will affect the design of the converter significantly.

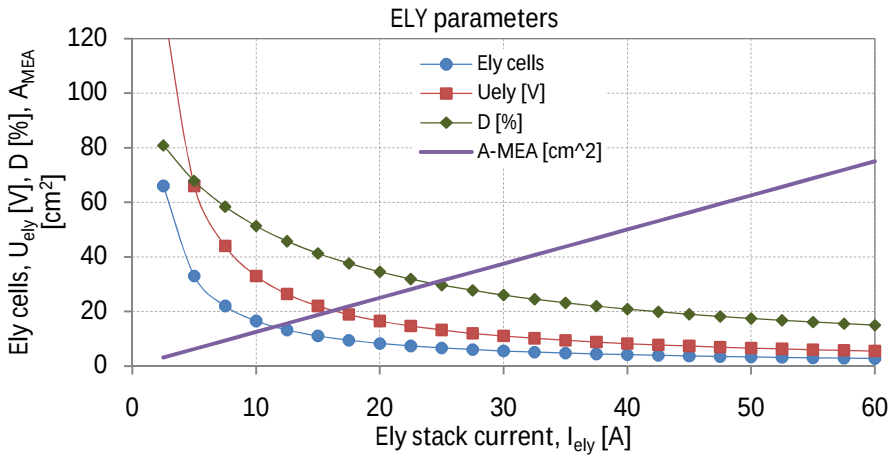

Fig 6.24 Electrolyser parameters for H_2(g/hr) = 6.4g/hr with a generator phase current of 10A and a phase voltage of 15.2V

6.5 *Conclusions*

The double-layer tooth-concentrated windings resulted in a very low harmonic content which was reduced in topologies with skewed magnets and alternating pole-arcs, i.e. as the flux-linkage reduced. It was only the 1st and 3rd harmonics which had a magnitude greater than 0.5V. The experimental no-load voltages were 17.9V for a pole-arc ratio of 0.80, 16.5V for alternating pole-arcs and 17V for the skewed topology. The variation due to the flux-linkage affected all the other parameters. The load voltage at 10A was estimated to be 15.2V, 14V and 14.4V at an efficiency of 80%, 78% and 79% respectively. All the machines met the load voltage requirement of 14V and the efficiencies were acceptable for small machines. It can be concluded that the effect of cogging torque reducing methods on machine performance was minimal. The alternating pole-arcs had the highest difference of 8% for the no-load and load voltages and 2.5% for the efficiency in comparison with the topology with a pole-arc ratio of 0.80.

The efficiency in small machines at relatively low frequencies is mainly due to copper losses. It was shown that the difference in no-load and load core losses was negligible. A methodology for estimating core and stray load losses was also discussed.

The electrolyser performance was shown to be dependent on the machine performance. As expected, the alternating pole-arcs topology lowered the hydrogen production rate by 6% while the skewed topology by 3%. The electrolyser would operate at a reasonable efficiency of 65% at a temperature of approximately 80ºC. The stack voltage was set by the phase voltage and the converter's duty ratio. For a constant stack voltage, the generator phase current determines the stack current which in turn affects the hydrogen production rate and the stack temperature. An approximate way of selecting the electrolyser parameters such as the number of cells, the active area of the membrane and the stack voltage for a given current were also outlined.

7 Conclusions and Recommendations

In this chapter, conclusions and recommendations are drawn from the analyses presented in the process of designing an axial-flux PMSG for a small-scale wind electrolysis plant.

7.1 *Conclusions*

1. A PEM electrolyser was shown to be well suited for intermittent RE applications. It was shown through simulations that the self-starting capability of an electrolyser can be achieved by holding the cell voltage at 2 to 2.2V. As the cell voltage increased beyond 1.481V for constant stack current, the efficiency dropped and the specific energy increased. The excess energy is dissipated as heat and is used in heating the electrolyser. The electrolyser H_2 production rate and temperature were shown to be dependent on the stack current while the efficiency was determined by the electrolyser stack voltage.

2. Different topologies for small-scale application of hydrogen in rural areas were analysed with their possible applications, advantages and disadvantages. It was shown that by using the base load and allowing EES to meet transients, the electrolyser rating was reduced significantly. The analysis also provided a guide to the sizing of an electrolyser by considering the load requirements and efficiencies. It led to the characterization of an 11-cell stack, 1kW, 55A and 20V PEM electrolyser with a production rate of 24g/hr operating at 80-100˚C.

3. An Axial-flux PMSG with a parallel-teeth stator was analysed and the following can be concluded:

    a. Its performance was verified using 2D and 3D FEA. It not only met performance requirements but it lowered cogging torque by 24%, compared to a machine with trapezoidal-teeth.

    b. Different methods of minimizing cogging torque in axial-flux machines were also evaluated. Cogging torque can be reduced to less than 6% of the rated torque by using a pole-arc ratio of 0.72, notching of the teeth and employing alternating pole-arcs. These topologies also minimized ripple torque significantly for unity power factor operation.

c. A methodology for simulating an AFPM machine as an equivalent RFPM was verified. It allowed the use of a 2D open source FEA software, Femm 4.2 in the analysis of the machine.

d. The limitations of using 2D-FEA and quasi-3D-FEA in analysing axial-flux machines were also discussed.

4. A parallel-teeth stator was successfully prototyped and used in the comparative analysis of three PM rotors. The teeth holding method was designed to minimize eddy-current losses due to short-circuiting of laminations and provided adequate mechanical strength. The machine design process was verified by comparing the analytical and/or FEA with experimental results. Their differences were within a reasonable error margin.

   It was also shown that cogging torque reduction methods had an effect on the machine performance. The alternating pole-arcs gave the largest difference of 8% in the no-load and load voltages and 2.5% drop in efficiency in comparison to the machine with a pole-arc ratio of 0.80. The peak cogging torque for the 0.80 rotor was 8.2% of the rated toque. It was reduced by 67% and 37% by using alternating pole-arcs and skewed poles respectively.

   The efficiency in small machines was shown to be largely dependent on copper losses, while core losses were fairly constant for the no-load and loaded cases. A methodology for estimating core losses and stray load losses was also discussed.

5. The electrolyser performance was shown to be dependent on machine performance. The hydrogen production rate was reduced by 6% and 3% for the alternating pole-arcs and skewed topologies respectively. The electrolyser would operate at a reasonable efficiency of 65% at a temperature of approximately 80ºC. It was also shown that for a relatively constant stack voltage which was determined by the generator phase voltage, the generator phase current determines the stack current which in turn affected the hydrogen production rate and the stack temperature. An approximate way of selecting the electrolyser parameters such as the number of cells, the active area of the membrane and the stack voltage for a given current was also outlined.

7.2 *Recommendations*

Based on the conclusions drawn in the previous section, the following recommendations can be made:

1. The use of electrolyser empirical data should be considered to verify the analytical methodology of sizing and characterizing a PEM electrolyser for RE applications proposed in this work. In the process the self-starting capabilities of the electrolyser will be better understood.

2. It was seen that by simply sizing the electrolyser for base load, its rating was lowered to 0.8kW from 1.7kW by using the peak power requirement. To further lower the capital costs of the hydrogen system, a set up incorporating a PEM electrolyser, H_2 storage, EES and FC is recommended. This topology will also reduce the transients 'seen' by the electrolyser, hence increasing its service life.

3. The WECS-ELY system can be made more realistic by including a wind resource assessment for a given site. This will allow the optimization of the electrolyser sizing process by considering both the load and the wind resource.

4. The assembly and efficiency of the machine can be improved by using thrust bearings that reduce the axial force due to the attraction of the stator core and rotor poles. This will reduce the friction losses.

5. Fabrication of the machine as a single unit which does not require assembly and disassembly is highly recommended. This will ensure friction and assembly components are identical, hence easier to characterize because they are independent of workmanship. This will also improve cogging torque measuring techniques, especially with the use of a scale.

6. The stray load results can be improved by using more loading points, which results in a more accurate curve and a better estimation. It is also necessary to incorporate speed variation in all the losses except for the no-load losses, since in normal applications the generator speed varies with wind speed.

7. A torque transducer with a lower rating of approximately 20-50Nm is recommended for machines with a relatively low torque rating. The current torque transducer is rated at 200Nm; hence the readings are at the lower quartile range. The readings were also affected by the

offset on the display of the power analyser that kept changing. This in effect affected the no-load readings especially at low shaft speeds where the values were less than unity. This problem may be solved by using an alternate display that allows zeroing.

8. A thorough thermal analysis should also be conducted for the machine to evaluate thermal performance of the parallel-teeth stator topology.

References

[1] B. Kropotkin, J. Levene, K. Harrison, P.K. Sen, and F. Novachek, "Technical report on Electrolysis: Information and Opportunities for electrical Power Utilities," National renewable energy Laboratory (NREL), A National Laboratory of the U.S. Department of Energy, 2006.

[2] B. Kruse, S. Grinna, and C. Buch, "Hydrogen – Status and Possibilities," The Bellona Foundation, 2002.

[3] Ø. Ulleberg, "Stand-alone power systems for the future: Optimal design, operation & control of solar-hydrogen energy systems," Norwegian University of Science and Technology, Trondheim, Norway, PhD Thesis 1998.

[4] F. Barbir, "PEM electrolysis for production of hydrogen from renewable energy sources," *Solar Energy*, vol. 78, pp. 661-669, 2005.

[5] L.N. Grimsmo, M. Korpås, T.Gjengedal, and S.Møller-Holst, "A probabilistic method for sizing of isolated wind-electrolyzer systems," *http://www.elkraft.ntnu.no/norpie/10956873/Final%20Papers/064%20-%20NORDPIE%202004%20wind-hydrogen.pdf , (26 May 2009).*

[6] http://www.maxwell.com/ultracapacitors/index.asp (28 August, 2009).

[7] H. De Battista, R.J. Mantz, and F. Garelli, "Power conditioning for a wind-hydrogen energy system," *Journal of Power Sources*, vol. 155, pp. 478-486, 2006.

[8] Ø. Ulleberg and S.O. Mørner, "Trnsys simulation models for solar-hydrogen systems," *Solar Energy*, vol. 59, pp. 271-279, 1997.

[9] K. Agbossou, M. Kolhe, J. Hamelin, and T.K. Bose, "Performance of stand-alone renewable energy system based on energy storage as hydrogen," *IEEE Transactions on Energy Conversion*, vol. 19, pp. 633-640, 2004.

[10] R.E. Clarke et al., "Direct coupling of an electrolyser to a solar PV system for generating hydrogen," *Int. J. Hydrogen Energy*, vol. 34, pp. 2531-2542, 2009.

[11] S.P.S. Badwal, S. Giddey, and F.T. Ciacchi, "Hydrogen and oxygen generation with polymer electrolyte membrane (PEM)-based electrolytic technology," *Ionics*, vol. 12, pp. 7-12, 2006.

[12] J.J. Hwang, W.R. Chang, and A. Su, "Dynamic modeling of a solar hydrogen system under leakage conditions," *Int. J. Hydrogen Energy*, vol. 33, pp. 3615-3624, 2008.

[13] Ø. Ulleberg, "The importance of control strategies in PV-hydrogen systems," *Solar Energy*, vol. 76, pp. 323-329, 2004.

[14] L.M. Gandía, R. Oroz, A. Ursúa, P. Sanchis, and P.M.Diéguez, "Renewable Hydrogen Production: Performance of an Alkaline Water Electrolyzer Working under Emulated Wind Conditions," *Energy & Fuels*, vol. 21, pp. 1699-1706, 2007.

[15] J. Samaniego, F. Alija, S. Sanz, C. Valmaseda, and F. Frenchoso, "Economic and technical analysis of a hybrid wind fuel cell energy system," *Renewable energy*, vol. 33, pp. 839-845, 2008.

[16] P.C. Ghosh, B.Emonts, H Janßen, J. Mergel, and D. Stolten, "Ten years of operation experience with a

hydrogen-based renewable energy supply system," *Solar Energy*, vol. 75, pp. 469-478, 2003.

[17] Ø. Ulleberg, "Modelling of advanced alkaline electrolyzers: a system simulation approach," *Int. J. Hydrogen Energy*, vol. 28, pp. 21-33, 2003.

[18] T.F. El-Shatter, M.N. Eskander, and M.T. El-Hagry, "Energy flow management of a hybrid wind/PV/fuel cell generation system," *Energy Conversion & Management*, vol. 47, pp. 1264-1280, 2006.

[19] "Hydrogen research center for South Africa," *Fuel Cells Bulletin*, vol. 2008, no. 2, p. 11, Feb 2008.

[20] Siegfried Heier, *Grid Integration of wind Energy Conversion Systems*, 2nd ed. The Atrium, Southern Gate, Chichester, West Sussex PO 19 8SQ, England: John Wiley & Sons, Ltd.

[21] http://www.siemens.com/energy (13 September, 2010).

[22] M. Aydin, S. Huang, and T.A. Lipo, "Axial Flux Permanent Magnet Disc Machines: A Review," in *the 37th IAS Annual Meeting, Industry Applications Conference*, 2002, pp. 1250-1257.

[23] Y.G. Guo and J.G. Zhu, "Study of permanent magnet transverse flux motors with soft magnet composite core," in *AUPEC*, Brisbane, Australia, 2004.

[24] J.F. Gieras, Rong-Jie Wang, and M.J. Kamper, *Axial Flux Permanent Magnet Machines*.: Kluwer Academic Publishers, Dordrecht/Boston/London, 2004.

[25] S. Huang, M. Aydin, and T.A. Lipo, "Comparison of (Non-Slotted and Slotted) surface Mounted PM Motors and Axial Flux Motors for Submarine Ship Drives," in *3rd Naval Symposium on Electrical Machines, 2000. International Agean Conference on electrical Machines and and Power electronics*, Kusadasi, Turkey , June 2001.

[26] R. Qu and T.A. Lipo, "Sizing Equations and Power Density Evaluation of Dual-Rotor, Radial-Flux, Toroidally Wound, Permanent-Magnet Machines," in *16th International Conference on Electrical Machines (ICEM)*, Cracow, Poland, 2004.

[27] P. Salminen, J. Pyrhonen, F. Libert, and J. Soulard, "Torque ripple of permanent magnet machines with concentrated windings," in *XII International Symposium on Electromagnetic Fields in Mechatronics, Electrical and Electronic Engineering (ISEF)*, Baiona, Spain.

[28] M. Aydin, Z.Q. Zhu, and T.A. Lipo, "Minimization of Cogging Torque in Axial-Flux Permanent-Magnet Machines: Design Concepts," *IEEE Transactions on Magnetics*, vol. 43, no. 9, pp. 3614-3622, 2007.

[29] M. Aydin, R. Qu, and T.A. Lipo, "Cogging Torque Minimization Technique for Multiple-Rotor, Axial-Flux, Surface-Mounted-PM Motors: Alternating Magnet Pole-Arcs in Facing Rotors," in *Industry Applications Conference, 38th IAS Annual Meeting*, 2003, pp. 555-561.

[30] J.-B. Eom, S.-M. Hwang, T.-J. Kim, W.-B. Jeong, and B.-S. Kang, "Minimization of cogging torque in permanent magnet motors by teeth pairing and magnet arc design using genetic algorithm," *Journal of magnetism and magnetic materials*, pp. 1229-1231, 2001.

[31] F. Libert and J. Soulard, "Investigation on Pole-Slot Combinations for Permanent-Magnet Machines with Concentrated Windings," in *International Conference on Electrical Machines (ICEM)*, Cracow, Poland, 2004.

[32] C.-C. Hwang, P.-L. Li, F.C. Chuang, C.-T. Liu, and K.-H. Huang, "Optimization for Reduction of Torque

Ripple in an Axial Flux Permanent Magnet Machine," *IEEE Transactions on Magnetics*, vol. 45, no. 3, 2009.

[33] C. Mandil, "Hydrogen & Fuel Cells," International Energy Agency (IEA), 2004.

[34] http://www.global-hydrogen-bus-platform.com / (09 June, 2010).

[35] P. Thounthong, B. Davat, S. Rael, and P. Sethakul, "Fuel Cell High-Power Applications," *IEEE Industrial Electronics Magazine*, pp. 32-46, March 2009.

[36] S.A. Sherif, F. Barbir, and T.N. Veziroglu, "Wind energy and the hydrogen economy-review of the technology," *Solar Energy*, vol. 78, pp. 647-660, 2005.

[37] S. Busquet, C.E. Hubert, J. Labbe, D. Mayer, and R. Metkemeijer, "A new approach to empirical electronic modelling of a fuel cell, an electrolyser or a regeneretive fuel cell," *Journal of Power Sources*, vol. 134, pp. 41-48, 2004.

[38] R.F. Mann, J.C. Amphlett, M.A.I. Hooper, and H.M. Jensen, "Development and application of a generalised steady-state electrochemical model for a PEM fuel cell," *Journal of Power Sources*, vol. 86, pp. 173-180, 2000.

[39] M. Newborough, "A Report on Electrolysers, Future Markets and the Prospects for ITM Power Ltd's Electrolyser Technology," Heriot-Watt University, Edinburgh, 2004.

[40] P. Choi, D.G. Bessarabov, and R. Datta, "A simple model for solid polymer electrolyte (SPE) water electrolysis," *Solid State Ionics*, vol. 175, pp. 535-539, 2004.

[41] M.E. Lebbal and S. Lecoeuche, "Identification and monitoring of a PEM electrolyser based on dynamical modelling," *Int. J. Hydrogen Energy*, vol. 34, pp. 5992-5999, 2009.

[42] L.G. Arriaga, W. Martinez, U.Cano, and H. Blud, "Direct coupling of a solar-hydrogen system in Mexico," *Int. J. Hydrogen Energy*, vol. 32, pp. 2247-2252, 2007.

[43] H. Görgün, "Dynamic modelling of a proton exchange membrane (PEM) electrolyzer," *Int. J. Hydrogen Energy*, vol. 31, pp. 29-38, 2006.

[44] Z. Zhi-dan, H. Hai-bo, Z. Xin-jian, C. Guang, and R. Yuan, "Adaptive maximum power point tracking control of fuel cell power plants," *Journal of Power Source*, vol. 176, pp. 259-269, 2008.

[45] R.A. Costa and J.R. Camacho, "The dynamic and steady state behaviour of a PEM fuel cell as an electric energy source," *Journal of Power Source*, vol. 161, pp. 1176-1182, 2006.

[46] NIIR Board, *Hand book on Biogas and its Applications*, 1st ed. Delhi, India: National Institute of Industrial Research (NIIR), 2004.

[47] U. Gautam, "Biogas Technology: A training manual," Food and Agricultural Organisation (FAO) of the United Nations, 1996.

[48] "Hydrogen Fuel Cell Engines and Related Technologies," College of the Desert, Monterey Avenue, Palm Desert, CA 92260, USA, 2001.

[49] http://www.prb.org/Articles/2008/kenya.aspx?p=1 (24 September, 2009).

[50] G.P. McTaggart-Cowan, S.R. Munshi, S.N. Rogak, P.G. Hill, and W.K. Bushe, "Hydrogen-Methane Blend Fuelling of a Heavy-Duty, Direct-Injection Engine," in *Proceedings of IMECE2007, ASME Int.*

Mechanical Engineering Congress and Exposition, Seattle, Washington, USA, 2007.

[51] S.O.B. Shrestha and G.A. Karim, "Hydrogen as an additive to methane for spark ignition engine applications," *Int. J. Hydrogen Energy*, vol. 24, pp. 577-586, 1999.

[52] V.K. Vijay, R. Chandra, P.M.V. Subbarao, and S.S. Kapdi, "Biogas Purification and Bottling into CNG Cylinders: Producing Bio-CNG from Biomass for Rural Automotive Applications," in *The 2nd Joint Int. Conference on Sustainable Energy and Environment*, Bangkok, Thailand, 2006.

[53] M. Cavallini, A. Furci, G. Solero, P. Lopinto, and G. Migliavacca, "Hydrogen-Methane Blended Fuel Jet Flames: Study of Ignition and Flames Morphology," *Italian Section of the Combustion Institute (Combustion Colloquia), Universita Degli Studi Di Napoli, Federico II*, April 2009.

[54] A. B. Sebitosi, "Application of advances in automotive technologies to electrification in rural sub-Saharan Africa," Electrical Engineering, University of Cape Town, South Africa, PhD Thesis 2004.

[55] U. Bossel, "Efficiency of Hydrogen Fuel Cell, Diesel-SOFC-Hybrid and Battery Electric Vehicles," *European Fuel Cell Forum*, 2003.

[56] L.K. Heung, "Using Metal Hydride to Store Hydrogen," Savannah River Technology, Aiken, SC 29808, USA, 2003.

[57] http://www.ika.rwth-aachen.de/r2h/index.php/Hydride_Hydrogen_Storage (24 September, 2009).

[58] N. Mohan, T.M. Undeland, and W.P. Robbins, *Power Electronics: Converters, Applications, and Design*, 3rd ed. USA: John Wiley & Sons, 2003.

[59] M.A. Khan, "Contributions to Permanent Magnet Wind Generator Design Including the Application of Soft Magnetic Composites," Electrical Engineering Department, University of Cape Town, Cape Town, South Africa, PhD Thesis 2006.

[60] A. Parviainen, M. Niemela, and Pyrhonen J, "Modelling of Axial Flux Permanent-Magnet Machines," *IEEE Transactions on Industrial Applications*, vol. 40, no. 5, 2004.

[61] J. R. Hendershot Jr. and T.J.E. Miller, *Design of brushless permanent-magnet motors*.: Magna Physics Publishing and Clarendon Press, Oxford, 1994.

[62] M. A. Khan and P. Pillay, "Analytical Design of a PM Wind Generator Optimized over a Wide Operating Range," in *IEEE International Electrical Machines and Drives Conference (IEMDC)*, San Antonio, Texas, 2005, pp. 1501-1506.

[63] S. Huang, J. Luo, F. Leonardi, and T.A. Lipo, "A Comparison of Power Density for Axial Flux Machines Based on General Purpose Sizing Equations," *IEEE Transactions on Energy Conversion*, vol. 14, no. 2, June 1999.

[64] R.-J. Wang, M.J. Kamper, K. Van der Westhuisen, and J.F Gieras, "Optimal Design of a Coreless Stator Axial Flux Permanent-Magnet Generator," *IEEE Transactions on Magnetics*, vol. 41, pp. 55-64, Jan 2005.

[65] P.C. Sen, *Principles of Electric Machines and Power Electronics*.: J. Wiley, 1997.

[66] S.E. Skaar, Ø. Krøvel, and R. Nilsen, "Distribution, coil-span and winding factors for PM machines with concentrated windings," in *International Conference on Electrical Machines (ICEM)*, Chania, Greece, 2006.

[67] F. Magnussen and C. Sadarangani, "Winding Factors and Joule Losses of Permanent Magnet Machines with Concentrated Windings," in *Electric Machines and Drives Conference (IEMDC)*, Madison, Wisconsin, USA, 2003, pp. 333-339.

[68] J. Germishuizen and M. Kamper, "Design and Performance Characteritics of IPM Machines with Single Layer Non-overlapping Concentrated Windings," in *Proc. of IEEE Industry Applications*, 2007, pp. 141-147.

[69] A. Parviainen, "Design of Axial-Flux Permanent-Magnet Low-Speed Machines and Performance Comparison between Radial-Flux and Axial-Flux Machines," Lappeenranta University of Technology, Lappeenranta, Finland, D.Sc. Thesis 2005.

[70] M. Aydin, S. Huang, and T.A. Lipo, "Design and 3D Electromagnetic Field Analysis of Non-Slotted and Slotted TORUS Type Axial Flux Surface Mounted Permanent Magnet Disc Machines," in *International Electrical Machines and Drives Conference (IEMDC)*, 2001.

[71] M. Aydin, S. Huang, and T.A. Lipo, "A New Axial Flux Surface Mounted Permanent Magnet Machine Capable of Field Control," in *Industry Applications Conference, 2002, 37th IAS Annual Meeting*, 2002, pp. 1250-1257.

[72] T.F. Chan and L.L. Lai, "An Axial-Flux Permanent-Magnet Synchronous Generator for a Direct-Coupled Wind-Turbine System," *IEEE Transactions on Energy Conversion*, vol. 14, no. 1, pp. 86-94, June 1999.

[73] M.J. Kamper, A.J. Rix, D.A. Willis, and R.-J. Wang, "Formulation, Finite-Element Modeling and Winding Factors of Non-overlap Winding Permanent Magnet Machines," in *Proc. of the 2008 International Conference on Electrical Machines*, 2008.

[74] Z.Q. Zhu, "A Simple Method for Measuring Coggiing Torque in Permanent Magnet Machines," in *Power & Energy Society General Meeting, 2009. PES '09. IEEE*, pp. 1-4. 26-30 July 2009.

[75] http://www.nap.edu/openbook.php?record_id=10922&page=240 (19 June 2009).

Appendices

Appendix A: Conversion Parameters and Safety Statistics for Hydrogen and other Fuels

Table A.1Conversions parameters

Metric ton (tonne) = 1,000 kg = 1.1023 short tons Btu = 1055 J Quad = 10^{15} Btu = 1.055 EJ Litre = 0.2642 US gallons Cubic meter (m^3) = 35.31 cubic feet		
Hydrogen conversions 1 million scf/day = 2.65 short tons/day 1 kg = 11.13 Nm^3 (0°C and 1 atms) 1 kg = 415.6 scf (60°F and 1 atms)		
Densities	**vapour (20°C; 68°F, 1 atms)**	**Liquid (at normal b.p., 1atms)**
Hydrogen	0.08376 kg/m^3 (0.005229 lb/ft^3)	70.8 kg/m^3 (4.432 lb/ft^3)
Methane	0.65 kg/m^3 (0.0406 lb/ft^3)	422.8 kg/m^3 (26.4 lb/ft^3)
Gasoline	4.4 kg/m^3 (0.275 lb/ft^3)	700 kg/m^3 (43.7 lb/ft^3)
Note*:** scf = standard cubic feet; Btu = British thermal unit; EJ = exajoule = 10^{18} J; kg = kilogram Nm^3 = normal cubic meter ***Source: Hydrogen Fuel Cell Engines and Related Technologies (Dec, 2001) [48] and http://www.nap.edu/openbook.php?record_id=10922&page=240 (19 June 2009) [75].		

Appendix B: WECS, WECS-ELY Interface and ELY Simulink® Model

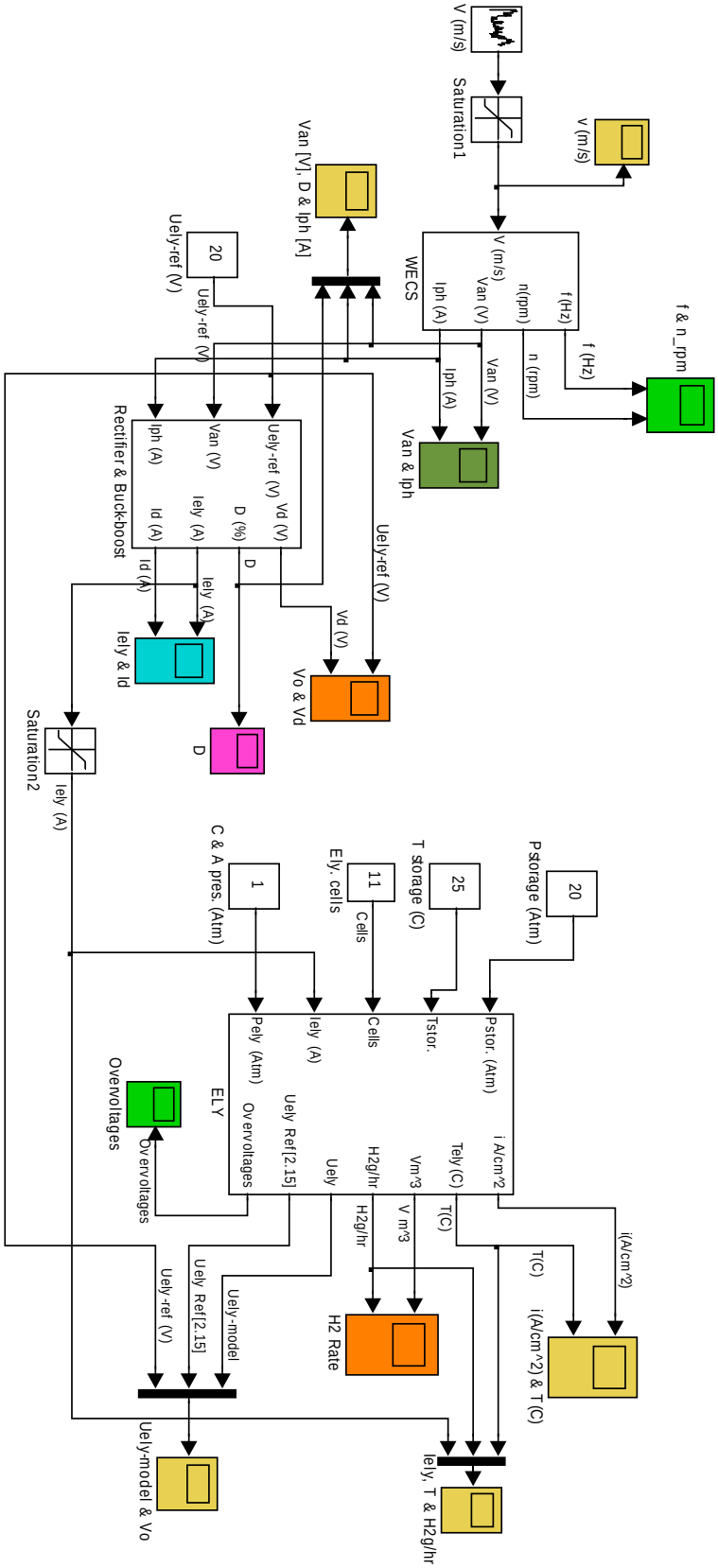

Fig B.1 Simulink® model

Appendix C: Winding Layouts and Factors for different Pole-Slot Combinations

Table C.2 Winding factor for different number of poles, *p* and slots Q_s combinations [31]

Qs\p	4	6	8	10	12	14	16	18	20	22	24	26	28	30	32	34	36	38	40	42
6	0.866		0.866	0.500		0.500	0.866		0.866	0.500		0.500	0.866		0.866	0.500		0.500	0.866	
9	0.617	0.866			0.866	0.617	0.328		0.328	0.617	0.866			0.866	0.617	0.328		0.328	0.617	0.866
12	1		0.866				0.866		…	…		…	…		0.866				0.866	
15			0.621	0.866					0.866	0.621		…	…		…	…		0.621	0.866	
18		1	…	0.647	0.866						0.866	0.647	…	…	…	…		…	…	…
21			…	…		0.866	0.890		0.953	0.953		0.890	0.866		…	…		…	…	
24			1	…		0.760	0.866			0.950		0.950			0.866	0.760		…	…	
27				…	…	…	…	0.866	0.877	0.915		0.954	0.954		0.915	0.877	0.866	…	…	…
30				1		…	…		0.866	0.874		0.936				0.936		0.874	0.866	
33						…	…		…	0.866		0.903	0.928		0.954	0.954		0.928	0.903	
36					1	…	…		…	…	0.866	0.867				0.953		0.953		
39						…	…		…	…		0.866	0.863		0.918	0.936		0.954	0.954	
42						1	…		…	…		…	0.866		0.890	0.913		0.945	0.953	

Qs\p	42	44	46	48	50	52	54	56	58	60	62	64	66	68	70	72	74	76	78	80
45		0.955	0.955			0.927		0.886	0.859	0.866	…	…	…	…	…		…	…	…	…
48		0.950	0.954		0.954	0.950			0.905		0.857	0.866		…	…		…	…		…
51		0.933	0.944		0.955	0.955		0.944	0.933		0.901	0.880		0.866	…		…	…		…
54		0.915	0.930		0.949	0.954		0.954	0.949		0.930	0.915		0.877	0.854	0.866	…	…	…	…
57		0.932	0.912		0.937	0.946		0.955	0.955		0.946	0.937		0.912	0.932		0.852	0.866		…
60		0.874	0.892			0.936			0.954		0.954			0.936			0.892	0.874		0.866
63	0.866	0.850	0.871	0.890	0.905	0.919			0.948	0.953	0.955	0.955	0.953	0.948			0.919	0.905	0.890	0.871
66		0.866	0.849		0.887	0.903		0.928	0.938		0.951	0.954		0.954	0.951		0.938	0.928		0.903
69		…	0.866		0.867	0.884		0.914	0.925		0.943	0.949		0.955	0.955		0.949	0.943		0.925
72	…	…	…	0.866	0.847	0.867			0.911		0.933		0.950	0.953	0.954		0.954	0.953	0.950	
75		…	…		0.866	0.846		0.880	0.895		0.920	0.930		0.945			0.955	0.955		
78		…	…		…	0.866		0.863	0.879		0.906	0.918		0.936	0.943		0.952	0.954		0.954
81	…	…	…	…	…	…	0.866	0.845	0.860	0.877	0.890	0.904	0.915	0.925	0.933		0.946	0.951	0.954	0.955
84		…	…		…	…		0.866	0.845		0.876	0.890		0.913			0.939	0.945		0.953
87		…	…		…	…		…	0.866		0.859	0.874		0.899	0.910		0.929	0.936		0.947
90	…	…	…	…	…	…		…	…	0.866	0.843	0.859	0.874	0.886			0.918	0.927	0.936	

0.866	k_{w1}= 0.866, q=1/2, 1/4		k_{w1}= 0.945, q=3/8, 3/10	0.955	Qs=21+6k, p=Qs±1, k = 0, 1, 2 …
	k_{w1}= 0.902, q=3/7, 3/11		k_{w1}= 0.951, q=5/14, 5/16	0.954	Qs=24+6k, p=Qs±2, k = 0, 1, 2 …
	k_{w1}= 0.933, q=2/5, 2/7		not allowed	…	k_{w1} < 0.866

Table C.3 Winding layouts (A' is the RETURN conductor corresponding to the GO conductor A; the colour code also apply to this table) [31]

Slot/pole combination or number of slot per pole per phase q	Winding layout
q = 2/5, 2/7	...|C' A|A' A'|AB'|BB|B' C|C' C'|CA|AA|A' B B' B'|BC'|CC...
q = 3/8, 3/10	...|C' A A' A'|AA|A' B|B' B'|BB|B' C|C' C'|CC ...
q = 3/7, 3/11	...|CA'|AB'|BB|B' C'|CA|A' A'|AB'|BC'|CC|C' A|A' B|B' B'|BC'|CA'|AA A' B|B' C|C' C'...
q = 5/14, 5/16	...|C' A|A' A'|AA|A' A' AA|A' B|B' B'|BB|B' B'|BB|B' C|C' C'|CC C' C'|CC...
Qs = 12 + 6k, with k = 0, 1, 2 … p = Qs ± 2 If p/2 even	...A|A' A'|A ...A|A' A'|AB'|BB|B'...B'|BB|B'C|C' C'|C...C|C' C'|C... (Qs/6 each)
If p/2 odd	A|A' A'|A...A'|AA|A'B|B' B'|B...B'|BB|B'C|C' C'|C...C'|CC|C'A'|...|AB|...|B'C'...|C (Qs/6, Qs/6, Qs/6, Qs/6, Qs/5, Qs/6)
Qs = 9 + 6k, with k = 0, 1, 2 … p = Qs ± 1	A|A' A|A...A'|AA|A'B|B' B' B...B'|BB|B'C|C' C'|C...C'|CC|C' (Qs/3, Qs/3, Qs/3)

Appendix D: Comparison of Some Silicon Steels

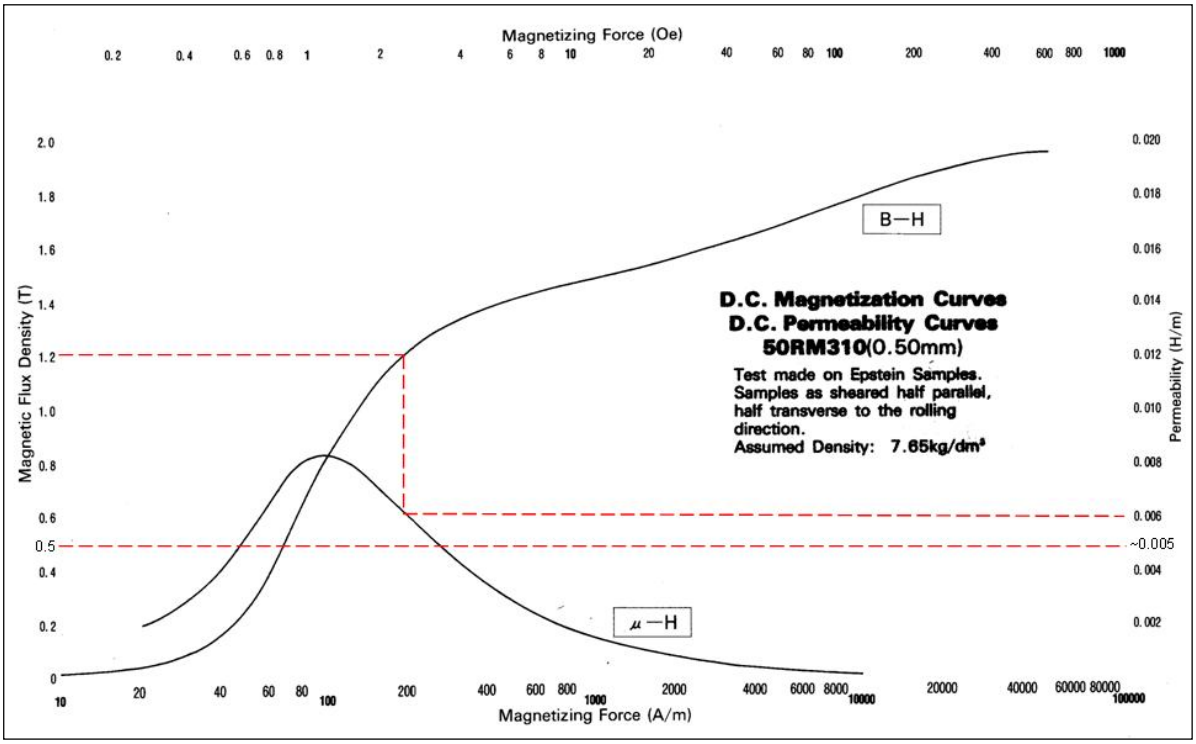

Fig D.2 DC magnetization curve for M310-50A

(*Source*: **http://www.unilam.co.za/** July, 2010)

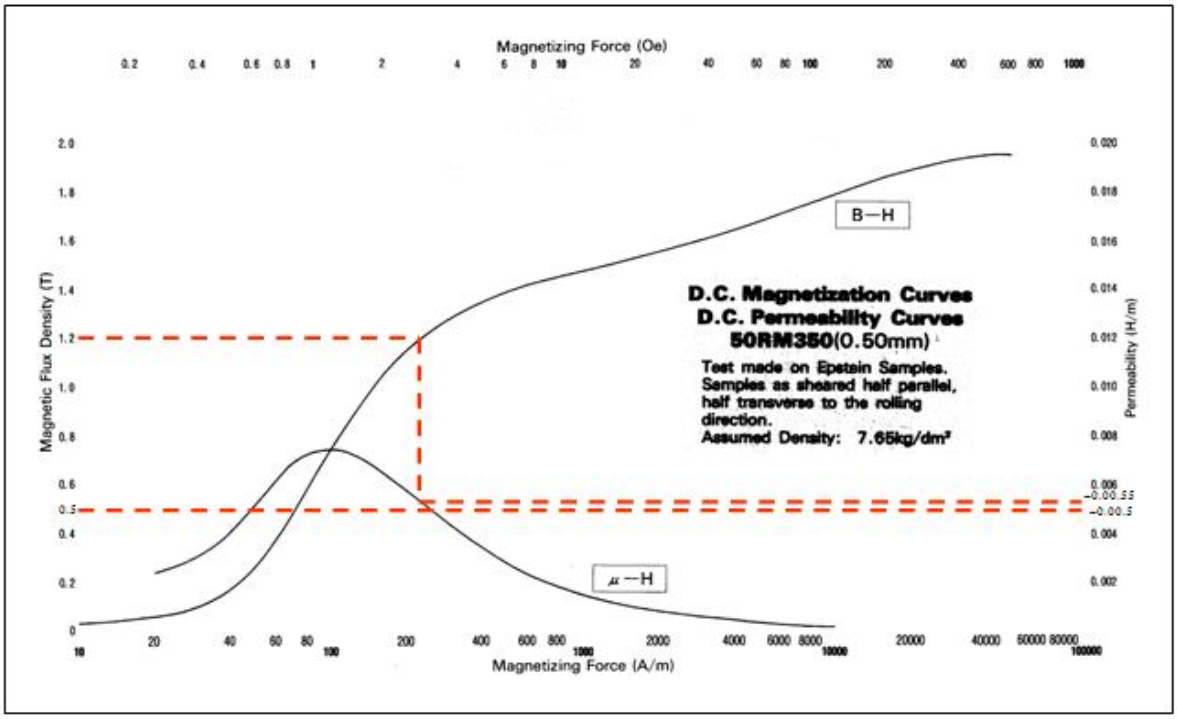

Fig D.3 DC magnetization curve for M350-50A

(*Source*: **http://www.unilam.co.za/** July, 2010)

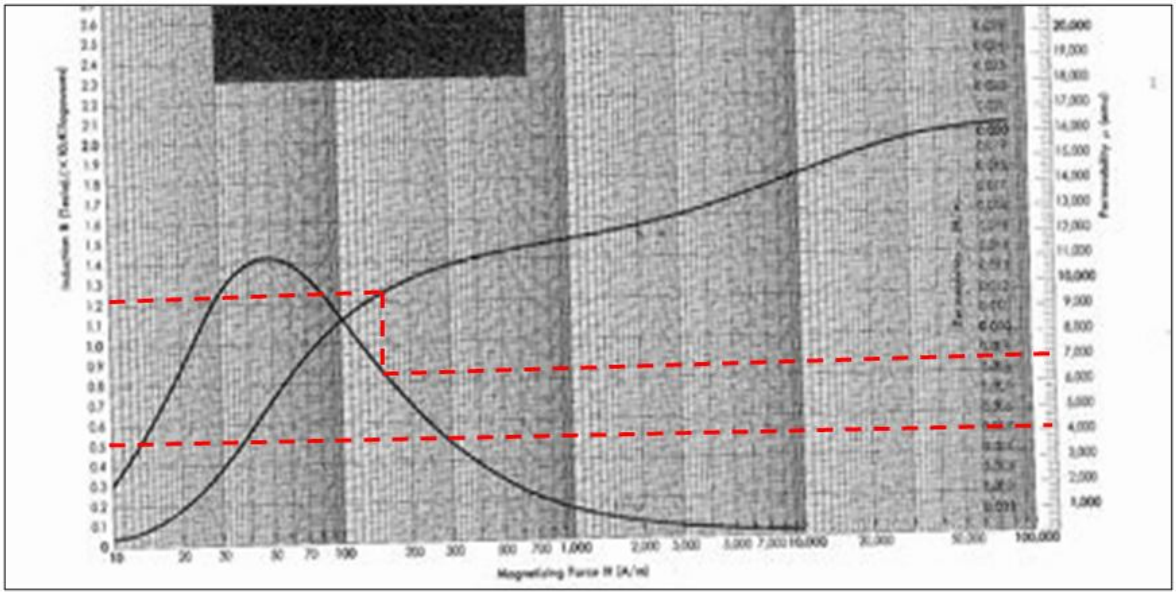

Fig D.4 DC magnetization curve for 50H270

(*Source*: **http://www.amccores.com/** July, 2010)